Dissertation zur Erlangung des Doktorgrades
der Fakultät für Chemie und Pharmazie
der Ludwig-Maximilians-Universität München

Tip-enhanced near-field optical microscopy on the quasi 1D semiconductors carbon nanotubes and CdSe nanowires

von
Miriam Böhmler
aus
Tübingen

2012

Erklärung

Diese Dissertation wurde im Sinne von § 7 der Promotionsordnung vom 28. November 2011 von Herrn Prof. Dr. Achim Hartschuh betreut.

Eidesstattliche Versicherung

Diese Dissertation wurde eigenständig und ohne unerlaubte Hilfe erarbeitet.

München, den 30.03.2012

(Unterschrift des Autors)

Dissertation eingereicht am 30.03.2012
1. Gutachter: Prof. Dr. Achim Hartschuh
2. Gutachter: Prof. Dr. Alf Mews
Mündliche Prüfung am 24.05.2012

Abstract

Optical microscopy is widely used to visualize small structures that can not be seen by the unaided human eye. On the nanoscale, however, the diffraction limit prevents conventional microscopy from studying materials with the required spatial resolution. This work reports on tip-enhanced near-field optical microscopy (TENOM), a technique that allows for nanoscale optical imaging with high detection sensitivity. It exploits the locally enhanced optical fields at a laser illuminated metal tip that acts as an optical antenna. The main aims of this work are to develop a better understanding of the signal enhancement mechanisms in TENOM and to apply the technique to different 1D semiconducting nanostructures, namely single-walled carbon nanotubes (SWCNTs) and cadmium selenide nanowires (CdSe NWs).

In the first part, the angular distribution of photoluminescence (PL) emission from SWCNTs with and without the optical antenna is studied by imaging the back focal plane of the microscope objective. Using model calculations, it is shown that the PL of SWCNTs on a dielectric substrate can be described as emission from a single in-plane point dipole despite the quasi 1D structure of the nanotubes. The signal enhancement due to the antenna is connected to a substantial redistribution of the angular emission. A procedure for the individual quantification of the excitation and radiation rate enhancement factors is developed and applied to the experimental data.

In the second part, nanoscale optical imaging of CdSe NWs using TENOM is presented for the first time. Spectrally resolved imaging reveals different band gaps for different NWs and variations of the PL energy and intensity along single NWs with energy gradients up to $1\,\mathrm{meV\,nm^{-1}}$. Even bundled NWs can be spatially resolved by their PL and Raman signals.

The third part reports on the angular and spectral emission properties of CdSe NWs and the tip-induced changes in a TENOM measurement. In contrast to SWCNTs, two perpendicularly oriented point dipoles are required to describe the angular intensity distribution of PL emission from CdSe NWs sufficiently. Again, tip-induced signal enhancement is accompanied by a spatial redistribution of the emission. The theoretical description is more complex than in the case of SWCNTs, because different radiating dipole orientations in the NW have to be taken into account that can interact with the tip. Finally, investigations of the tip-sample distance dependence of PL and Raman scattering are presented and discussed.

Kurzzusammenfassung

Optische Mikroskopie ist eine weit verbreitete Technik um kleine Strukturen sichtbar zu machen, die mit bloßem Auge nicht erkennbar sind. Im Nanometerbereich verhindert jedoch die Beugungsgrenze konventioneller Mikroskope, dass Objekte mit der nötigen Ortsauflösung untersucht werden können. Diese Arbeit handelt von spitzenverstärkter Nahfeldmikroskopie (engl.: tip-enhanced near-field optical microscopy, TENOM), welche optische Abbildungen mit einer Nanometerauflösung ermöglicht. Dabei werden lokal verstärkte optische Felder an einer Laser-beleuchteten Metallspitze, die als optische Antenne fungiert, genutzt. Ziel der Arbeit ist es, ein verbessertes Verständnis der Signalverstärkungsmechanismen in TENOM zu erreichen, und die Methode auf verschiedene 1D Halbleiternanostrukturen, d.h. einwandige Kohlenstoffnanoröhren (engl.: single-walled carbon nanotubes, SWCNTs) und Cadmiumselenid Nanodrähte (engl.: cadmium selenide nanowires, CdSe NWs), anzuwenden.

Im ersten Teil wird die winkelabhängige Abstrahlung der Photolumineszenz (engl.: photoluminescence, PL) von SWCNTs mit und ohne optischer Antenne anhand von Abbildungen der hinteren Fokalebene des Mikroskopobjektivs untersucht. Mit Hilfe von Modelrechnungen wird gezeigt, dass die PL von SWCNTs auf einem dielektrischen Substrat durch Strahlung eines einzelnen, in der Substratebene liegenden Punktdipols beschrieben werden kann, obwohl die Nanoröhre quasi eindimensional ist. Die durch die Antenne verursachte Signalverstärkung ist an eine Umverteilung der winkelabhängigen Abstrahlung gekoppelt. Es wird gezeigt, wie die Verstärkungsfaktoren für Anregungs- und Abstrahlungsrate anhand der experimentellen Ergebnisse unterschieden und quantifiziert werden können.

Im zweiten Teil werden zum ersten Mal hochaufgelöste optische TENOM-Messungen an CdSe NWs gezeigt. Spektral aufgelöste Bilder machen sowohl verschieden große Bandlücken unterschiedlich dicker NWs als auch Energie- und Intensitätsvariationen entlang einzelner NWs mit Energiegradienten bis zu $1\,\mathrm{meV\,nm^{-1}}$ sichtbar. Sogar gebündelte NWs können anhand ihrer Raman- und PL-Signale räumlich aufgelöst werden.

Im dritten Teil dieser Arbeit werden die spektralen und winkelabhängigen Abstrahleigenschaften von CdSe NWs und der Einfluss der in TENOM verwendeten Goldspitzen auf diese behandelt. Im Gegensatz zu den SWCNTs werden zwei orthogonal zueinander ausgerichtete Punktdipole benötigt, um die winkelabhängige Abstrahlungsverteilung der PL der Nanodrähte gut zu beschreiben. Auch hier wird die Signalverstärkung durch die Spitze von einer räumlichen Umverteilung der Strahlung begleitet. Die theoretische Beschreibung

ist komplexer als im Falle der SWCNTs, weil mehrere strahlende Dipole unterschiedlicher Ausrichtung im NW berücksichtig werden müssen, die mit der Spitze in Wechselwirkung treten können. Schließlich werden die Untersuchungen der PL und Ramanstreuung in Abhängigkeit des Abstandes zwischen Spitze und NW vorgestellt und die Ergebnisse diskutiert.

Contents

1 Introduction and motivation

Today, nanosized materials are object to a huge field of science and technology, the so called nanotechnology [1]. Many nanomaterials show unique mechanical, optical and electrical characteristics, which makes them highly interesting and promising candidates for electrical and optical nanotechnological devices. The properties crucially depend on the size and the shape of the material, and as a consequence they can be controlled and tailored systematically, which is a key parameter for potential applications. For the realization of the nanocomponents, accurate methods for the production and the characterization are needed. During the past decade many synthesis methods have been developed which now provide excellent materials in a highly controllable way. These methods include top-down and bottom-up schemes, wet and non-wet chemistry, as for example lithography or chemical synthesis methods.

Optical microscopy and spectroscopy are indispensable tools for the investigation and characterization of all kinds of materials since they provide valuable information on material composition, structure and dynamics. To study nanostructures on their relevant length scales down to few nanometers, however, techniques that provide nanoscale resolution and a high detection sensitivity are required. Unfortunately, the resolution of classical optical microscopy is limited by diffraction, that means roughly to about $\lambda/2$. For light in the visible regime that is around 200-300 nm, which is often dissatisfying when studying nanomaterials which are usually considerably smaller. Other techniques providing the necessary resolution are for example transmission electron microscopy (TEM), atomic force microscopy (AFM) or scanning tunnelling microscopy (STM). They can give informations about e.g. the chemical composition, the crystal structure and the topography with atomic resolution [2–5]. However, optical properties like fluorescence emission or Raman scattering are not accessible.

Consequently, overcoming the diffraction limit of optical microscopy has been a key issue, and within the last decades several schemes have been developed to solve it. These techniques can be divided methodological into those that work with the far-field of the sample only, and those that exploit a sharp probe to work in the near-field of the sample. To the first group belong, e.g., stimulated emission depletion (STED), photoactivated localization microscopy (PALM), fluorescence photoactivated localization microscopy (FPALM) and stochastic optical reconstruction microscopy (STORM) [6–9]. The latter group are scanning near-field optical microscopy (SNOM) schemes like aperture-SNOM, scattering SNOM or tip-enhanced near-field optical microscopy (TENOM) [10–12]. Today, the high-

est optical resolution and detection sensitivity on surfaces is achieved with tip-enhanced near-field optical microscopy [13]. TENOM exploits the enhanced electric fields in the vicinity of a sharp laser-illuminated metal probe to locally increase the optical response from the sample. Raster-scanning the tip and simultaneous detection of the signal from the sample results in optical images with a spatial resolution up to 10 nm combined with single molecule sensitivity for both fluorescence and Raman spectroscopy [12]. The tip can enhance the exciting laser field and the vacuum field, resulting in a substantial amplification of the optical signals. The enhancement mechanisms are not yet fully understood, and since the enhancement of excitation and radiation can be usually not distinguished in the observed signal, it is quite difficult to quantify them. At this point further investigations are thus highly desired.

For potential optical applications, nanomaterials with semiconducting character are of high interest, because they exhibit special optical properties resulting from the presence of a band gap. Semiconducting (quasi-) 1D nanostructures in which electronic states can be controlled by quantum confinement, such as carbon nanotubes and other inorganic nanowires, will play an important role as basic components for optoelectronis and photovoltaics [14–16].

Single-walled carbon nanotubes exhibit exceptional optical and electrical properties that result from their unique structure, which is made of carbon atoms arranged like a very thin hollow cylinder that can be as long as centimeters. Today, many potential applications have been realized and the research is still going on [17, 18]. In the meantime, TENOM is a well established tool to investigate single-walled carbon nanotubes, it has been applied to single and bundled nanotubes, and has resulted in a manifold of valuable informations because of the optical resolution and the detection sensitivity [12, 19–24]. Although it is accepted that the signal enhancement arises from the highly confined electrical fields at the tip apex, the enhancement mechanisms are still not investigated qualitatively.

Inorganic semiconducting nanowires are promising candidates as building blocks in nanoscale optoelectronics, photovoltaics, and sensing devices owing to their unique physical properties [16, 25, 26]. In thin cadmium selenide (CdSe) nanowires, diameter-dependent quantum confinement controls the electronic band gap energy, a key parameter in potential applications [27]. In addition, the band gap energy is known to depend on the crystal phase, since wurtzite and zinc-blende phase are stable in the nanowires [16, 28]. Nanoscale phase variations with alternating wurtzite and zinc-blende segments along the nanowires have been suggested as the origin of the large spectral width of the observed photoluminescence bands [29]. Despite the outstanding probabilities of modern high resolution optical microscopy techniques, only a few experiments with sub-diffraction resolution have been performed on nanowires in the quantum-confinement regime up to now [30–33]. The extension of TENOM as a standard technique also for inorganic nanowires would lead to a further progress in the investigation and understanding of their optical properties on nanometer length scales.

This work therefore aims at two main points. The first is a better understanding of the enhancement mechanisms in tip-enhanced near-field optical microscopy including a separation of the excitation and the radiative rate enhancement described by the enhancement factors F_{ex} and F_{rad}. The second goal is the establishment of TENOM as a tool for the investigation and characterization of quasi 1D structures beyond SWCNTs, i.e. for inorganic nanowires like CdSe nanowires. The following questions have thus been put up: (i) How does the near-field probe influence the emission of SWCNTs regarding spectral and angular aspects? (ii) How can the individual rate enhancement factors F_{ex} and F_{rad} be separated and quantified? (iii) Is TENOM applicable to inorganic semiconductors with high image contrast and sub-diffraction resolution? (iv) How does the tip influence the emission of the inorganic nanowires, again regarding spectral and angular characteristics?

The written form of this thesis is arranged as follows: First an overview of the required basics is given in chapter 2, regarding the physical properties of the sample materials SWCNTs and CdSe nanowires. High resolution optical microscopy will be introduced in chapter 3, and the experimental details will be described in chapter 4.

The presentation of the experimental results and the corresponding interpretations and discussions will start from chapter 5. Here, the interaction mechanisms between the gold tip and single semiconducting SWCNTs are addressed. For the investigations of the angular emission of photoluminescence from nanotubes and the influence of the tip, the radiation pattern in the back focal plane of the objective has been imaged. The comparison with calculated patterns allows for a detailed data analysis which reveals the dipolar nature of the emission. It will be shown that the signal enhancement provided by the tip is connected to a redistribution of the angular emission. The radiation pattern can also be utilized to extract the rate enhancement factors for excitation and radiative rate, F_{ex} and F_{rad}.

In chapter 6, TENOM measurements on CdSe nanowires are presented which show that a high signal enhancement accompanied by a spatial resolution of about 20 nm is possible for both PL emission and Raman scattering. Hyperspectral imaging further provides full spectral details about the sample material. Variations of the photoluminescence intensity and energy along the nanowires are revealed that are otherwise hidden due to spatial averaging. It will be shown that by using TENOM even bundled CdSe nanowires can be spatially resolved according to their photoluminescence and Raman signals.

The influence of the near-field probe on the spectral and angular emission properties of CdSe nanowires is discussed in chapter 7. Owing to quantum confinement effects the photoluminescence of CdSe nanowires is blue-shifted with respect to the bulk emission if the diameter is smaller than twice the exciton Bohr radius. In addition variations in the crystal structure result in energy shifts. Observations of emission spectra during the approach of the near-field probe allow for correlating the signal enhancement and possible shifts in the PL energy to the tip-sample distance. The dependence of the signal enhancement for

photoluminescence as well as Raman scattering on the tip-sample distance are deduced. The discussion of the occasionally observed spectral shift in the PL energy reveals the complexity of the coupled tip-sample systems, which consequently must result in a careful interpretation of the TENOM data. The second part of the chapter gives attention to the angular emission of photoluminescence emanating from the CdSe nanowires. Radiation patterns from the nanowires were measured and the results compared to theoretical patterns. In contrast to the SWCNTs, a description with a single dipolar emitter is not sufficient to reproduce the angular emission characteristics, and the theoretical treatment must thus be further extended. The signal enhancement due the near-field probe is again found to be connected to a spatial redistribution of the emission, which is shown in a series of radiation patterns measured during tip approach.

Finally, the key results obtained during this thesis are summarized, and a short outlook provides ideas for further experiments and applications for TENOM.

Two appendices are attached to the main part of the work in which several experiments regarding the improvement and the applicability of TENOM are presented. In appendix A a way to improve the used sharp gold tips is demonstrated, which aims at maximizing the field enhancement and confinement at the tip apex by fabricating surface plasmon Bragg reflectors all around the tip in a well-defined distance to the tip apex to mimic finite length antenna structures. Stronger signal enhancement results in higher detection sensitivity and higher resolution and is thus in high demand.

Appendix B deals with TENOM measurements on substrates other than a glass substrate. The first example is a TEM grid carrying a thin carbon film. The combination of TENOM and TEM investigations on the same object would be of great value for researchers, but usually this is not possible because of the differing substrate requirements. As the first example it is thus shown, that TENOM is also possible on a typical TEM substrate. The second example is a rough gold film sputtered onto a glass substrate. Rough metal films are known as substrates for surface-enhanced Raman spectroscopy. Since metals in contact with an emitter quench the photoluminescence, they are not used to enhance fluorescence. It was found however, that the quasi 1D structures lying on a rough film still exhibit small luminescent regions. TENOM on such a sample would allow for the combination of surface- and tip-enhancement or a gap-mode configuration, and much higher enhancement factors are expected [34].

2 Quasi 1D semiconducting materials

Semiconducting (quasi-) 1D nanostructures, such as carbon nanotubes and inorganic nanowires, will play an important role in future applications, for example as basic components for nanotechnological devices. Nanotubes and nanowires are promising candidates as building blocks in nanoscale optoelectronics, photovoltaics, and sensing devices. The unique physical properties of these nanomaterials and, in particular, their strong correlation with structural parameters attracted considerable scientific interest [14–16, 35, 36]. The dependence of the optical and electrical properties on structural parameters can be exploited to tailor the material properties for different applications. One-dimensional structures are of special interest since they are required for signal and carrier propagation as well as transport applications. While zero-dimensional components do not allow any directional action and two- or three-dimensional systems have no preferred directivity, the 1D structures allow for well designed devices based on spatial transport. The 1D materials may act as wires on the nanoscale, for the communication between spatially separated blocks or for building up complex two- and three-dimensional networks.

During this work, two quasi one-dimensional semiconducting nanomaterials have been investigated, namely single-walled carbon nanotubes and inorganic CdSe nanowires. Both materials are very thin with diameters of about 0.85 nm for the nanotubes and 4-24 nm for the nanowires. The spatial confinement in two dimensions leads to quantum confinement of the electronic states, if their diameter is in the range or smaller than twice the respective exciton Bohr radius. For a semiconducting carbon nanotube, the exciton Bohr radius is always a little bigger than its diameter [37]. A huge number of possible applications have been suggested exploiting the outstanding properties of single-walled carbon nanotubes. Besides this, they also represent a highly interesting model system that allows for the investigation of the basic physics of one-dimensional systems. Since the intrinsic properties of a nanotube are given by its structure, which is usually uniform along its complete length, it represents a well-defined model material featuring unique properties. The exciton Bohr radius of CdSe is $r_{Bohr} = 5.6\,nm$, which allows for studying quantum confinement effects depending on the size, since CdSe nanowires with diameters down to few nanometers can be synthesized [29, 38]. It further constitutes a way to control the electronic band gap energy, a key parameter in potential applications.

This chapter will give a basic overview of the used sample materials, their synthesis and properties. Section 2.1 provides a short introduction into the field of single-walled carbon nanotubes (SWCNTs), especially with regard to the optical properties of semiconducting

SWCNTs. Section 2.2 then provides an introduction into the field of CdSe nanostructures with the main focus on the quasi one-dimensional nanowires, their synthesis and optical properties.

2.1 Single-walled carbon nanotubes

SWCNTs are hollow cylinders built up from sp^2 hybridized carbon atoms only. They have a small diameter of down to 0.5 nm, but can be as long as centimeters. Therefore, their aspect ratios are typically very large and they can thus be regarded as quasi one-dimensional nanostructures. The structure of a nanotube, that is the arrangement of the carbon atoms, defines its characteristic mechanical and electronic properties. All the carbon atoms forming a carbon nanotube are surface atoms, which makes SWCNTs very sensitive to their environment and changes or irregularities therein.

2.1.1 Structural properties

Conceptionally, the unit cell of a single-walled carbon nanotube can be regarded as a very thin and hollow cylinder that is rolled up from a single sheet of sp^2 hybridized carbon atoms, namely a piece of single layer graphene. The graphene sheet can be rolled up in different ways resulting in nanotubes with different structures, denoted as their chirality, which defines their particular mechanical, electronic and optical properties. The chirality of a nanotube is described unambiguously by two numbers n and m with $n, m \in \mathbb{N}$, usually written as chiral index (n, m). This index is defined by the nanotube's circumferential vector expressed in multiples of the lattice vectors of graphene. Three different kinds of carbon nanotubes are distinguished regarding their chirality: Chiral nanotubes have two indices n, m with $m \neq n$ and $n, m \neq 0$. In zig-zag nanotubes one index equals zero and in armchair nanotubes n equals m. In figure 2.1, the described concept of nanotube structures is shown for a (6,5), a (8,0) and a (5,5) nanotube exemplary (taken from reference [39]).

The circumferential vector $\vec{C}_h$ of the nanotube is given by

$$\vec{C}_h = n \cdot \vec{a}_1 + m \cdot \vec{a}_2,$$

with the graphene lattice vectors $\vec{a}_1$ and $\vec{a}_2$ as indicated in figure 2.1. The translational vector $\vec{T}$ is the length of the unit cell along the nanotube axis, given by

$$\vec{T} = \frac{2m+n}{d_r} \cdot \vec{a}_1 - \frac{2n+m}{d_r} \cdot \vec{a}_2$$

where d_r is the greatest common devisor of $(2m+n)$ and $(2n+m)$. The diameter d of a nanotube is given by $d = \vec{C}_h/\pi$. Zig-zag and armchair nanotubes are always achiral and exhibit a symmetry axis along the nanotube length, in contrast to the chiral nanotubes which can be left- or right-handed. A carbon nanotube with $(n-m)mod3 = 0$ is metallic,

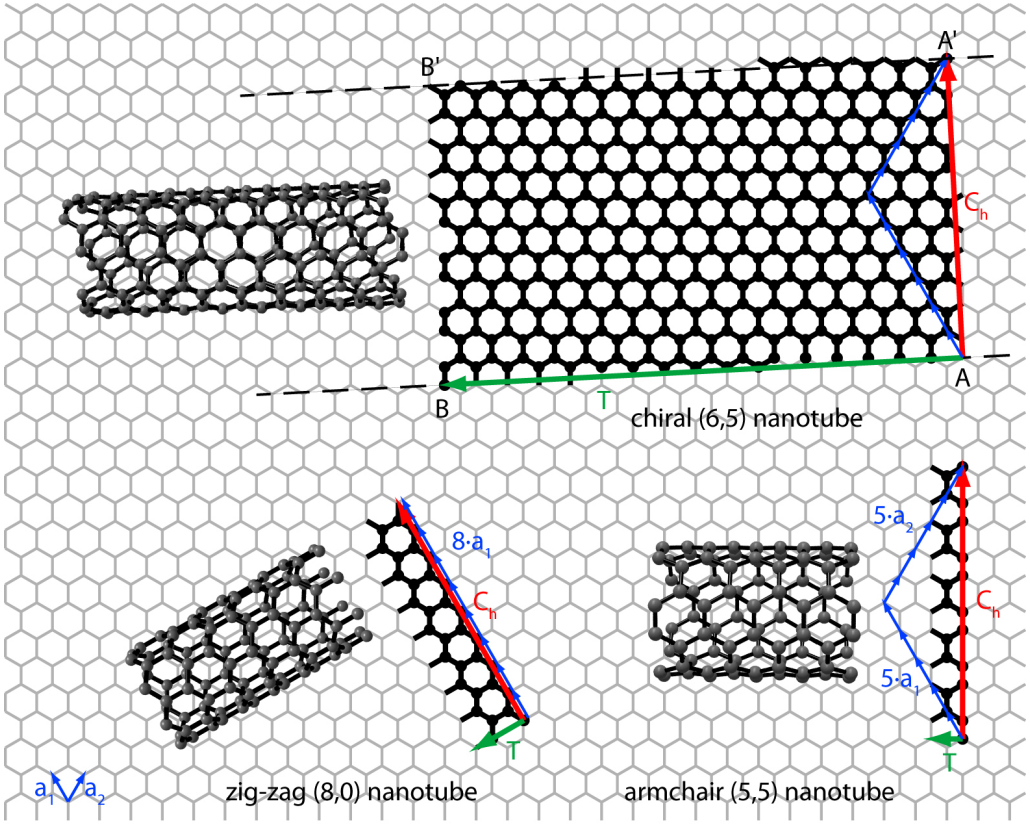

Figure 2.1: Depending on the indices n and m three kinds of carbon nanotubes are distinguished: chiral nanotubes with $m \neq n$ and $m, n \neq 0$, zig-zag nanotubes with $n = 0$ or $m = 0$ and armchair nanotubes with $n = m$. As examples a (6,5), a (8,0) and a (5,5) nanotube are shown here. The lattice vectors $\vec{a}_1$ and $\vec{a}_2$ of the underlying graphene sheet are indicated. The circumference of the resulting nanotubes is given by $\vec{C}_h$, the perpendicular translational vector of a unit cell by $\vec{T}$.

otherwise it is semiconducting and exhibits a direct band gap. In the following, only semiconducting SWCNTs are discussed because all nanotubes investigated in this work were semiconducting. Further details beyond the following short overview can be found in literature [14, 39–42].

2.1.2 Optical properties

Semiconducting carbon nanotubes have a direct band gap and are thus luminescent showing emission in the near-infrared. In addition they exhibit strong Raman scattering as it is typical for many carbonaceous materials.

Photoluminescence

For a basic understanding of the optical properties of single-walled carbon nanotubes a simple zone-folding approximation based on the graphene band structure is well suited [41]. Under the assumption of free charge carriers this results in a band structure and a correlated density of states (DOS) as depicted in figure 2.2. The DOS shows van Hove singularities which are typical for quasi one-dimensional systems.

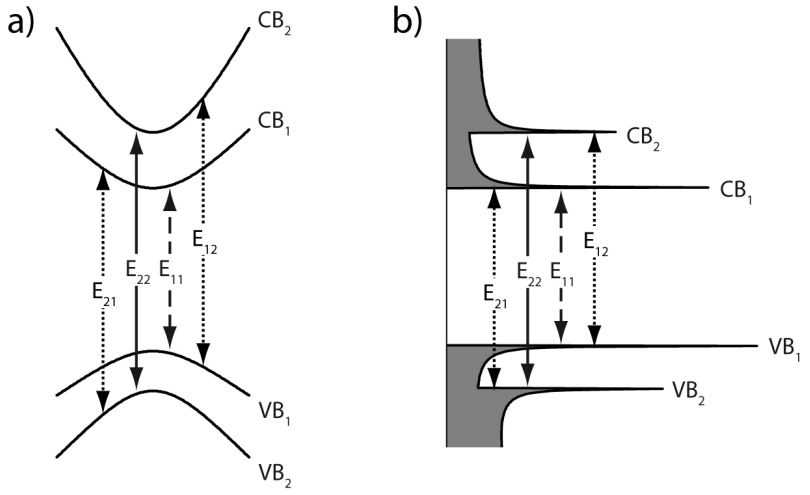

Figure 2.2: a) The band structure of semiconducting SWCNTs exhibits a band gap between the highest valence band VB_1 and the lowest conduction band CB_1, denoted as E_{11}. b) The density of states (DOS) including van Hove singularities. Optical transitions with E_{ii} are polarized along the carbon nanotube. Transitions with E_{ij} are polarized perpendicular and are usually strongly suppressed because of depolarizations effects.

Optical transitions in SWCNTs are strongly polarization dependent. The solid arrows in figure 2.2 represent transitions between van Hove singularities with the same index E_{ii} which are polarized along the nanotube axis. On the other hand, cross-polarized transitions E_{ij} as indicated by the dashed arrows, are polarized perpendicular to the nanotube axis. For propagating electromagnetic fields these transitions are screened efficiently by the polarizability of the nanotube, so usually excitation via $E_{i\neq j}$ can be neglected. As a consequence a SWCNT is excited efficiently only if the incoming light is polarized along the nanotube axis. Vice versa the emission of a photoluminescence photon via the lowest possible transition, E_{11}, is polarized in the same manner. For a more detailed description, curvature effects have to be taken into account whose influence increases with decreasing diameter. However, for a basic understanding of the optical properties of carbon nanotubes the zone folding technique is sufficient.

In quasi one-dimensional carbon nanotubes Coulomb interactions between free charge carriers can no longer be neglected. As a consequence the free-particle picture introduced above has to be replaced by an exciton picture since optical excitation creates excitonic states rather than free particles. Repulsive electron-electron interaction results in an in-

crease of the band gap by E_{BGR}, which is known as band gap renormalization. Attractive electron-hole interactions compensate E_{BGR} to some extent, resulting in excitonic states below the continuum state E_{11}^{∞}. The exciton binding energy of the lowest bright excitonic state E_{11}^{bright} is denoted as E_{bind} and is very large for SWCNTs. Binding energies between 300-400 meV have been determined using one- and two-photon luminescence [43]. The strongly bound excitons have an exciton Bohr radius in the order of few nanometers. They can be regarded as neutral quasi-particles that are delocalized along the circumference of the nanotube and, to some extend, mobile along its long axis. The diffusion length of excitons in SWCNTs on a dielectric surface is around 100 nm [44, 45]. For low exciton densities they are assumed to behave like independent particles because of their rather small coherence length and lifetime [46].

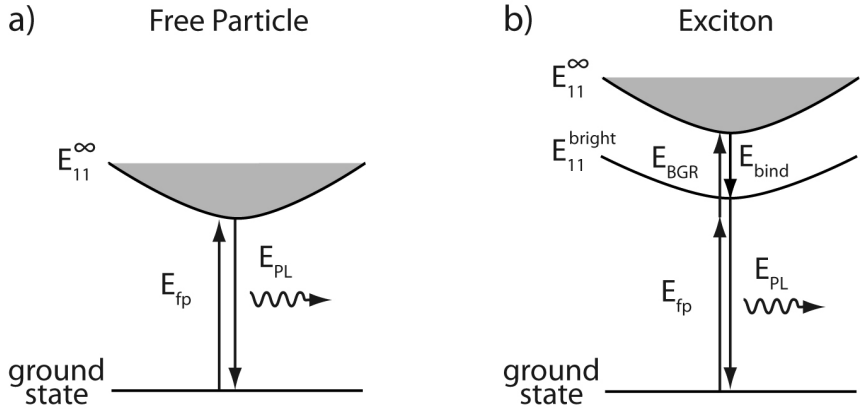

Figure 2.3: a) Free-particle and b) exciton picture of semiconducting SWCNTs. Coulomb interactions disregarded in the free-particle picture can not be neglected in 1D SWCNTs. Electron-electron repulsion leads to an increase of the band gap by E_{BGR}, electron-hole attraction results in excitonic states below the continuum state E_{11}^{∞}. The exciton binding energy of the lowest bright excitonic state E_{11}^{bright} is denoted as E_{bind}.

Photoluminescence (PL) in semiconducting carbon nanotubes results from the recombination of the bright E_{11}^{bright} exciton, which is usually observed in the near-infrared. As mentioned above the absorption and emission energies depend on the chirality of the nanotube. The energy of the band gap scales approximately inversely with the diameter d of a nanotube, which means that the transition energy increases with decreasing nanotube diameter. As a consequence, the diameter, and thus the chirality described by (n, m), can be deduced from the energy of the photoluminescence photons. Since the SWCNTs are very thin and contain only surface atoms, they are highly sensitive to their environment and changes therein. Dielectric screening depending on the dielectric constant of the surrounding decreases E_{BGR} as well as E_{bind} resulting in an overall red-shift of the observed PL energy. Representative PL spectra are shown in figure 2.4 a for a (6,5) and a (9,1) nanotube. The full width at half maximum of these bands is around 25 nm ($\approx$ 30 meV).

For optical investigations usually the E_{22} transition is excited. SWCNTs have a very small Stoke's shift which makes excitation and emission detection from the same transition very

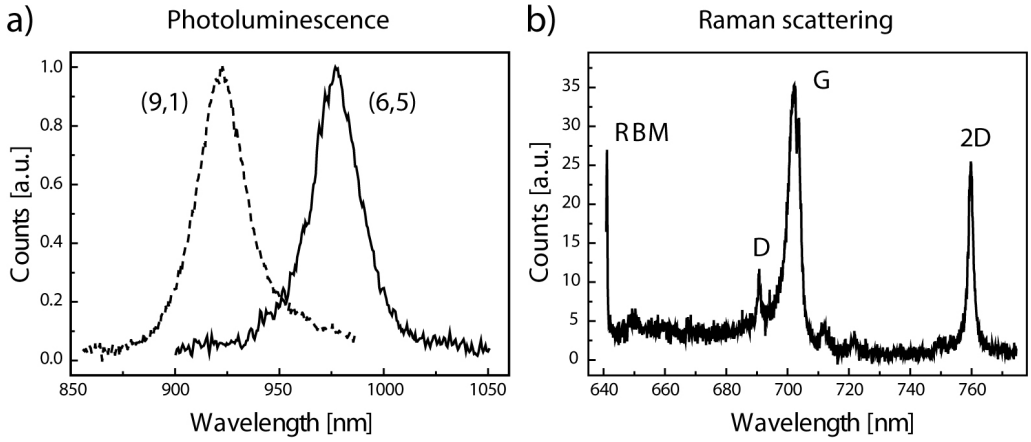

Figure 2.4: a) Photoluminescence spectra of a (6,5) and a (9,1) nanotube exhibiting emission in the near-infrared. b) Raman spectrum of a SWCNT on glass. The D, G and 2D (G') bands are visible. The RBM mode appears only partly in the spectral detection window since it lies close to the laser energy.

difficult because of their nearly identical wavelengths. An excited higher state decays rapidly, efficiently and non-radiatively to the E_{11} state from which photoluminescence can be emitted [47, 48]. Radiative recombination is in competition with non-radiative decay channels on the time scale of several tens of picoseconds. The quantum yield Q of an emitter is given by

$$Q = \frac{\mathrm{k_{rad}}}{\mathrm{k_{rad}} + \mathrm{k_{nr}}}, \tag{2.1}$$

with the radiative rate $\mathrm{k_{rad}}$ and the non-radiative rate $\mathrm{k_{nr}}$. Since $\mathrm{k_{rad}}$ is rather low for carbon nanotubes (in the range of 0.1 to $1\,\mathrm{ns}^{-1}$), non-radiative relaxation dominates in SWCNTs. The oscillator strength of an exciton, which is proportional to the radiative rate, is small because of the ultrafast dephasing and the respective short coherence length [49]. The resulting quantum yield is rather small in the range of only few percent or less. Quenching sites like defects further reduce the quantum yields, and therefore highest values were found for high quality SWCNTs [14]. Besides defect induced quenching, efficient energy transfer between nanotubes of different chiralities has been observed where energy is transferred to lower band gap SWCNTs [50]. Also energy transfer to metallic nanotubes which exhibit no band gap and thereby offer non-radiative decay channels occurs, which leads to efficient quenching of the photoluminescence. This is important since SWCNTs tend to bundle together due to strong van der Waals interactions. Therefore, they have to be thoroughly separated for the purpose of optical investigations, which can be done by the help of surfactant materials.

Raman scattering

Raman scattering of carbon nanotubes is unaffected by these quenching and bleaching issues of photoluminescence. As a well established tool for the investigation of graphitic

materials, Raman spectroscopy provides informations on structural properties like the degree of doping, functionalization and, in the case of carbon nanotubes, the chirality.

The Raman spectrum of SWCNTs contains four main features, namely the radial breathing mode (RBM), the defect related D band, the G band, and the G' band. A representative spectrum is depicted in figure 2.4 b. The RBM is an oscillation of the diameter and unique to carbon nanotubes. Its frequency is related to the diameter of the nanotube and thus to its chirality. The measurement of an RBM excitation spectrum is widely used for the assignment of (n, m). Owing to its low energy a double resonance process is possible if the laser photon and the scattered photon meet an E_{ii} transition. In this case the RBM will dominate the Raman spectrum, while it is barely detectable for off-resonance conditions. The D-band at around $1350\,\mathrm{cm}^{-1}$ requires scattering by a defect to preserve momentum conservation and is thus only visible in non-perfect nanotubes. It is often used as a measure of defect concentration since its intensity increases with increasing number of defects [51, 52]. The G band at around $1590\,\mathrm{cm}^{-1}$ typically dominates the Raman spectrum of carbon nanotubes. In imaging techniques usually the G band is measured since it provides the best signal-to-noise ratio [53]. In semiconducting SWCNTs it consists of two modes, namely the G^+ mode which is connected to a LO phonon and the G^- mode connected to a TO phonon. Because of symmetry reasons the G^- component is slightly shifted towards lower energies depending on the nanotube diameter. The G' band (also 2D band) is the second order process of the D band but does not require defect scattering and is thus always allowed.

Raman spectroscopy has a rather low sensitivity because of the typically small Raman cross sections. Therefore, resonant Raman scattering with significantly increased Raman cross sections is required to observe Raman scattering from single carbon nanotubes. The Raman process is resonant if the energy of either the excitation laser or of the scattered photon matches one of the electronic transitions E_{ii}. Beyond this the signal intensity can be further increased drastically using enhancing techniques like surface or tip enhanced Raman scattering (SERS, TERS).

2.2 Inorganic semiconducting nanowires: cadmium selenide

Cadmium selenide (CdSe) attracted high interest in the past decades and is thus a very well studied semiconductor material. Especially the advent of its nanomaterials gave rise to a burst of scientific research, for example the investigation of quantum confinement effects, complemented by theoretical modelling and followed by the suggestion and implementation of manifold technological applications. Owing to the high toxicity of CdSe there are only rare applications of the bulk material. Nanomaterials, on the other hand, feature many (potential) applications, which range from optoelectronic devices like light emitting diodes, photovoltaics over single electron transistors and sensing applications to bioimaging in form

of fluorescent labels, Raman labels and so on [26, 54–59]. This fact makes them highly interesting in research and nanotechnology despite their toxicity.

In this section, the inorganic semiconductor CdSe and especially its nanoscale representatives will be introduced. After a short summary of some basic information including the electronic band structure and the crystal structure, a more detailed introduction into the nanomaterials will be given. The main focus lies on the quasi one-dimensional nanowires since they served as sample material for one main part of this work, namely the application of tip-enhanced near-field optical microscopy to 1D inorganic nanowires.

2.2.1 Electronic band structure

CdSe is a II-VI semiconducting material consisting of twofold negative selenium anions and twofold positive cadmium cations. At room temperature it has a direct band gap of 1.74 eV at the Γ point of the first Brillouin zone [29,60]. With decreasing temperature the band gap increases up to 1.84 eV at 0°C. The highest valence band state originates from the selenium 4p orbitals, the lowest conduction band from cadmium 5s orbitals. The band structure as calculated by Kobayashi et al. according to a semi-empirical tight-binding theory [61] is depicted in figure 2.5.

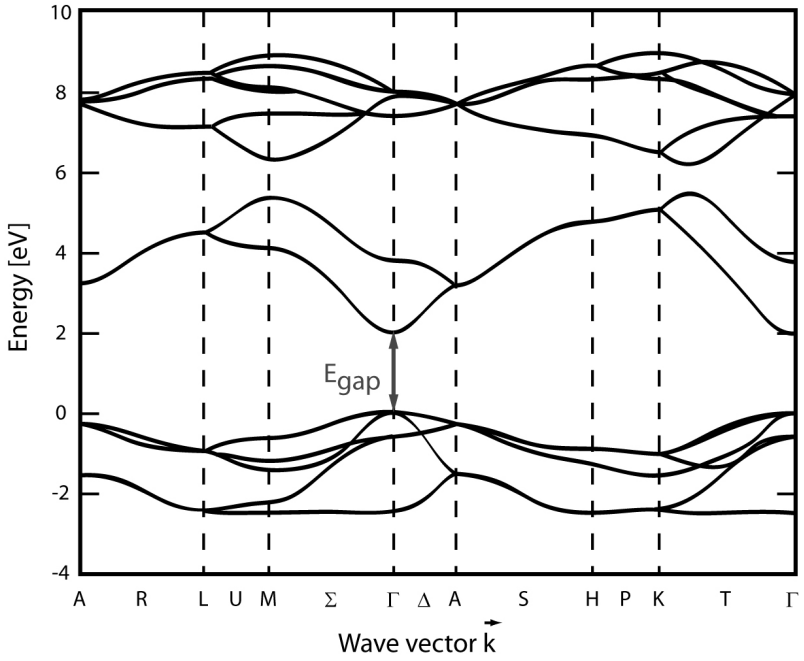

Figure 2.5: Schematic of the band structure of bulk CdSe (WZ) according to the semi-empirical tight-binding theory by Kobayashi [61]. The direct band gap at the Γ point is 1.74 eV at room temperature.

2.2.2 Crystal structure

The crystal structure of the bulk material cadmium selenide is the hexagonal wurtzite (WZ) structure. In its nanoscale versions also the cubic zinc-blende (ZB) structure is stable. Figure 2.6 shows the crystal structure of hexagonal WZ and cubic ZB symmetry with Cd^{2+} cations as blue spheres and Se^{2-} anions as red spheres. The energy difference between the two crystal structures is only about 2 meV/atom facilitating alternations between them in one dimensional nanowires [29]. A change from WZ to ZB structure or vice versa is realized by a simple rotation of 60° between the (0001) growth direction in WZ and the (111) direction in ZB. In zero dimensional nanocrystals either WZ or ZB structure is possible, depending on the synthesis conditions.

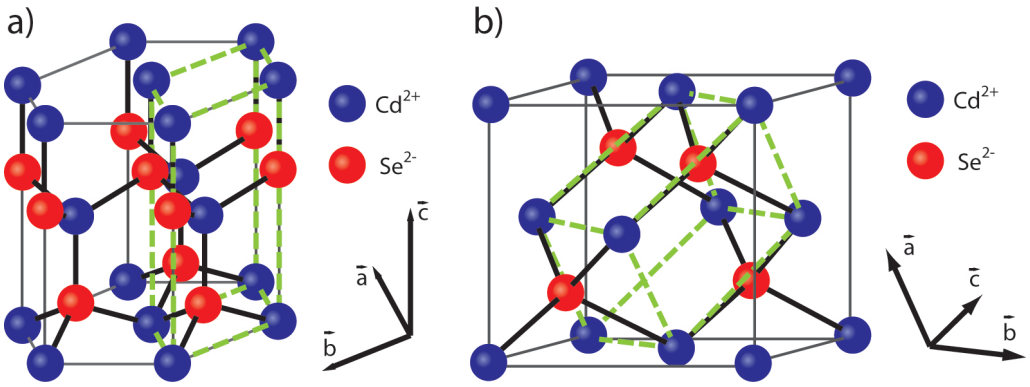

Figure 2.6: Crystal structure of CdSe. a) Hexagonal wurtzite structure and b) cubic zinc-blende structure. Both crystal structures are stable in CdSe nanostructures. Cd-cations are depicted as blue spheres and Se-anions as red spheres. The unit cells are marked by the dashed green boxes.

2.2.3 0D: Nanocrystals and quantum dots

Nanocrystals (NCs) are single crystalline nanomaterials with dimensions smaller than 100 nm. The characteristic properties of a material undergo interesting changes when the size of a particle becomes significantly smaller than this, which is typically the case in nanocrystals of only few nanometers diameter. If the diameter of the crystal is in the range or smaller than twice the size of the exciton, given by the exciton Bohr radius r_{Bohr}, the three dimensional spatial confinement leads to the so called quantum confinement. In the case of CdSe $r_{Bohr} = 5.6$ nm, which means that quantum confinement effects are expected for CdSe nanocrystals with a diameter below 10 nm. In this case the exciton is localized and the nanocrystal can be described as a quasi zero-dimensional structure, also called quantum dot. The quantum confinement leads to a spatial confinement of the electron and hole wavefunctions resulting in discrete electronic levels and transitions resembling atomic transitions.

Related to this quantization is an increasing blue shift of the absorption and the photoluminescence energies with decreasing crystal size. The Stokes shift of the emission is found to depend on the size of the nanocrystal [62]. The absorption and emission spectra of CdSe nanocrystals that are only few nanometers small have been measured by Kippeny et al. as shown in figure 2.7 a [63]. The blue shift of the absorption and emission bands with decreasing nanocrystal size is clearly visible.

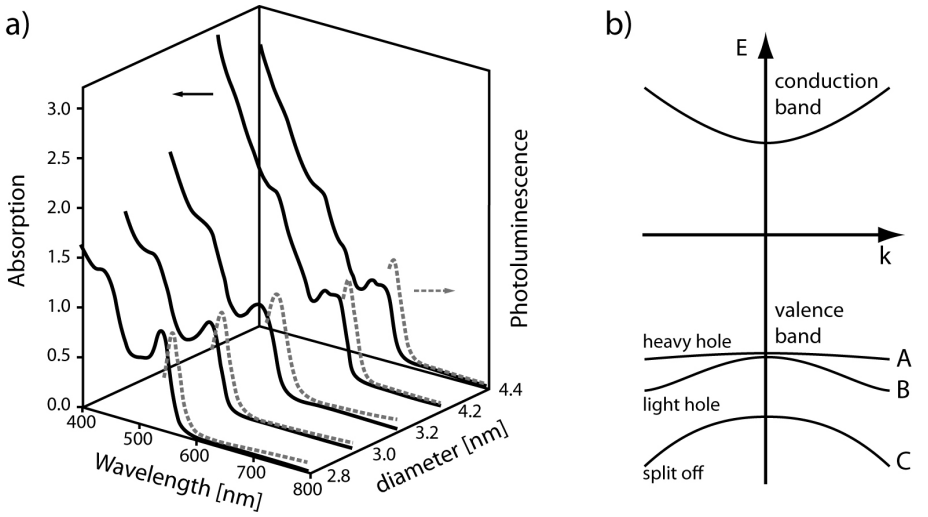

Figure 2.7: Optical transition in CdSe nanocrystals. a) With decreasing diameter the band gap of CdSe nanocrystals increases because of quantum confinement resulting in blue shifted absorption (solid lines) and emission (dotted lines) [63]. b) Conduction and valence band at the Γ point in the case of semiconductor nanocrystals. Spin-orbit coupling and crystal-field splitting result in splitting of the valence band into three sub-bands, namely A, B and C, that correspond to heavy hole, light hole and split-off bands.

In a direct band gap semiconductor nanocrystal with the band edges centered in the first Brillouin zone, the valence band splits into three sub-bands because of crystal-field splitting and spin-orbit coupling [60, 64–66] as depicted in figure 2.7 b. Conventionally, the band that corresponds to the heavy hole is denoted as A band, the light hole band as B band and the spin-off band as C band [64]. Since the spin-orbit splitting energy ($\lambda_{CdSe} \approx 420\,\mathrm{meV}$) is significantly higher than the crystal field splitting energy ($\Delta_{CdSe} \approx 25\,\mathrm{meV}$) the C band is located well below the A and B bands and consequently does not play a role in an emission process [64]. In contrast, the levels of the A band and the B band lie close together. Which of them exhibits the lower energy depends on the actual size and shape of the nanostructure owing to crystal field splitting and quantum confinement effects. In quasi 0D nanocrystals the A band that mainly originates from $4p_{x,y}$ orbitals represents the highest occupied level. This results in a degenerate transition dipole moment perpendicular to the c axis of the crystal (in plane polarization) [64, 67].

The size of the band gap does not only depend on the crystal size and shape but also on the surface properties of the nanostructure and its surrounding. The smaller the nanocrystal, the higher is the ratio of surface atoms and consequently also the influence of its surround-

ing. This gives an increasing influence to the ligands that are usually used for preparation and stabilization of the nanocrystals. The surrounding medium further has an impact because of the dielectric mismatch. The more the refractive indices differ from each other the bigger will be the change in the characteristic properties.

Therefore, the optical properties of such nanocrystals can be tuned throughout the whole visible spectrum in a highly controlled way. Today's synthesis methods allow for the preparation of structures with well designed optical and electrical properties. Owing to this fact together with the atom-like transitions, the nanocrystals are sometimes called artificial atoms.

One main drawback of nanocrystals regarding applications based on their photoluminescence is their low quantum yield (QY). Trap states at the crystal surface have been identified as the culprit because they are able to quench the photoluminescence efficiently via non-radiative Auger recombination. Usually, the trap state is not always occupied resulting in blinking on a time scale of up to seconds [68]. Consequently, a shell that shields the nanoparticle core is needed, which has been realized in so called core-shell systems. In these systems a second material with a higher band gap is used as thin shell prohibiting trap states. They typically reach quantum yields as high as 50% [69], but a quantum yield of unity is theoretically possible [70]. In addition, such a shell leads to further confinement of the excitonic states which has to be considered in the design of appropriate core-shell particles. A manifold of synthesis strategies exist, following either top-down or bottom-up approaches, based on wet or non-wet chemistry, and have been reviewed in literature [58, 63].

2.2.4 1D: Nanowires

Like carbon nanotubes also inorganic nanowires can be regarded as quasi one-dimensional if they are thin and long enough. Compared to the nanocrystals or quantum dots the quantum confinement is relaxed in one dimension in the case of nanowires. For CdSe nanowires with diameters of 3-6 nm the transition from 3D to 2D quantum confinement was found to take place at a length of about 30 nm [27]. As the diameter increases, quantum confinement in the other two dimension also relaxes. At a diameter of about 11 nm which is twice the exciton Bohr radius, the influence of quantum confinement is already moderate. Thick nanowires with significantly larger diameters show the same optical properties as the bulk material.

As a consequence of the relaxation of quantum confinement in one dimension, the B band crosses the A level. The B band mainly originates from $4p_z$ orbitals resulting in a polarization of the transition dipole moment along the c axis, which is usually the growth axis of these structures. In CdSe nanorods the crossover between the highest occupied levels was found to occur at an aspect ratio of about 1.3. The polarization dependence

of excitation as well as emission intensity for rods with aspects ratios greater than 1.3 follows a $\cos^2\theta$ law [71]. In PL scan images a CdSe nanorod or a short nanowire should thus appear as two-lobe pattern, when excited with a radially polarized doughnut mode, which has two opposite lobes with the required polarization along the nanowire axis. A doughnut mode and a PL image of a short nanowire is shown in figure 2.8 a and b. The excitation wavelength was $\lambda_{ex} = 633\,\text{nm}$. The corresponding topography of the nanowire measured by shear-force AFM is depicted in (c). The two observed intensity sites thus indicate a transition orientation as sketched by the arrow in b) which coincides with the orientation of the nanowire as observed in the topographical image. This confirms a transition orientation along the CdSe nanowire.

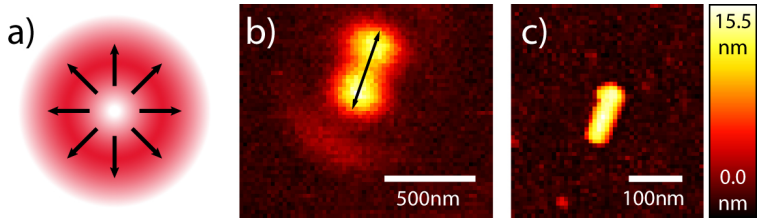

Figure 2.8: a) Schematic of the radially polarized doughnut mode used for excitation ($\lambda_{ex} = 633\,\text{nm}$). b) The photoluminescence image of a short CdSe nanowire shows two areas of maximum intensity which is expected for an absorption transition parallel to the substrate. The deduced dipole orientation is indicated by the arrow. It agrees with the long axis of the nanowire estimated from the topographical data in (c). The aspect ratio deduced from the topography is about 6, taking into account the finite dimensions of the probe.

Interestingly even if c is not the long axis of the nanowire, both excitation and emission show the same polarization dependence along the wire axis. This means that effects due to the dielectric mismatch between a CdSe nanowire and its surrounding are important regarding the polarization characteristics. For a field polarization perpendicular to the nanowire axis the induced charges counteract against the excitation field thereby attenuating it inside the nanowire. In the case of a field polarization parallel to the nanowires axis ideally no counteraction takes place [71].

Several studies addressed the question whether a free electron-hole pair arises upon absorption of a photon or if the excited state in CdSe nanowires has an excitonic character. The exciton binding energy was found to be 15 meV in bulk CdSe, but theory predicts exciton binding energies up to 300 meV in quantum confined systems [60, 72, 73]. Experiments on CdSe nanostructures confirmed binding energies in the range of 30 meV which means that excitons are stable up to room temperature [74]. The excitons in 1D nanowires are found to be mobile along the nanowire axis to some degree, with the mobility depending on the particular conditions like the potential landscape and the temperature [74, 75].

The blue shift ΔE_{gap} of the nanowires photoluminescence (compared to the bulk material) depends on the confinement in two dimensions and hence on the diameter d of the nanowire.

Several formulas to describe the dependence have been developed recently. The simple treatment of the excited state in a 1D structure according to the particle-in-a-box scheme predicts a $1/d^2$ dependence of ΔE_{gap} regarding free electron and hole [27]. Even though the same dependence is expected from a simple effective mass approximation that accounts for confinement effects, a better agreement with experimental data is found for a $1/d$ dependence [38]. Fitting a semi-empirical pseudopotential method to experimental values resulted in the relation 2.2 which suits the experiment quite well [27].

$$E_{gap}\,[\mathrm{eV}] = E^0_{gap} + \Delta E_{gap} \approx 1.74\,\mathrm{eV} + d^{-1.36}\,\mathrm{eV\,nm} \tag{2.2}$$

Here, the energy gap of the bulk material E^0_{gap} is 1.74 eV [27]. A plot of equation 2.2 is depicted in figure 2.9 for diameters ranging from 4-24 nm, because the diameters of the nanowires investigated in the course of this work are in this range.

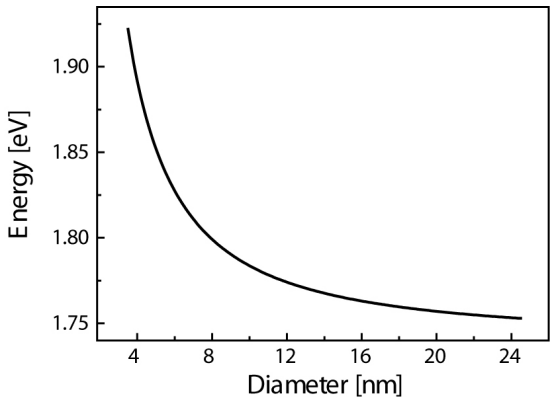

Figure 2.9: Plot of equation 2.2. The emission energy of CdSe nanowires depends on the diameter as shown here for the relevant diameter range of 4-24 nm occurring in the sample material investigated in this work. The band gap increases by up to 0.25 eV for the smallest depicted nanowire diameters compared to the bulk value.

As in the case of nanocrystals the band gap of a nanowire will be influenced by its surrounding environment. But since the ratio of surface atoms is smaller compared to a NC, this influence is expected to be considerably smaller.

A highly complicating factor regarding the energy shift of the band gap is that in 1D nanowires, both ZB and WZ crystal structure with different band gap energies are stable and present. Usually both structures do occur in the same nanowire and to date all synthesized nanowires reported in literature feature alternating ZB and WZ structure with randomly distributed segment lengths in the range of few nanometers. In addition the ZB structure allows for twinning, that is a stacking fault within the crystal structure. Figure 2.10 a shows typical CdSe nanostructures imaged by high-resolution electron transmission microscopy (HRTEM). The zoom in (b) reveals alternating ZB and WZ segments as well as twinning in the ZB segments as indicated by examples. Owing to this polytypism CdSe nanowires are so called heterogeneous homomaterials.

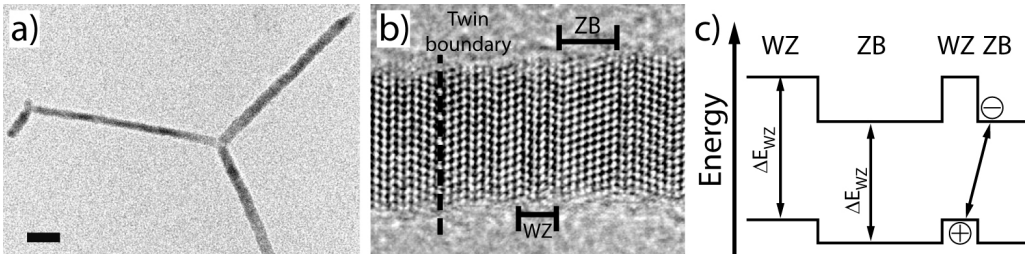

Figure 2.10: a) TEM image of a CdSe nanostructure with two branching sites. The scale bar is 20 nm. The high resolution TEM image in b) reveals a ZB/WZ admixture and twinning in ZB segments. c) WZ and ZB segments form type-II transition with staggered conduction and valence bands. The band gap of WZ is higher than that of ZB. TEM images have been measured in the group of Prof. Ch. Scheu at the LMU München.

Wurtzite and zinc-blende crystal structure form a type-II transition as depicted in figure 2.10 c, where the potential energy along alternating WZ and ZB segments is schematically drawn. The band gap of zinc-blende CdSe is slightly smaller than that of wurtzite CdSe. Because of the type-II transition character, electrons in the ZB part are energetically favourable whereas the holes should prefer the WZ sections. Consequently, an effective localization of charge carriers along the nanowire axis is conceivable. In NWs with short WZ and ZB segments in the range of few nanometers, however, the corresponding wavefunctions are predicted to overlap considerably at least at room temperature, for the valence band as well as for the conduction band [76]. The segments of typically synthesized CdSe nanowires are therefore not long enough to efficiently localize charge carriers.

The quantum yield of nanowires is typically about 0.1 % [26], which is low regarding possible applications. But also higher values up to 20 % have been reported in literature [77]. The full width at half maximum (FWHM) of the nanowire photoluminescence has been found to be rather broad, typically in the range of 100 meV [29]. Possible reasons for the broad bands are irregularities in diameter, ligands, electrostatic environment, interactions with the substrate, and the crystal structure [29, 74, 76].

A typical spectrum of a single CdSe nanowire with Raman and PL features is depicted in figure 2.11. The PL band at 670 nm (1.85 eV) is rather broad. The blue shift of the PL band frequency compared to the bulk material indicates an influence of quantum confinement. Besides photoluminescence also Raman scattering from CdSe nanowires is observed. Three Raman peaks are visible in the example spectrum, the strongest one at 641.3 nm (210 cm^{-1}) is related to the longitudinal optical phonon mode (LO). The less intense peaks at 650.0 nm (417 cm^{-1}) and 658.7 nm (620 cm^{-1}) are the overtones of the LO phonon, namely 2LO and 3LO. These higher order peaks, especially the 3LO mode, are only visible for high laser intensities and long integration times.

Photoluminescence measurements at low temperatures revealed that the broad emission band consists of several narrow peaks with different energies and line widths < 5 meV [74]. These features were attributed to localization of the emitting excitonic states in shallow

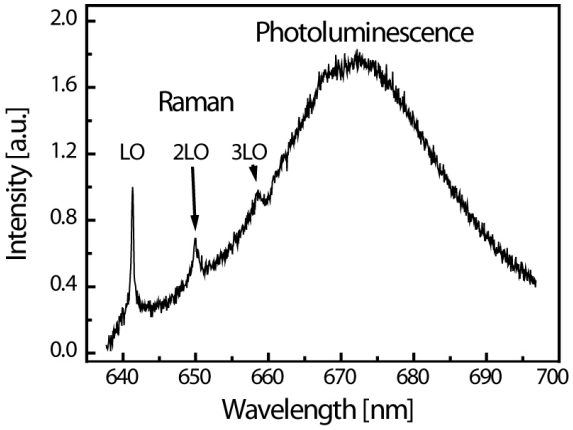

Figure 2.11: The spectrum of a single CdSe nanowire reveals photoluminescence and Raman activity. The frequency of the PL band depends on the diameter of the NW, here it is 670 nm (1.85 eV) and the FWHM is rather broad. The LO phonon mode is the strongest Raman signal, also visible are its overtones 2LO and 3LO. The excitation wavelength λ_{ex} was 632.8 nm.

potential minima along the nanowire in combination with wider variations of the underlying potential energy. The emission intensity which was found to be uniform along the whole nanowire at room temperature concentrates into bright spots at low temperatures, which is consistent with the proposed exciton localization. The reason for this behaviour are inhomogeneities inside and outside the nanowire that influence the potential energy. The energy barriers however are small which leads to a widening of the narrow peaks with increasing temperature that finally merge together at room temperature resulting in the usually observed broad emission bands.

2.2.5 Synthesis

Several strategies for the fabrication of inorganic semiconducting nanostructures have been developed during the last decades, some of them are non wet chemical approaches while others are solution based. Amongst the former are lithography techniques, vapour liquid solid growth (VLS), molecular beam epitaxy (MBE) and chemical vapour deposition (CVD). Wet chemical strategies like the solution liquid solid technique (SLS) and the supercritical-fluid liquid solid technique (SFLS), developed in the 1990s, have made significant progress and are now able to deliver high quality nanomaterials. The CdSe nanowires used in this work have been synthesized by the SLS method which will therefore be summarized in the next section.

Generally, wet chemical strategies used to start from dimethyl cadmium ($(CH_3)_2Cd$), which is an air sensitive, pyrophoric, highly toxic and expensive material. After the introduction of the much easier to handle starting materials cadmium oxide (CdO) and cadmium acetate ($Cd(CH_3CO_2)_2$), a significant growth of the field of synthesis took place,

yielding many kinds of nanostructures like spheres, rods, wires, arrow heads, and tear drops [78]. Also higher order structures like core-shell systems, heteromaterial nanorods and nanowires, or branched nanowires have been successfully synthesized [79–83]. The availability of such structures was naturally followed by a burst of research on semiconducting nanomaterials accompanied by theoretical work and modelling.

Solution liquid solid growth of CdSe nanowires

Several reviews on the synthesis of nanomaterials including the SLS method can be found in literature [16, 83, 84]. In general, the advantages of the SLS method are low temperatures, potentially higher synthesis yields, soluble materials, high crystallinity, and excellent control of shape, size and dimensionality of the nanowires. The thinnest possible diameters down to the exciton Bohr radius of CdSe and even below have been achieved by the SLS method. This is of fundamental importance for the investigation of quantum confinement effects and their possible applications.

For the synthesis reaction CdO is dissolved in tri-n-octylphosphine oxide (TOPO) by heating up the solution to 250 °C. A second solution containing the catalytic Au/Bi nanoparticels and the Se precursor TOPSe (tri-n-octylphosphine selenide) is then added. After a short reaction time the mixture is swiftly cooled down which quenches the nanostructure growth. Some toluene has to be added during cooling because otherwise TOPO would solidify. The resulting nanomaterial can be further purified using ultra-centrifugation.

The seeded growth mechanism is sketched in figure 2.12. It requires a molten metal catalyst nanoparticle, for example made of a tiny Au core with a Bi shell. The organometallic precursors dissolve in the catalyst particle until saturation. Upon supersaturation a CdSe core nucleates at the particle surface and starting from this nucleus the nanowire growths out of the catalyst by further adding Cd and Se ions. The resulting nanowire has one tapered end and is attached to the catalyst particle on the other one.

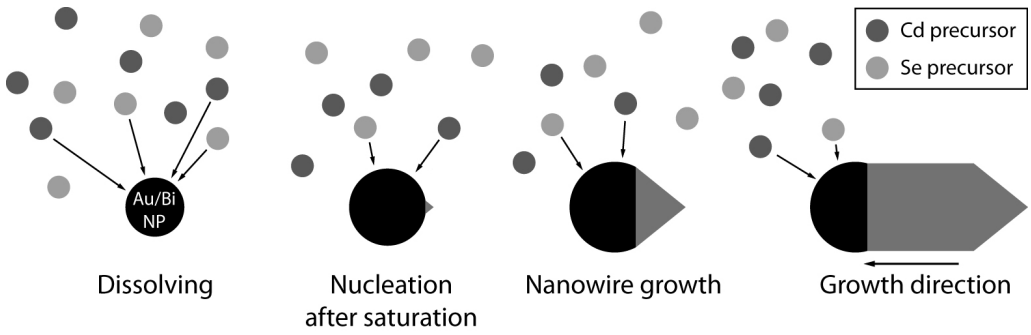

Figure 2.12: Schematic drawing of the nanowire growth mechanism in the solution liquid solid method. The molten Bi nanoparticle absorbs Cd and Se until it is saturated. The nanowire nucleation then starts at the particle surface and it grows further until the precursor concentration is too low or the reaction itself is quenched by cooling.

Several parameters influence the resulting morphology of the synthesized nanowires, allowing control and tailoring [16, 83, 85]. In principal, there are two competing processes: the first one between nucleation at the catalyst particle leading to a nanowire growth and self nucleation which results in nanocrystals. Secondly, longitudinal growth of the nanowires adding to their length competes with a transversal growth adding to the diameter.

If the concentrations of the Cd and Se precursor are too high, self nucleation leads to nanocrystals, whereas low concentrations result in thicker nanowires. Also the ratio of Cd and Se is important, in the case of stoichiometric conditions branching of the nanowires is favoured, while an asymmetric ratio with an increased amount of Cd precursor leads to straight nanowires. The temperature has empirically found to exhibit an optimum between 250-350 °C, low temperatures lead to an increased number of branching sites. Regarding the catalyst nanoparticles the concentration as well as the size has to be considered. At low concentrations self nucleation again favours the creation of nanocrystals. Next, the size influences the diameter of the resulting nanowires, bigger particles lead to thicker nanowires. The reaction time finally determines the length and/or the diameter, depending on the ratio of longitudinal and transversal growth. All these parameters have to be empirically optimized for the preparation of the desired nanowire sample material.

The preparation conditions further affect the crystal structure of the products. As mentioned before wurtzite and zinc-blende structure are stable in the nanowires. Longer reactions times and higher temperatures result in an increased WZ fraction while shorter reaction times and lower temperatures favour the formation of ZB structure. This means that ZB structure is kinetically favoured while WZ structure is the thermodynamically preferred product [85]. Since the energetic as well as the structural difference between those two is pretty small, however, CdSe nanowires synthesized by wet chemistry always feature an admixture of both crystal structures with random segment lengths.

If branching of the nanowires is desired, the number of branching sites can be further increased by trioctylphosphine (TOP) doping of the ligand medium, which proofed to have a strong effect on the nanowire growth. It has been proposed that binding of the ligand to specific crystal faces may assist the branching events. The resulting structures include v-shaped, y-shaped, tripod, tetrapod, merged-y shaped and higher order nanowires. A scheme including the different branch structures and the nomenclature according to references [16, 83] is shown in figure 2.13.

To undergo a branching event, at least two single nanowires have to be grown from the same catalyst particle. Depending on the angle θ between them, either a ZB core is build up (upper way in figure 2.13) or the wires directly merge together with a twinning boundary that runs from the core through the third arm (lower part of figure 2.13). An angle θ that is smaller than the critical angle $\theta_c \approx 77°$ leads to a merged-y structure, larger angles result in branched structures containing a ZB core. In the case of formation of a ZB core, the nanowire arms are attached to equivalent {111} faces of the tetrahedral core

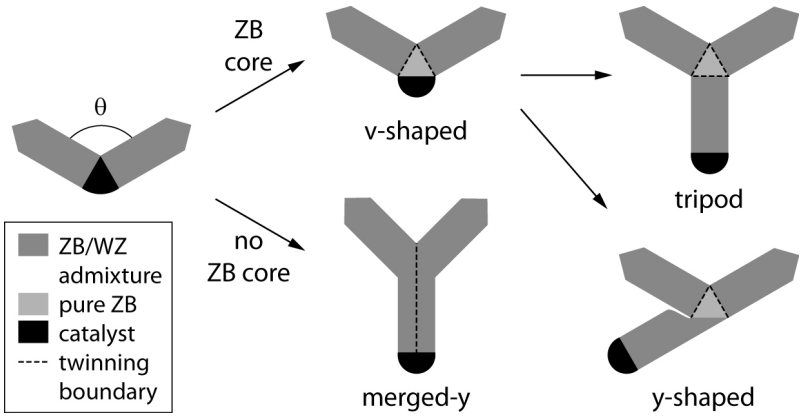

Figure 2.13: Schematic of the possible branching of nanowires including conventional nomenclature. v-shaped, tripod, tetrapod (not shown) and y-shaped nanostructures comprise a tetrahedral ZB core with the arms attached equally to the {111} faces. On the contrary, the merged-y-shaped structures have a twinning boundary running from the core through the third arm. The arms typically are composed of alternating ZB and WZ segments of random size.

by a twinning site. This leads to a non-planar structure of the tripod shape with an angle of $\sim 109.5°$ between the arms. The branching mechanism for the tetrapod is the same as for the tripod, it only starts with three nanowires growing from the nanoparticle instead of two (not shown in figure 2.13). The catalyst is then attached to a fourth arm while all arms are equally attached to the equivalent faces of the ZB core.

3 High-resolution optical microscopy

Today, optical microscopy and spectroscopy are common tools for the investigation and the characterization of a multitude of materials in chemistry, physics, biology, medicine, material sciences, and many more. It allows us to see small objects that can not be seen with the bare human eye. Spectroscopy, the investigation of the interaction of matter and light, provides further information for example on the material composition, the structure or dynamic processes.

Optical microscopy opens up the fascinating microscopic world, however, as the size of the subject of interest reaches the nanoworld it faces the well known diffraction limit. In today's nanoscience and nanotechnology the designed structures are often considerably smaller than 100 nm whereas the resolution of conventional optical microscopy is limited to about $\lambda/2$, i. e. about 250 nm for visible light. Therefore many concepts to overcome the diffraction limit have been developed during the last decades. They can be distinguished into far-field techniques working with propagating waves in the far-field, and near-field techniques that use a tiny sharp probe to locally extract information from the near-field of the sample.

This chapter provides the theoretical basics regarding optical microscopy and high resolution microscopy using optical antennas. First the diffraction limit and its origin will be outlined. Thereafter, far-field and near-field techniques to overcome this limit are shortly discussed. Within these methods, tip-enhanced near-field optical microscopy (TENOM) will be presented in more detail since it is the main object of this work to improve the understanding of the enhancement mechanisms and to establish TENOM as a method for quasi one-dimensional systems beyond carbon nanotubes, for which it has been introduced already years ago [19]. The metal tips that are used in TENOM can be described as optical antennas, a powerful concept which is introduced in section 3.3. Since optical antennas influence the angular emission of single emitters, a basic introduction to radiation patterns is given afterwards. Finally a short review of TENOM on 1D systems in literature is given.

3.1 The diffraction limit

Imaging a point source with an optical system does not result in an image point of the same size, but rather in a blurred spot whose shape is defined by the so called point

spread function (PSF). The reason for this fact is the wave nature of light, which leads to diffraction effects.

The electrical field E in a plane z emanating from the source plane with $z = 0$ can be described by an angular spectrum representation

$$E(x, y, z) = \iint_{-\infty}^{\infty} \hat{E}(k_x, k_y; 0)\, e^{i[k_x x + k_y y \pm k_z z]}\, dk_x dk_y, \tag{3.1}$$

where $\vec{k}$ is the wave vector given by

$$|k| = \frac{\omega}{c} n \tag{3.2}$$

and

$$k_z \equiv \sqrt{k^2 - k_x^2 - k_y^2}. \tag{3.3}$$

It means that the electrical field E can be described as a superposition of an infinite number of plane waves and evanescent waves emanating from the source. For a purely dielectric medium, the index of refraction is a real and positive number. Plane waves and evanescent waves can be then distinguished with respect to their propagation term, depending on whether the wavenumber k_z is real or imaginary. For real wavenumbers with $k_x^2 + k_y^2 \leq k^2$, the exponential factor $e^{\pm i|k_z|z}$ is an oscillating function which results in propagating plane waves with a constant intensity. This kind of waves and thus the information they contain can be detected by far-field techniques. For imaginary wavenumbers with $k_x^2 + k_y^2 > k^2$, the exponential factor $e^{-|k_z|z}$ is an exponentially decaying function. In this case, the waves do not propagate, because their intensity decays exponentially. Consequently, they can not be observed in the far-field. Information provided by these so called evanescent fields is only accessible at very small distances from the source, that is the near-field.

The spatial resolution

The larger the detected spectrum of wave vectors Δk, the better is the spatial resolution of an optical system. Δk is given by

$$\Delta k = \sqrt{\Delta k_x^2 + \Delta k_y^2}. \tag{3.4}$$

To distinguish two point sources with a distance Δr, the product $\Delta k \cdot \Delta r$ has to be ≥ 1 [13]. This means the larger Δk, the smaller the minimum distance Δr between two objects can be. In the far-field, only wave numbers up to $k = \frac{\omega}{c} n = \frac{2\pi}{\lambda} n$ are available, which leads to a minimum distance

$$\Delta r_{min} = \frac{\lambda}{2\pi n} \tag{3.5}$$

for two point sources to be resolvable. In an optical system, only light propagating towards the lens or the objective, which means within a specific angle θ, can be collected. This

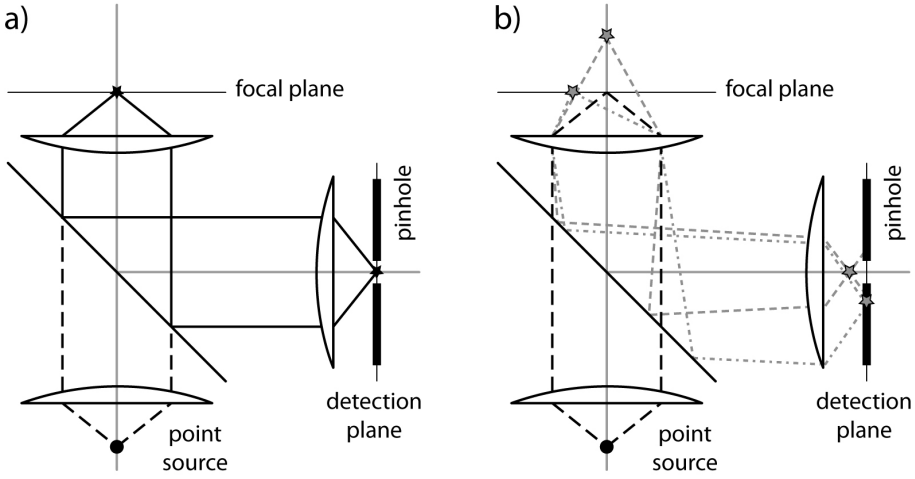

Figure 3.1: Schematic of the light paths in confocal microscopy for a) an emitter in the focus and b) two emitters that are moved out of the focus in x and z direction, respectively. Signal emanating from the emitter in a) reaches the a detector placed behind the confocal pinhole, whereas signal from the displaced emitters in b) are blocked by the pinhole.

restriction is described by the numerical aperture NA $= n\,sin\alpha$ of the optical system, which modifies equation 3.5 to

$$\Delta r_{min} = \frac{\lambda}{2\pi\,\mathrm{NA}}. \tag{3.6}$$

The axial resolution is slightly inferior to the lateral resolution, because the focus is more elongated in z direction.

The lateral resolution given by equation 3.6 is the best resolution that can be theoretically achieved with an ideal optical systems. However, for real systems based on elements like lenses and mirrors it is impossible to reach it. A technique which comes close to this limit is laser scanning confocal microscopy [86,87]. In confocal microscopy, light emanating from a point source is used to excite the sample, which is scanned through the focus of a lens, and the detected response is focused again through a small pinhole that is confocal to the focus on the sample. In doing so all light emanating from outside the focal volume is suppressed and does not reach the detection element. This principal is shown in figures 3.1 a and b for an emitter centered in the focal spot and for two emitters which are displaced in x and in z direction, respectively.

Several far-field and near-field concepts that have been developed to overcome the classical diffraction limit will be presented in the next two subsections, beginning with an overview of the far-field concepts. After introducing several near-field schemes, tip-enhanced near-field optical microscopy (TENOM) will be presented in its own section as it is the technique used throughout this work.

Far-field concepts

Today, several far-field concepts are established tools for the non-invasive investigation of nanosized objects, as for example photoactivated localization microscopy (PALM), fluorescence photoactivated localization microscopy (FPALM) and stochastic optical reconstruction microscopy (STORM) [7–9]. These methods utilize the idea of substituting the problem of spatial resolution by the problem of position accuracy. In that way they obtain nanoscale resolution although they are working in the far-field. This is possible because the position of a single emitter can be determined with nanometer accuracy even though the image spot size given by the point spread function of the optical system is much larger. However, this requires that the active emitters are separated far enough to avoid overlapping of the PSFs. Therefore, all these techniques rely on switching processes of the emitter activity to make sure that only few emitters are active at any time. As a consequence, the sample must be labelled densely with specific switchable or blinking dye molecules. The position accuracy which determines the resolution of those methods is given by the signal-to-noise-ratio of the experiment. The resolution is thus defined by parameters like the density of dye labelling of the sample, the quantum yield of the emitter (the number of emitted photons), and the detection sensitivity of the optical system, which consequently have experienced extensive improvements lately.

Another well established technique is stimulated emission depletion (STED), which actively controls the excitation state of the emitting molecules [6]. A diffraction limited spot on the sample is excited with a short laser pulse followed by a second pulse, the so called STED pulse, that induces stimulated emission. The intensity of the STED pulse is ring-shaped, therefore only dye molecules in a small central region remain in the excited state. Only emission from this tiny central area is detected afterwards. By raster scanning the sample, images with a spatial resolution below 20 nm can be achieved using STED. Commercial systems are available nowadays, offering 50 nm spatial resolution (Leica TCS STED), but they are rather expensive.

In general, these techniques working in the far-field can be also used for 3D imaging and the acquisition of movies. This is a valuable advantage to investigate thick biological samples like cell tissue and to follow dynamical processes. On the other hand, they usually require invasive labelling with dye molecules that provide strong and stable optical signals. This hinders the direct observation of the sample's intrinsic fluorescence or Raman scattering and direct spectral information from the investigated object is therefore inaccessible.

Near-field concepts

Another idea to overcome the diffraction limit was presented by Edward H. Synge in 1928 [88], who himself called it "exceedingly simple". He proposed to bring a tiny hole in an opaque metal screen in close proximity to the sample in such a way that only light

passing this hole reaches and excites the sample. The optical answer is than detected from the back side while scanning the sample pixel by pixel underneath the excitation hole. In this configuration the resolution of the system is only given by the size of the hole and its distance from the sample which should be much smaller than the wavelength of the excitation light. Many years later, after the development of piezoelectric positioners that allowed for accurate sample positioning and probe-sample distance control, his idea could be realized for the first time in the microwave regime [89]. Nowadays, metal coated glass fiber tips with a small aperture of 50-100 nm are successfully used as probes for scanning near-field optical microscopy (SNOM). The main drawback of this scheme is the very low throughput of a sub-wavelength aperture, resulting in very low excitation or detection efficiencies.

A superior concept is apertureless SNOM (a-SNOM), where a tiny probe is used to locally explore the near-field of the sample surface. In a-SNOM the probe acts as an optical antenna that converts the local near-field into propagating electromagnetic waves and vice versa. The concept of optical antennas will be introduced in section 3.3. Two types of a-SNOM can be distinguished: (i) scattering SNOM (s-SNOM) and (ii) tip-enhanced near-field optical microscopy (TENOM).

In scattering SNOM a metal tip scatters the near-field of the sample into propagating waves [11]. To discriminate the signal from the large scattering background originating from the diffraction limited excitation spot, the tip-sample distance is modulated at a frequency Ω and the detection signal is demodulated at higher harmonics of Ω to filter out the near-field signal and rejecting the constant background contribution. In this way, the Rayleigh scattering response from the tip, acting approximately as a dipole, and its image dipole inside the sample are obtained and yield nanoscale information of the dielectric properties of the sample [90].

TENOM exploits the highly confined and strongly enhanced optical fields in the vicinity of laser illuminated metallic nanostructures, as for example nanoparticles or sharp tips. These fields locally increase the spectroscopic response from the sample by enhancing the excitation and radiation rate, resulting in a substantially higher sensitivity of this method. A detailed introduction to TENOM will be given in the following section.

3.2 Tip-enhanced near-field optical microscopy (TENOM)

Today, the highest optical resolution and detection sensitivity on surfaces is achieved with tip-enhanced near-field optical microscopy (TENOM) [12, 91]. In TENOM a sharp laser-illuminated metal tip is used as near-field probe to locally enhance the signal from the investigated sample material. Plasmon resonances and the so called lightning rod effect are responsible for highly confined electrical fields at the tip apex which are able to substantially increase the excitation and the radiative rate [13, 92]. Owing to the near-field

nature of those enhanced fields, their intensity decays exponentially with the distance from the tip and the sample material must be in close vicinity of the near-field probe. This requires a highly sensitive probe-sample distance control usually done by a shear-force feedback mechanism.

A representative TENOM data set comparing confocal and tip-enhanced images of carbon nanotube photoluminescence is presented in figure 3.2 a and b, respectively. Confocal and TENOM PL images of an identical sample area were recorded with the same excitation power and integration time. Only the scan speed was reduced for the acquisition of the near-field image to avoid damaging of the tip. The topographic image obtained simultaneously with the TENOM PL image is shown in (c). The comparison of the confocal and the near-field PL images clearly shows the tip-induced signal enhancement which is connected to a drastically improved spatial resolution.

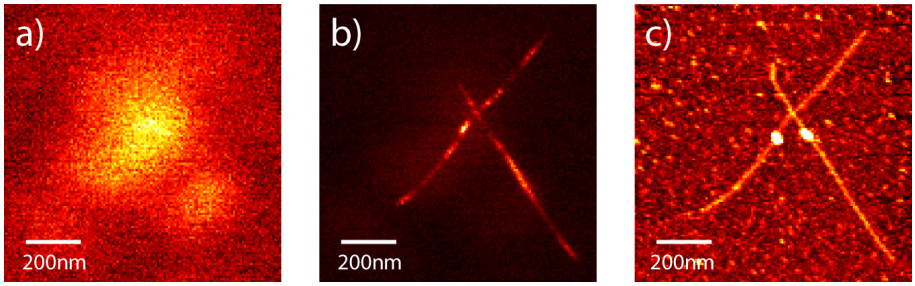

Figure 3.2: a) Confocal image of a photoluminescent carbon nanotube sample with diffraction limited spatial resolution. b) PL image of the same sample area measured with TENOM. Excitation power and integration time have been the same for both measurements. The sharp gold tip leads to an enhanced detection sensitivity and a resolution of about 15 nm. The TENOM image resolves the arrangement of the nanotubes and intensity variations along them. c) The simultaneously obtained topographic image. Material: SC-wrapped CoMoCat nanotubes.

Enhanced optical fields at the tip apex

If an incident optical field of appropriate frequency oscillates along the tip axis collective electron oscillations are induced in the metal. These charge oscillations, known as plasmons, result in a surface charge density that reaches its highest amplitude at the tip apex. Since the specific geometry of the metal tip constitutes a spatial singularity at the apex the surface charge is concentrated which leads to stronger local fields. This effect is called the lightning rod effect. The frequency at which plasmons are most efficiently excited, the plasmon resonance, depends on the tip material and its specific shape.

The magnitude of electrical field enhancement is given by the field enhancement factor

$$f = \frac{E^*}{E_0} \tag{3.7}$$

which is defined as the ratio of the field at the tip apex E^* and the incident field E_0. It is a measure of the enhancement capabilities of the near-field probe, because the electrical fields are responsible for the desired signal enhancement. The quality of the resulting near-field experiment, however, is not only determined by the electric field enhancement factor f, because the probe will also change the properties of the emitter itself. In the case of photoluminescence, the quantum yield of the emitter plays a crucial role because a low QY may increase while a QY of one cannot be enhanced further. In addition, if the emitting object is spatially extended, charge carrier mobilities may effect the signal enhancement since mobile excited states are able to enter or leave the near-field interaction range of the probe. Therefore, when giving a number of enhancement, the entire system of probe and sample has to be considered [45].

A more practicable value is the image contrast, which is defined as the contrast between enhanced signal and background signal. The background signal arises from the sample material within the diffraction limited excitation spot, and is always present in TENOM measurements. The size of the diffraction limited focus is determined by the properties of the imaging system and the wavelength of light used in the experiment. The magnitude of the background contribution within the detected signal crucially depends on the dimensionality of the sample material, which defines the examined volumes of the sample material. To account for the different sizes of the far-field and the near-field focus, the constant factor V is defined as

$$V = \frac{V_{ff}}{V_{nf}}, \tag{3.8}$$

with the size of the sample in the near-field focus V_{nf} and in the far-field focus V_{ff}. In the case of a quantum dot smaller than the near-field focus, the whole dot would be within both foci and thus $V_{nf} = V_{ff}$. For a two-dimensional object the near-field signal from the small area of near-field interaction has to compete with the background signal from the much larger diffraction limited focus and $V_{nf} \ll V_{ff}$. For the quasi-1D structures investigated in this work, the ratio of the widths of diffraction limited focus and near-field focus are relevant. A typical number for a confocal microscope with a resolution of 250 nm combined with an optical antenna providing 15 nm resolution would be $V = 250\,nm/15\,nm \approx 17$ when investigating 1D structures, which is still a relatively small number. For comparison, a 2D sample would result in $V = (125\,nm)^2/(7.5\,nm)^2 \approx 278$ by relating the examined areas, in other words the signal enhancement must be much stronger to overcome the far-field background.

The electrical field in the vicinity of a metal tip can be approximately described by the field of an effective dipole $\mu(\omega)$, which is located at the center of the tip apex [13]. Its magnitude is given by

$$\mu(\omega) = \begin{bmatrix} \alpha_\perp & 0 & 0 \\ 0 & \alpha_\perp & 0 \\ 0 & 0 & \alpha_\parallel \end{bmatrix} E_0(\omega), \tag{3.9}$$

with the incident field $E_0(\omega)$ and the polarizations $\alpha_\perp$ and $\alpha_\parallel$ perpendicular and parallel to the tip axis, respectively. The polarizabilities are given by

$$\alpha_\perp(\omega) = 4\pi\epsilon_0 r_{tip}^3 \frac{\epsilon(\omega)-1}{\epsilon(\omega)+2} \tag{3.10}$$

and

$$\alpha_\parallel(\omega) = 2\pi\epsilon_0 r_{tip}^3 f_e(\omega), \tag{3.11}$$

with the bulk dielectric constant ϵ of the metal tip with a tip radius r_{tip}, and the complex field enhancement factor f_e. Generally, the polarizability of the tip is assumed to be much stronger along its axis, which means that $\alpha_\parallel \gg \alpha_\perp$ and thus $f_e \gg (\epsilon(\omega)-1)(\epsilon(\omega)+2)$, which is an appropriate approximation for the elongated structure of the tip [93].

As a consequence, charges can be only accumulated at the tip apex if the driving field is polarized parallel to the tip axis, while a transverse polarization would not lead to enhanced electrical fields. Therefore, a radially polarized doughnut mode is commonly used to efficiently excite the tip, resulting in strong longitudinal fields in the central focus which give rise to highly confined electrical fields at the tip apex [22,94]. According to the reciprocal theorem, radiation emanating from the tip leads to radial polarization in the detection plane.

Finally, the resulting electric field at the tip apex can be written as

$$E(r,\omega) = E_0(r,\omega) + \frac{1}{\epsilon_0}\frac{\omega^2}{c^2}\overleftrightarrow{\mathrm{G}}(r,r_0,\omega)\mu(\omega), \tag{3.12}$$

with the origin r_0 of the effective tip dipole μ and the dyadic Green's function $\overleftrightarrow{\mathrm{G}}$.

To which extend the optical signal from the sample will be increased by this enhanced field differs for photoluminescence and Raman scattering.

Enhancement of Raman scattering

The intensity of the Raman scattering signal depends on both the excitation rate as well as emission rate, denoted as $k_{ex}(\lambda_{ex})$ and $k_{rad}(\lambda_{rad})$, which depend on the wavelength λ of the exciting and the radiated fields. The signal enhancement M_R can be written as

$$M_R = \frac{I_R^*}{I_R^0} = \frac{k_{ex}^*(\lambda_{ex})}{k_{ex}^0(\lambda_{ex})}\frac{k_{rad}^*(\lambda_{rad})}{k_{rad}^0(\lambda_{rad})}, \tag{3.13}$$

with the Raman signal I_R^0 in the absence of the tip and the tip-enhanced Raman signal I_R^*. Since the Raman shifts are typically moderate and $\lambda_{ex} \sim \lambda_{rad}$, the enhancement factor of the tip is similar for both processes. Therefore M_R given by equation 3.13 can be approximately written as

$$M_R \approx \frac{k_{ex}^*}{k_{ex}^0}\frac{k_{rad}^*}{k_{rad}^0} \approx f^4. \tag{3.14}$$

The signal enhancement by the tip scales with the forth power of the field enhancement [95]. This means that even moderate field enhancement results in a substantially enhanced signal intensity. For Raman scattering with typically very small scattering cross sections, this is a key to achieve single molecule detection sensitivity [96].

It has to be mentioned that also the collection efficiency impacts to the image contrast. As will be shown in this work the radiation rate enhancement is connected to a spatial redistribution of the emission. The fraction of the power radiated into the angle of view of the collecting element can thus be altered by the near-field probe thereby altering the ratio of detected near-field and background signal. Consequently, the measured ratio of the Raman scattering intensities $\frac{I_R^*}{I_R^0}$ does not exactly reflect the electric field enhancement.

Enhancement of photoluminescence

In the case of photoluminescence, the signal intensity also depends on the excitation rate, but the emission process is more complex than for Raman scattering. After excitation, the energy can be emitted radiatively giving rise to a photon or the excited state relaxes via non-radiative channels. The ratio of emitted photons and excited states is given by the quantum yield (QY) of the emitter. The signal enhancement for photoluminescence is thus given by

$$M_{PL} = \frac{k_{ex}^*}{k_{ex}^0}\frac{Q^*}{Q^0} \approx f^2\frac{Q^*}{Q^0} \tag{3.15}$$

with the intrinsic quantum yield Q^0 and the quantum yield modified by the tip Q^*.

For high quantum yield systems with Q^0 alread near unity, such as dye molecules or some well-designed quantum dots, Q^0 can not be increased further and consequently, the maximum signal enhancement scales with only f^2. Furthermore a metallic near-field probe may introduce additional non-radiative decay channels at very short sample-tip distances which reduces the quantum yield. Energy is hereby transferred to the tip and can dissipate non-radiatively within the metal, a process known as quenching [97]. The distance dependence of the enhanced signal will be addressed in the next section.

On the other hand, the QY can be increased drastically for low quantum yield systems such as carbon nanotubes or CdSe nanowires, resulting in much higher signal enhancement factors. Again quenching may play a role at short distances and has to be avoided carefully.

Another aspect that has some influence on near-field measurements in 1D systems is exciton mobility. In systems where the excitons are mobile they might leave the area of signal enhancement after excitation, and the probability of radiative decay can not be increased by the tip. This has to be taken into account for the estimation of the enhancement factors for excitation and radiative rate as will be shown in chapter 5.4.

Distance dependence of the near-field signal

A distinct characteristic of the near-field interaction between probe and sample is its short ranged nature. The signal enhancement induced by the probe is not operative until the tip approached the sample to a distance of only few nanometers, leading to a drastic increase of the signal. In the case of enhanced Raman scattering the signal is expected to rise continuously with the field enhancement factor to the fourth (f^4) [22]. For photoluminescence signals, tip-induced quenching at shortest distances competes with the signal enhancement effect, therefore a final decrease of the signal intensity is expected [97–100].

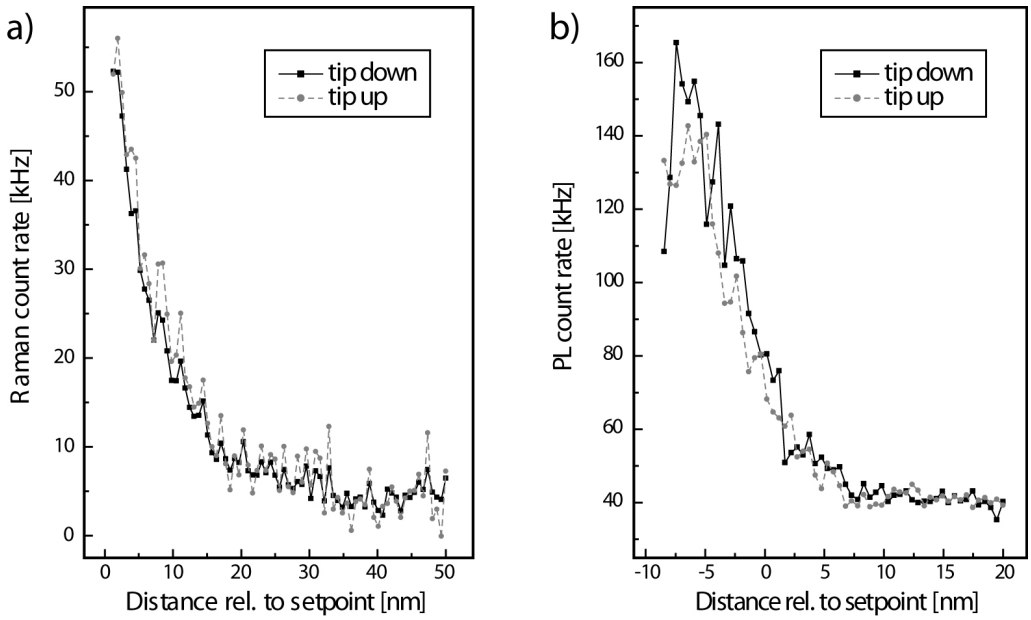

Figure 3.3: Tip-sample distance dependence of the signal enhancement in near-field measurements. a) Approach curve for Raman scattering of a single SWCNT showing a steep signal increase. c) Approach curve for photoluminescence of a SWCNT revealing quenching at very short distances.

In figure 3.3 a and b Raman and PL approach curves measured with a sharp gold tip on single-walled carbon nanotubes are shown. The absolute distance could be measured by decreasing it to zero, where the tip would touch the sample surface. Since this would damage the tip apex, the measurement is stopped before. The signal intensity is thus plotted against the tip position relative to the setpoint position, which corresponds to the tip-sample distance used in TENOM imaging. While the steep increase within few nanometers continues for Raman scattering, the competition of signal enhancement and quenching leads to a drop-off in the PL intensity after passing a maximum enhancement.

Owing to this strong distance dependence of the signal in a TENOM experiment it is crucial to keep the near-field probe in a constant distance of few nanometers above the sample surface. While the investigation of Raman signals allows for very small distances,

quenching has to be avoided in PL measurements and the distance has to be well considered to provide the maximum enhancement. Even small variations in the distance lead to strong changes in the signal intensity because of the steep signal increase. Therefore accurate tip-sample distance control with appropriate feed-back parameters is essential.

3.3 Optical antennas

The antenna concept is well established in the radio frequency and the microwave regime, where the antenna is defined by its functionality: it converts freely propagating electromagnetic radiation into localized energy and vice versa. It is thus a mediator between a local transmitter or receiver and propagating waves that are able to travel large distances. A schematic of the antenna principle is depicted in figure 3.4.

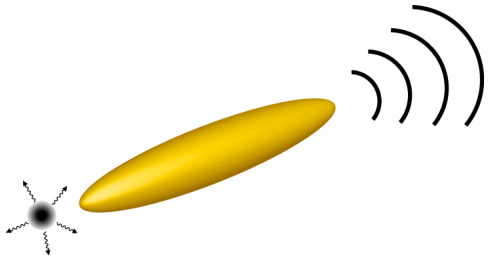

Figure 3.4: An antenna as defined by its functionality: it couples freely propagating waves into localized energy and vice versa. (Adapted from [101].)

The dimensions of radio antennas, especially the length L, scale with the wavelength λ of the freely propagating waves. As a consequence, antennas working at optical frequencies will be of nanoscale size. Hence, the fabrication of such antenna structures requires nanotechnology which only became feasible during the last decades and is now available for researchers and engineers in terms of bottom-up as well as top-down schemes. The development of the required nanotechnology gave rise to a rapidly growing field of optical antennas.

J. Wessel was the first who suggested the use of optical antennas for near-field microscopy, pointing out the analogy to their radio- and microwave counterparts by introducing the terminology [102]. U. C. Fischer and D. W. Pohl finally implemented near-field optical microscopy using the enhanced electromagnetic fields at a gold coated polystyrene bead [103].

While there are lots of similarities between radiowave and optical antennas they also exhibit significant differences. The most important one is the failure of the scalability with λ. At optical frequencies metals can no longer be regarded as perfect conductors because the penetration depth of fields into the metal (skin depth) is in the range of the dimension of the optical antennas. Collective oscillations of the electron gas are excited which can be described by a strongly coupled plasma assuming that $d \ll \lambda$ and that the electron gas

behaves according to the Drude model [104]. It is therefore necessary to introduce the effective wavelength λ_{eff} given by

$$\lambda_{eff} = c_1 + c_2 \frac{\lambda}{\lambda_p}, \tag{3.16}$$

which is effectively shorter than the wavelength λ of the propagating fields [105]. c_1 and c_2 are geometrical factors depending on the optical antenna properties and λ_P is the plasmon wavelength.

In the following, the properties of optical antennas are defined in analogy to their radiowave counterparts as described by Novotny et al. [105]. The transmission efficiency ϵ_{rad} describes how much power P_{rad} of the total power dissipated to the antenna P is radiated. It is given by

$$\epsilon_{rad} = \frac{P_{rad}}{P} = \frac{P_{rad}}{P_{rad} + P_{loss}}. \tag{3.17}$$

Energy that is transferred to the antenna but dissipated non-radiatively is summarized in P_{loss}. The directivity D which describes the angular distribution of radiation in space is given by

$$D(\theta, \phi) = \frac{4\pi}{P_{rad}} p(\theta, \phi), \tag{3.18}$$

with the angular power density $p(\theta, \phi)$ and θ, ϕ defining the direction of propagation. Finally the gain G is defined as

$$G = \frac{4\pi}{P} p(\theta, \phi) = \epsilon_{rad} D. \tag{3.19}$$

Due to the reciprocity theorem the characteristics of a receiving antenna are equal to its transmitter characteristics and vice versa.

Optical antennas allow for visualization, control and manipulation of optical fields at nanometer length scales. This makes them highly interesting tools for many applications, because they increase the performance of optoelectronic devices, from light emitting diodes over sensors and photovoltaics to microscopic techniques that work beyond the diffraction limit, which includes also tip-enhanced near-field optical microscopy. The radiation characteristics of an optical antenna in form of a sharp gold tip, as used in TENOM, will be discussed in the following section. Utilizing optical antennas in TENOM constitutes an intervention of the antenna (the near-field probe) on the light-matter interaction. The optical antenna influences the sample properties, for example by altering the transition rates, the angular emission, the spectrum, or the quantum yield [106–111]. The sample and the near-field probe thus form a coupled system. Enhancement and redirection of the emission of single-walled carbon nanotubes by an optical antenna will be content of chapter 5, the influence of an antenna on the spectral and angular emission of CdSe nanowires is addressed in chapter 7.

3.4 Angular emission: The radiation pattern

The emission of a radiating dipole into its surrounding medium is not uniform but rather exhibits a characteristic angular intensity distribution, the so called radiation pattern. It contains information about the radiating dipole, for example about its orientation and the directivity. The specific radiation pattern gets modified if there are variations in the refractive index of the surrounding medium, for example when the radiating dipole lies on a substrate or when a (small) metal object is brought close by as it is the case in tip-enhanced near-field optical microscopy.

In the following, a short overview of the radiation patterns of dipoles in free space and on a dielectric substrate will be given. The radiation pattern can be imaged with a microscope objective by recording the 2D image of the intensity distribution in the back focal plane. The theory developed by Lieb et al. [112] to describe and simulate the recorded 2D radiation patterns of an emitting dipole close to a glass/air interface will be introduced and finally a short overview of the literature regarding the influence of optical antennas on the radiation pattern of a dipole emitter will be given.

Radiation pattern from a dipole at an interface

The radiation pattern of a point dipole in free space with refractive index n_1 can be described by the radiation of a Hertzian dipole. The radiation pattern is rotationally symmetric with respect to the axis of the transition dipole moment with the highest intensity perpendicular to the dipole axis.

The radiation pattern changes significantly if a substrate with a refractive index $n_2 \neq n_1$ is approached. The major part of the radiation is directed into the optically denser medium, which leads to a redistribution of the emission and alters the directivity. This has a direct consequence for microscopy of samples placed on a surface, e.g. a conventional glass cover slide. The collection efficiency of an index matching immersion objective approached from the glass side will always be higher than that of an air objective with the same collection angle collecting from the lower index side. In addition, surface modes which are bound to the interface can be excited at the substrate/air interface. A schematic of the total power emanating from an emitter at an interface is depicted in figure 3.5.

The total energy dissipated from the emitter placed at an interface is given by

$$P = P_u + P_{l1} + P_{l2} + P_s + P_i, \tag{3.20}$$

with the radiation into the upper halfspace P_u, radiation at the interface P_s (surface modes) and radiation into the lower halfspace P_{l1} and P_{l2}. Radiation with an angle θ larger than the critical angle θ_c, denoted as P_{l2}, originates from the near-field of the dipole whose evanescent fields are transformed into propagating waves at the interface. P_i is the

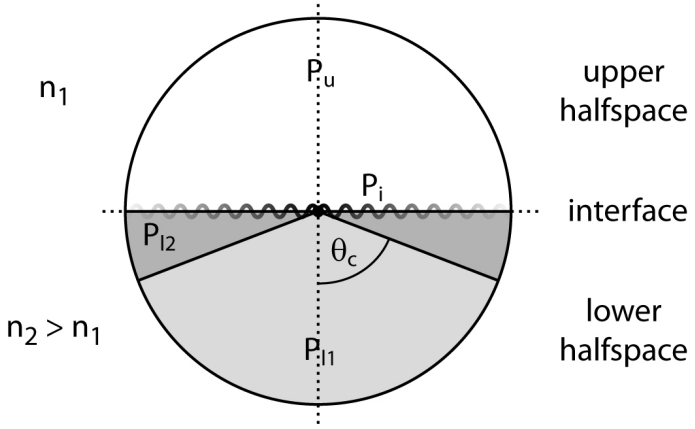

Figure 3.5: Radiation emanating from an emitter at an interface can propagate into the upper halfspace coloured in white, the lower halfspace coloured in grey scales or remain bound to the interface (surface modes, coloured black). In the lower halfspace radiation denoted as P_{l2} with an angle θ larger than the critical angle θ_c originates from the near-field of the emitting dipole.

energy that is dissipated intrinsically and non-radiatively. The contributions are depicted in figure 3.5, except for the non-radiated power P_i.

When radiation patterns are recorded with a microscope objective its numerical aperture has to be taken into account. Obviously, the higher the detection angle is, the more signal will be collected. For objectives with high numerical apertures up to 1.49 the system is assumed to be aplanatic. According to reference [112] the intensity distribution in the back focal plane of the objective is then given by

$$I(r, \varphi, \theta, \Phi) \propto \frac{1}{cos\theta}(E_p E_p^* + E_s E_s^*), \tag{3.21}$$

where r denotes the radial distance from the optical axis, φ the azimuthal angle in the back aperture, and θ and Φ the polar and the azimuthal angle of the dipole axis. A schematic including all denominations is shown in figure 3.6 a. The electrical fields E_p and E_s parallel and perpendicular to the optical axis are given by

$$E_p = c_1(\theta)\, cos\Theta\, sin\theta + c_2(\theta)\, sin\Theta\, cos\theta\, cos(\varphi - \Phi) \tag{3.22}$$

and

$$E_s = c_3(\theta)\, sin\Theta\, sin(\varphi - \Phi). \tag{3.23}$$

The coefficients c_1, c_2 and c_3 result from the presence of the interface and are defined as

$$\begin{aligned} c_1(\theta) &= \frac{n_2^2}{n_1^2}\frac{cos\theta}{cos\theta_s} t^p(\theta_s)\Pi(\theta_s) \\ c_2(\theta) &= \frac{n_2}{n_1} t^p(\theta_s)\Pi(\theta_s) \\ c_3(\theta) &= -\frac{n_2}{n_1}\frac{cos\theta}{cos\theta_s} t^s(\theta_s)\Pi(\theta_s) \end{aligned}$$

with the Fresnel transmission coefficients t^p and t^s for p- and s-polarized light, respectively. For a dipole in free space c_1, c_2 and c_3 equal unity. $\Pi(\theta_s)$ given by $\Pi(\theta_s) = e^{ikn_1 cos\theta_s \delta}$ encounters for the distance δ of the radiating dipole from the interface, k is the vacuum wavevector. For dipoles lying flat on the substrate $\delta = 0$ and $\Pi(\theta_s) = 1$.

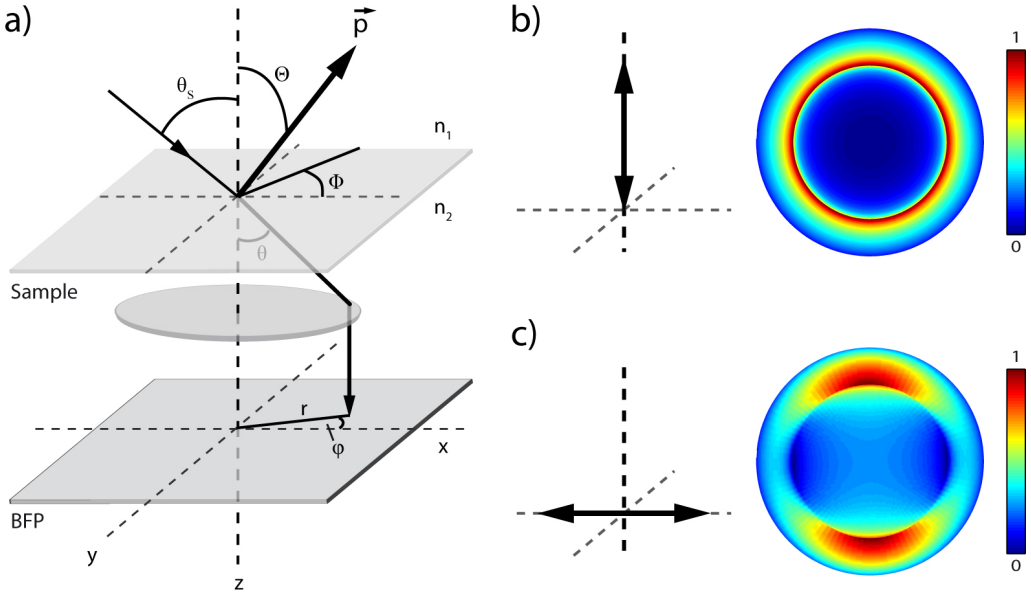

Figure 3.6: Calculation of the radiation pattern of a dipole $\vec{p}$. a) Radiation emitted at θ_s will be imaged in the BFP of the objective at position (r, φ). The normalized calculated radiation pattern in the BFP for a vertical ($\vec{p} \parallel x$) and a horizontal ($\vec{p} \perp x, y$) dipole are depicted in (b) and (c), respectively. They reveal significant differences of the intensity distribution. The pattern in (b) is radially symmetric with a sharp ring close to the critical angle and approximately no intensity in the center, the pattern in (c) is axially symmetric with two lobes and also weak intensity in the center.

The radiation patterns in the back focal plane (BFP) of the objective are calculated using equation 3.21 for a vertical dipole oriented perpendicular to the substrate and a horizontal dipole lying flat on the substrate. The results are shown in figure 3.6 b and c for the vertical and the horizontal dipole, respectively. The intensity distribution in the case of the horizontal dipole is axially symmetric with two lobes of maximum intensity in the outer rim and a weak signal contribution in the central region. The pattern from the vertical dipole on the other hand is rotationally symmetric with a sharp ring of maximum intensity in the outer rim and no intensity in the central region. Both patterns exhibit most intensity in the outer rim indicating that a high NA objective is crucial for high collection efficiencies.

The radiation pattern of an optical antenna in form of a sharp gold tip is expected to be ring shaped under the condition that the polarizability perpendicular to its axis is negligible against the polarizability parallel to it, that is $\alpha_\parallel \gg \alpha_\perp$. The radiating tip can then be treated as a vertical dipole positioned on the long axis of the tip which usually coincides with the optical axis of the microscope. As mentioned above the radiating properties

of the antenna also reflect the optimum excitation conditions because of the reciprocity principle. Consequently, the optical antenna in TENOM will be excited most efficiently if the polarization of the exciting laser matches the polarization of the emission of the antenna, that is radially polarized in the back focal plane.

As a consequence the fraction γ of the total power which is radiated into the angular detection range of an optical microscope depends on the particular dipole orientation. Whether the collected fraction is higher for a vertical or a horizontal dipole depends on the numerical aperture of the objective. This has to be taken into account when intensities of signals emanating from dipoles with different orientations are regarded and compared. In figure 3.7, γ is plotted versus the maximum collection angle of the microscope objective θ_{max} for a dipole $\gamma_{\parallel}$ oriented horizontally with respect to the sample surface (solid line) and a vertically oriented dipole $\gamma_{\perp}$ (dashed line).

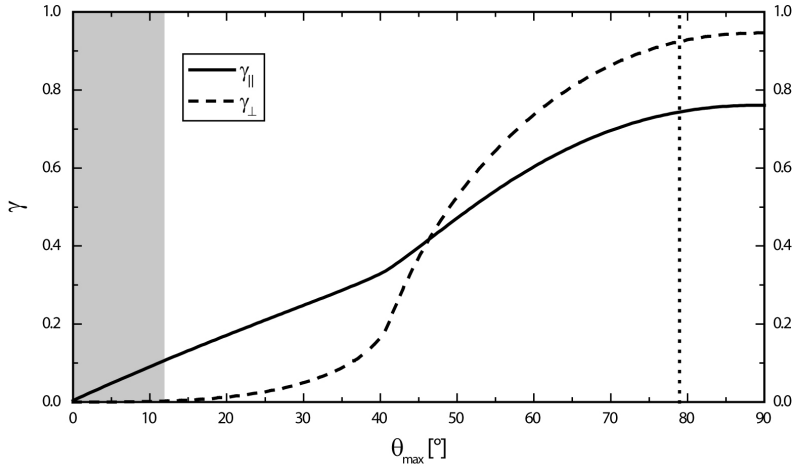

Figure 3.7: Detected fraction γ of the total power radiated by a dipole oriented parallel (solid line) or perpendicular (dashed line) with respect to the substrate, depending on the collection angle of the microscope objective θ_{max} for the setup configuration used in this work (chapter 4). The dotted line marks the maximum collection angle $\theta_{max} = 78.98°$ for the microscope objective with NA = 1.49. The grey area corresponds to the θ_{max} range for the inner part of the radiation patterns. In this range the contribution of the vertical dipole is negligible.

The solid and the dashed line show a crossing point at around 46.3°. For objectives with a maximum angle θ_{max} smaller (larger) than 46.3°, $\gamma_{\parallel} > \gamma_{\perp}$ ($\gamma_{\parallel} < \gamma_{\perp}$), which means that a larger (smaller) fraction of the radiation from a horizontally (vertically) oriented dipole is collected. For an objective with NA = 1.49, $\theta_{max} = 78.98°$ and the resulting fractions are $\theta_{\parallel} = 0.73$ and $\theta_{\perp} = 0.92$, i.e. the detection sensitivity for the vertical dipole is higher than for the horizontal dipole. For very small angles $\gamma_{\perp}$ is approximately zero as can be seen in the grey area on the left side in figure 3.7. This means that the radiation pattern of vertically oriented dipole shows nearly no intensity in the central part of the 2D pattern. This finding will be important in chapters 5 and 7.3 where the photoluminescence signal of semiconducting nanoctructures and the influence of a near-field probe (optical antenna)

on the corresponding radiation pattern are investigated. In the case of the antenna this quantity corresponds to the angular integral of the antenna directivity divided by 4π [110].

Radiation pattern from a dipole close to an optical antenna

In chapter 3.3, the concept of optical antennas was introduced as a description of the near-field probe. This section addresses the interaction between an emitting dipole and an optical antenna formed by a small nanoparticle. Different theoretical approaches have been applied to describe and predict the influence of an optical antenna, and scanning probe techniques such as SNOM and TENOM have been used in several studies to experimentally complement these theoretical results [108–110, 113, 114].

A metal nanoparticle, that is brought close to a dipole emitter significantly modifies its emission characteristic regarding the transition rates, the radiation pattern and the emission spectrum. All of them can be strongly influenced by the antenna characteristics of the metal particle. The radiation properties were found to depend on the dipole orientation with respect to the antenna, the distance between them, and the particular antenna properties defined by its structure, shape, material and size. Since the antenna characteristics in turn depend on the wavelength of the radiation, the interaction between antenna and emitter is wavelength-dependent.

In 1982, Ruppin et al. described the influence of a small metal sphere on the decay rate of an excited molecule by means of electromagnetic theory [113]. Here, energy is dissipated from the dipole-sphere system either in form of radiative loss or non-radiatively into the sphere (Ohmic losses). They found a decreasing lifetime for distances smaller than the wavelength due to quenching by the sphere. The decrease comes up to its maximum when the wavelength of emission meets the plasmon resonance of the metal particle.

Changes in the radiation pattern have been calculated and observed by Taminiau et al. [109, 110]. They used a full-3D finite integration technique and obtained the transition rates and field amplitudes relative to a reference situation in form of an emitter in vacuum. The radiation pattern was found to depend on the orientation and distance of the dipole transition moment and the antenna mode, the interaction was found to be connected to a process of angular redirection. For maximum coupling, the radiation is dominated by the antenna mode pattern regardless of the orientation of the emitter. Interestingly, even in the case of perpendicular orientation of the molecular dipole moment relative to the antenna mode, a strong coupling is observed while scanning the antenna across the dipole, as long as they are slightly separated horizontally. Only if the dipole is right underneath the antenna apex no coupling is observed. This is especially important in TENOM, where a strong near-field interaction is crucial for signal enhancement, which is thus maximized for a parallel orientation of tip and emitter dipole.

The wavelength dependence of the signal enhancement leads to modifications in the emission spectrum. Kühn et al. found that a maximum enhancement occurs at a wavelength slightly red-shifted from the particles resonance [108]. The intensity distribution in an antenna enhanced spectrum therefore does not necessarily reflect the spectrum of the unperturbed emitter. This aspect requires attention in the interpretation of spectral data obtained using enhancement by optical antennas.

The optical antenna acts as mediator between local fields and the far-field. As long as the coupling from a local emitter to the antenna is stronger than the direct coupling from the emitter to the far-field, the radiation characteristics of the antenna modes will dominate the radiation of the coupled system.

3.5 Nanoscopy on quasi 1D semiconducting nanomaterials

Carbon nanotubes have been extensively studied with tip-enhanced optical microscopy, which has resulted in many interesting publications [12, 19–24]. For inorganic nanowires, however, TENOM is not yet an established tool for nanoscale optical imaging despite the fact that nanoscale resolution would be highly desirable for the investigation of nanoscale devices and quantum confinement effects. To conclude the chapter a small overview of the literature regarding TENOM on carbon nanotubes and high-resolution optical investigations on inorganic nanowires is given in this last section.

3.5.1 TENOM on carbon nanotubes

Tip-enhanced optical microscopy has been applied to single and bundled single-walled carbon nanotubes by several groups [12,115–117]. The strong signal enhancement and the corresponding high resolution made it possible to characterize the sample material with nanoscale resolution. This facilitated imaging of the energy landscape along a nanotube by investigating PL energy shifts and intensity variations on the nanoscale, which could also be used to determine the exciton diffusion length, yielding a value of around 100 nm [45, 118]. Furthermore, the energy transfer between two semiconducting nanotubes has been investigated with respect to the distance between the nanotubes [20,21,24]. Tip-enhanced photoluminescence spectra showed no shifts in the PL energy induced by the tip, therefore spectral variations could be attributed to the investigated nanotubes themselves [50]. Also structural properties have been studied by imaging the Raman scattering [19, 22]. It was found that the scattering process connected to defects is limited to about 2 nm around the defect site [23]. Further, chirality changes in single nanotubes have been imaged by mapping two resonant RBM phonon frequencies [119].

Regarding the Raman scattering, a model has been developed for the near-field enhancement on one-dimensional semiconductors, which has been successfully applied to SW-

CNTs [93]. It predicts that the signal enhancement induced by the presence of the sharp gold tip is inversely proportional to the 10th power of the distance d between tip and sample according to

$$\frac{R(d)}{R_{max}} = \frac{1}{M} + \frac{C}{(d + r_{tip})^{10}}. \tag{3.24}$$

Here, $R(d)/R_{max}$ denotes the distance dependence of the Raman signal normalized to its maximum, M the signal enhancement factor, C is a constant and r_{tip} the tip radius. Even though the model was originally developed to describe coherent Raman scattering in SWCNTs, it is also applicable to CdSe nanowires as will be presented in chapter 7.

3.5.2 Inorganic nanowires

Up to now only few TENOM experiments on inorganic 1D nanostructures have been reported in literature. Aperture-type scanning near-field optical microscopy in combination with time-resolved measurements has been used to image emission properties of single colloidal CdSe nanowires with a spatial resolution of about 100 nm [30], which results from the size of the aperture probe. The emission properties were found to be highly sensitive to the surrounding of the nanowires, in that case to residuals from the organic suspension, and the mechanical influence of the probe. Yoskovitz et al. localized the emission of excitons in single heterostructured nanorods using apertureless near-field distance-dependent PL lifetime imaging with a spatial resolution of about 20 nm [31]. The exciton emission was always found to emanate from a well-defined region, which is consistent with the seed location in the heterostructure. Tip-enhanced Raman spectroscopy was used by Berweger et al. to image ferroelectric domains in $BaTiO_3$ nanocrystals with nanoscale resolution [33].

Further, cathodoluminescence spectral imaging of GaN/AlN quantum disks in single nanowires has been used at low temperatures to observe the quantum confined Stark effect and the influence of strain on the emission properties [32].

4 Experimental details

This chapter provides an overview of the investigated sample materials and the experimental setup. In the first part the specifications of the used carbon nanotubes and the CdSe nanowires are reported. The next section provides information on the optical system regarding excitation and detection beam path. It also contains details on the near-field configuration used in TENOM measurements. Finally, the production process for the gold probes is described.

4.1 Single-walled carbon nanotubes: sample preparation

The synthesis of single-walled carbon nanotubes (SWCNTs) results in a mixture of nanotubes with different diameters and chiralities [120]. Subsequent chirality enrichment may narrow the diameter distribution, but there are always several chiralities present in one sample. Several surfactants are available to individualize the nanotubes, which otherwise tend to form bundles due to van der Waals forces. Two kinds of carbon nanotube material have been used for this work, namely SWCNTs wrapped with soap molecules as surfactant, i.e. either sodium cholate (SC) or sodium dodecyl sulfate (SDS), and SWCNTs wrapped with poly(9,9-dioctyluorenyl-2,7-diyl), in the following referred to as polymer-wrapped carbon nanotubes. If not described otherwise, samples of SWCNTs were prepared by spin coating the aqueous suspension onto a glass cover slide that has been previously cleaned with water and methanol. Afterwards, the sample was rinsed with water to remove excess surfactant, since this would hinder the shear-force AFM microscopy due to undefined tip-sample interactions. The glass slides (Marienfeld GmbH) are transparent, 130 - 160 µm thick and have a refractive index of 1.52.

Surfactant-wrapped SWCNTs

Two nanotube materials have been wrapped with sodium cholate (SC). The first one was prepared according to the cobalt-molybdenium catalyst (CoMoCat) method resulting in nanotubes with a small diameter distribution [121, 122]. The nanotubes used here have an average diameter around 0.85 nm. A further chirality enrichment of the material was obtained by sorting by diameter using discriminating surfactants and density gradient ultracentrifugation [123–125]. The sample material was dispersed in aqueous solution using

SC (1wt%) as surfactant. It contains mainly (6,5) SWCNTs which have the photoluminescence band at around 980 nm. Also (6,4), (8,3), (9,1) and other chiralities are found in this material, emitting between 850 - 1000 nm. CoMoCat nanotubes were provided by the group of Prof. Mark Hersam (Northwestern University, Illinois, USA).

The second nanotube material was provided by Unidym, USA, synthesized according to the high pressure carbon monoxide (HiPCO) method [126, 127]. The sample material was dispersed in aqueous solution using SC (1wt%) as surfactant. HiPCO nanotubes have also been wrapped with sodium dodecyl sulfate (SDS) according to the same recipe as for SC.

Polymer-wrapped SWCNTs

The polymer-wrapped nanotube material was prepared by the group of Prof. Manfred Kappes (Karlsruher Institut für Technologie, Germany). A semiconducting (n, m) component of SWCNT raw material was selectively dispersed in toluene using a fluorene-based polymer [128]. The resulting sample material shows relatively bright and stable photoluminescence compared to the SC-wrapped material, and has been used for the investigations of the angular emission.

4.2 CdSe nanowires: sample preparation

The CdSe nanowire material has been synthesized by the group of Prof. Alf Mews (University of Hamburg, Germany) via the solution-liquid-solid (SLS) approach as described in chapter 2.2. After purification they were dispersed and stored in toluene. Most nanowires have a diameter between 8 and 15 nm nanometers, but also thinner and thicker nanowires can be found. For the optical investigations the solution was spin coated on glass cover slides. To remove excess surfactant (TOPO) the samples were rinsed with toluene after spin coating. Figure 4.1 shows two representative confocal PL images of the used CdSe nanowires with straight (a) and branched (b) nanostructures.

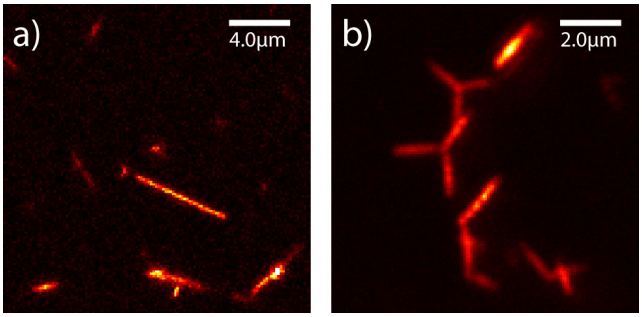

Figure 4.1: Representative confocal PL images of the used CdSe nanowires measured at 650 - 670 nm, showing straight (a) and branched (b) nanostructures.

4.3 Microscope setup

The microscope used throughout this work is based on an inverted optical microscope (Nikon Eclipse TE2000) with oil immersion objectives featuring very high numerical apertures of 1.3 (Nikon CFI S-FLUOR 100x Oil) and 1.49 (Nikon CFI Apo TIRF 60x Oil). Schematics of the setup are shown in figures 4.2 and 4.3 for the acquisition of spectra or radiation patterns, respectively. The excitation beam path is the same in both cases and is depicted in figure 4.2.

4.3.1 Confocal microscope

Excitation

For excitation either a red or an orange HeNe laser with output wavelengths λ_{ex} of 632.8 nm or 594 nm is used. After spectral filtering of the laser line with a laser line filter (LF), the beam is expanded using two pairs of lenses to fill the back aperture of the microscope objective. Optionally the linear Gaussian mode can be converted into a radially polarized doughnut mode by a mode converter (MC) consisting of four $\lambda/2$ wave plate segments [129]. If not mentioned otherwise, such a radially polarized doughnut mode is used in all experiments with the red HeNe laser, while the linear Gaussian mode of the orange HeNe laser is used without modification. The beam is then focused through a tiny pinhole to spatially filter out higher order perturbations. A non-polarizing beam splitter (BS) reflects the excitation light into the microscope objective and to the sample. The sample substrate is positioned on a closed loop x,y-piezo scan stage (Physik Instrumente PI - P-517.3) that allows for raster scanning the sample through the focus with nanometer precision.

For the detection path two setup configurations have been used, the first for confocal imaging in combination with the possibility to acquire emission spectra. The second allows for the acquisition of angular resolved radiation patterns instead of frequency resolved spectra. They will be separately described in the following.

APD imaging in combination with detection of UV/Vis-spectra

A schematic drawing of the first configuration of the experimental setup is shown in figure 4.2. After excitation the optical response emanating from the sample is collected by the high NA objective, transmitted by the beam splitter and finally leaves the microscope as a collimated beam. A notch filter (bandstop at 632.8 nm, Kaiser Optics) then separates the signal from reflected or scattered laser light in the case of $\lambda_{ex} = 632.8\,\text{nm}$. When using the orange laser with $\lambda_{ex} = 594\,\text{nm}$ a long pass filter with a cutoff wavelength $\lambda = 615\,\text{nm}$ is used. Afterwards, the signal is either guided towards two single photon counting avalanche

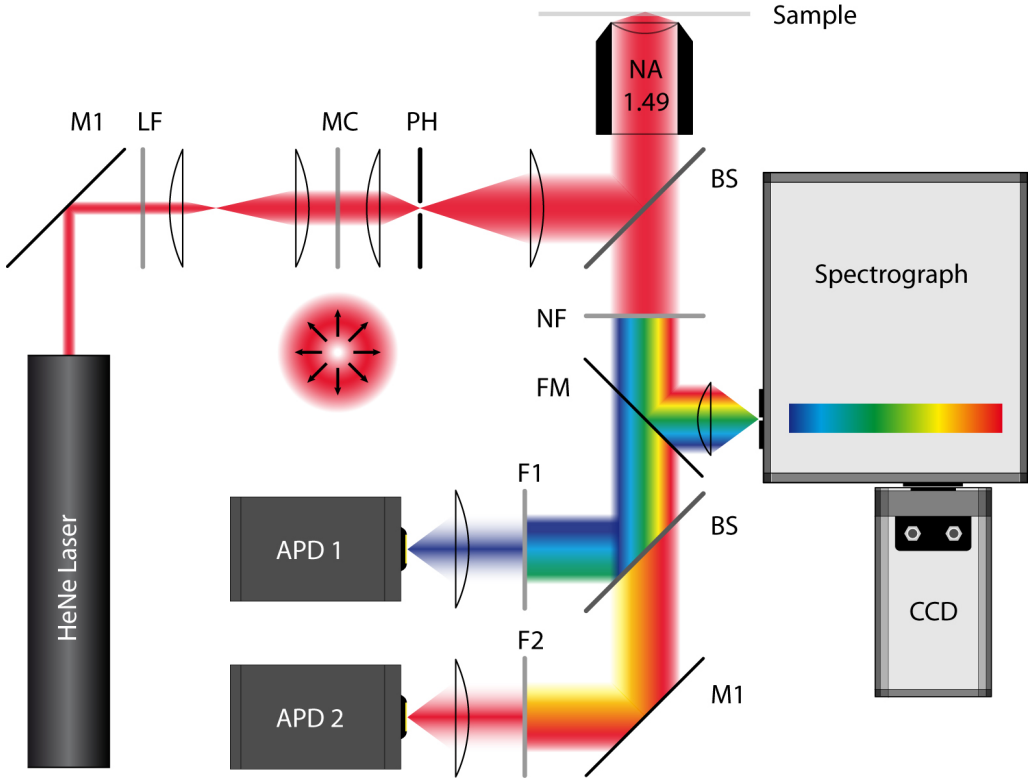

Figure 4.2: Schematic of the experimental setup. After passing a laser line filter (LF) the output of a HeNe laser is expanded, optionally passes a mode converter (MC) and then a tiny pin hole (PH) positioned in the second expansion for spatial filtering. A beam splitter (BS) directs the excitation beam through the high NA objective to the sample. The optical response is collected by the same objective and transmitted by the BS. A notch (or a long pass) filter (NF) separates the signal which is then directed to spectrograph and CCD by a flip mirror (FM) or passes to the APDs with appropriate filtering (F1, F2).

photo diodes (APDs) or it is directed to the spectrometer (Andor shamrock 303i) by a flip mirror (FM), followed by detection with a Peltier-cooled CCD camera (Andor iDus DU420-BR-DD). In case of APD detection the signal is divided by a BS that transmits light with $\lambda > 760\,\text{nm}$ and reflects light with shorter wavelengths. After optional spectral filtering the two beams are focussed onto and detected by two APDs. This configuration including APD detection of different spectral windows allows for the simultaneous detection of Raman and photoluminescence signal of carbon nanotubes. For CdSe nanowires only one APD is used since both Raman scattering and photoluminescence emission occur at wavelengths shorter than 760 nm.

APD imaging in combination with back focal plane imaging

The detection path for the second setup configuration is sketched in figure 4.3. The signal beam which exits collimated from the objective is focused by the tube lens inside the

microscope. It is not collimated again as in the other configuration. A flip mirror is used to direct the signal either to the APDs or to another cooled CCD camera (Andor iDus DU920N-OE or Andor iDus DU420A-OE). In both cases a lens is used to collimate the beam after it has passed a focus. The following filtering and subsequent detection by the ADPs is identical to that in the other configuration. For the acquisition of radiation patterns, which is determined by the intensity distribution in the BFP, a collimating lens, the so called Bertrand lens (BL), forms the image of the objective's back focal plane (BFP) onto the CCD camera (BFP'). For a better signal-to-noise ratio in all patterns pixel binning (4x4) has been applied.

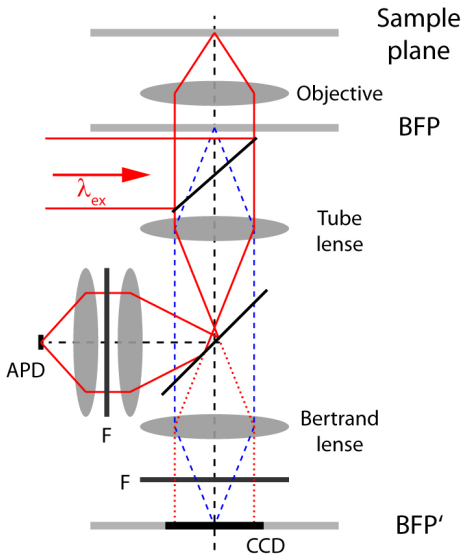

Figure 4.3: Schematic of the experimental setup with the beam paths for APD imaging (red) and radiation pattern detection (blue). Radiation patterns are recorded by imaging the back focal plane of the objective onto a cooled CCD camera using a Bertrand lens (BL) as indicated by the blue dotted lines. Optionally, spectral filters (F) can be used to select the desired detection window.

In this configuration radiation patterns can be recorded reflecting the angular emission of an emitter in a two-dimensional projection. The angular range of the observed patterns is limited by the numerical aperture of the objective, therefore high NA objectives are required to obtain a high degree of information, especially since most of the radiation emanating from a dipolar emitter occurs at large angles.

4.3.2 Near-field configuration

In the near-field experiments a sharp gold tip that operates as optical antenna has to be kept in close and constant distance to the sample surface. For that purpose a home built shear-force atomic force microscopy (AFM) head equipped with a tuning fork is used. The sharp gold tips acting as optical antennas are attached to the tuning fork. The shear-force feed-back mechanism is highly sensitive and applies only small forces, both is essential

for the use of soft gold tips. A frequency-shift-controlled feedback loop, controlled by a phase-locked loop (easyPLL, Nanosurf©) and a scanning probe microscopy controller (SPM1000, RHK Technology), is used to keep the distance between tip and sample surface constant at a few nanometers. Further details on the shear-force AFM can be found in reference [39].

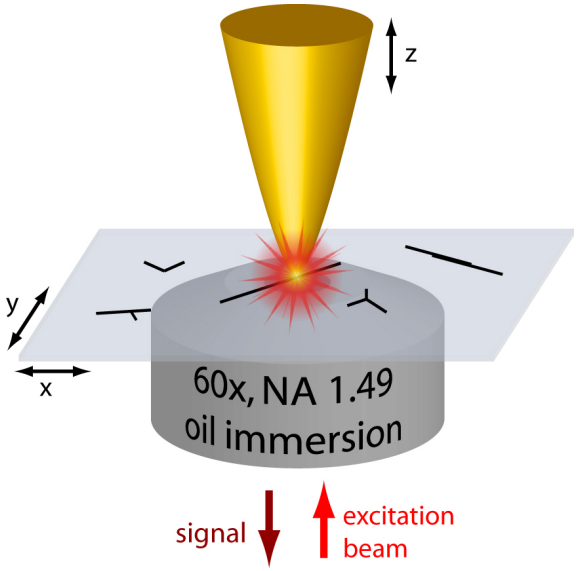

Figure 4.4: Schematic of the experimental setup including the high NA objective, the sample material on a glass substrate and the near-field probe in form of a sharp gold tip. The probe is oriented perpendicular to the sample substrate with the tip axis coinciding with the optical axis of the microscope. For image acquisition the substrate with the sample is scanned through the focus while the gold tip only moves in z direction to keep the distance constant.

A scheme of the near-field configuration is shown in figure 4.4 a. A high NA oil immersion objective is approached from below to focus the laser onto a glass cover slip that carries the sample material, for example single-walled carbon nanotubes or CdSe nanowires. The near-field probe in form of a sharp gold tip is approached from above the sample, that is from the lower refractive index side. The axis of the tip coincides with the optical axis of the microscope (on-axis configuration).

4.4 Preparation of gold tips

Sharp gold tips like the one depicted in figure 4.5 b have been electrochemically etched from pure gold wires (⌀ 100 µm, 99.995% Chempur) in high purity hydrochloric acid [130–132]. A scheme of the etching setup is depicted in figure 4.5 a. A platinum ring dipping into the acid serves as counter electrode to the gold wire. The applied square DC pulses with an amplitude of 8 V, a duration of 30 µs length and a repetition rate of 3 kHz were applied manually via an additional on/off switch. By this procedure gold tips with diameters in

the range of 10-40 nm at the tip apex were obtained. Characterization of the gold tips was done by scanning electron microscopy (SEM).

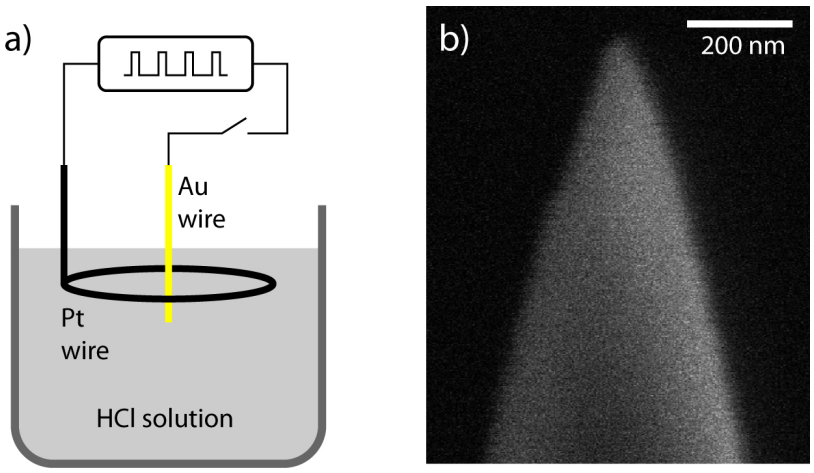

Figure 4.5: a) Schematic of the etching setup including the platinum electrode and the gold wire that dip in hydrochloric acid, and the associated voltage supply. b) SEM image of a typically sharp gold tip used as near-field probes in TENOM experiments. The tip apex has a radius of about 30 nm.

Although the gold tips produced according to this method appear to be similar, one has to keep in mind that each tip is unique regarding the apex size, opening angle, surface roughness, symmetry and material quality. Characterization using scanning electron microscopy allows for the choice of appropriate tips for the TENOM experiments, but slight variations in the geometry can not be avoided which result in more or less differing optical properties affecting the signal enhancement and the radiation pattern. However, a careful selection of probes results in reliable near-field enhancement and only small discrepancies from a radial symmetry which is important for this work.

5 Near-field signal enhancement on SWCNTs

This chapter is based on the paper *"Enhancing and redirecting carbon nanotube photoluminescence by an optical antenna"* that has been published in *Optics Express* (volume **18**, page 16443 (2010)).

Tip-enhanced near-field optical microscopy is a well established tool for the optical investigation of single-walled carbon nanotubes. The enhanced optical fields at the tip apex lead to an increase of the excitation and the emission rate and thus to an increased signal intensity, a higher detection sensitivity and high spatial resolution. The signal enhancement is known to occur only within the range of few nanometers owing to its near-field nature. The overall enhancement factor can be estimated by comparing the signal intensities in the presence and in the absence of the near-field probe, normalized by the size of the far-field and near-field foci given by the factor V in equation 3.8. However, the overall enhancement factor does not distinguish between excitation and radiative rate enhancement (F_{ex}, F_{rad}), which is interesting for a better understanding of the enhancement mechanisms as well as for a further improvement of the technique itself. It turned out to be very difficult to distinguish the single rate enhancement factors from experimental data. Only a semi experimental ansatz could be found in literature, where the excitation enhancement factor is calculated theoretically and the remaining enhancement is attributed to enhancement of the radiative rate [133]. A straight forward experimental differentiation of the individual rate enhancement factors as well as their quantification was thus still lacking.

A way to distinguish and quantify the enhancement factors for excitation and emission rate is presented in this chapter. It is based on the observation and the careful evaluation of the angular emission characteristics of dipolar emission. The angular emission was investigated by imaging the back focal plane of the microscope objective resulting in so called radiation patterns. In addition, these measurements also show that the signal enhancement is connected to a spatial redistribution of the emission.

In the first section, a basic near-field measurement is presented demonstrating the high signal enhancement and a high spatial resolution at optical wavelengths, for Raman scattering as well as photoluminescence emission. Angular radiation patterns of single carbon nanotubes' photoluminescence that were observed in the back focal plane of a microscope objective are shown in section 5.2. A comparison of the results with calculated patterns

shows that the emitting nanotube can be described by a single in-plane point dipole with the axis of the transition dipole oriented along the nanotube axis. Following this, the near-field interaction between a nanotube and an optical antenna was investigated, as used in TENOM. The optical antenna was found to modify the angular emission of PL significantly (section 5.3). It will be shown that the radiation pattern becomes dominated by the characteristics of the antenna and that this directional redistribution of the photoluminescence emission is connected to the radiative rate enhancement. Separation and quantification of antenna induced excitation and radiation enhancement is discussed in section 5.4.

5.1 TENOM on SWCNTs

In figure 5.1, the TENOM data for a thin bundle of photoluminescent SWCNTs spin coated onto a glass cover slip are depicted. The topography is shown in figure 5.1 a. It is dominated by rather uniform layers of surfactant molecules remaining from sample preparation. The Raman signal in figure 5.1 b was detected by an APD after spectral filtering using a narrow bandpass filter to select the vibrational energy of the Raman G-band at 1600 cm^{-1}. A second APD in combination with a broad bandpass filter centered at 950 nm was used to simultaneously record the PL from semiconducting SWCNTs (figure 5.1 c).

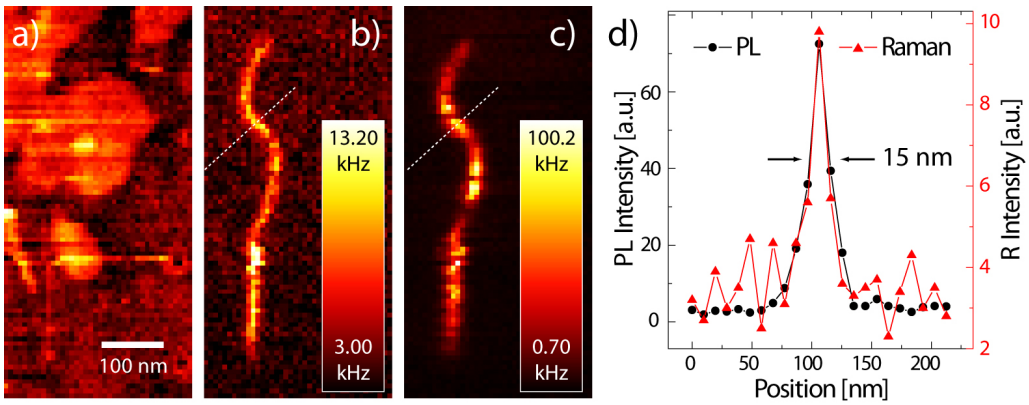

Figure 5.1: TENOM data of SWCNTs on glass. a) The topography image mainly shows layers of surfactant molecules with a rather uniform height of about 1.3 nm. The SWCNTs are hardly visible based on topography data. The simultaneously recorded Raman (b) and PL maps (c) clearly reveal the SWCNTs with high image contrast. d) Cross-sections taken from the Raman and PL images demonstrate a spatial resolution of 15 nm at optical frequencies. Material: SC-wrapped HiPCO nanotubes.

The PL and Raman images reveal a huge signal enhancement due to the near-field interaction with the gold tip resulting in a spatial resolution of 15 nm as determined from the cross-sections shown in figure 5.1 d. While the nanotubes are hardly visible in the topographical image they are clearly identified in the optical images. Owing to the fact that the confocal background is rather small or, for the Raman scattering, not observable at all, a

comparison of near-field and far-field signal intensities is not feasible. For a detailed study of the enhancement process a quantification of the respective rate enhancement factors is needed.

In the following it will be shown how the observation of the radiation pattern and changes therein induced by the near-field interaction can be exploited to separate and quantify excitation and radiative rate enhancement factors F_{ex} and F_{rad}.

5.2 Angular emission of SWCNTs on a surface

As a first step the angular characteristics of photoluminescence emission of single-walled carbon nanotubes is examined. It is expected to show the characteristics of a point dipole emitter which is oriented horizontally with respect to the sample substrate, because the SWCNTs lie flat on a glass cover slip and the E_{11} transition coincides with the nanotubes long axis. The plane of the nanotubes and thus of their transition dipoles is perpendicular to the optical axis of the system.

To show that the emission actually is of a dipolar nature the emission pattern measured in the back focal plane (BFP) were compared to the simulated emission pattern of a point dipole lying flat on a substrate. The simulations have been performed according to the formulas derived by A. Lieb et al. as described in chapter 3 [112].

The SWCNTs (wrapped with sodium cholate) were spin coated on a glass cover slip which was scanned through the focus of a NA = 1.3 objective. For excitation, the linearly polarized Gaussian beam of an orange HeNe-laser with an output wavelength of $\lambda_{ex} = 594\,\text{nm}$ was used. The PL signal was simultaneously detected by an APD in the range of the E_{11} transition between 880 and 1000 nm. A typical APD image is shown in figure 5.2 a.

For the acquisition of the radiation pattern a bright spot indicating the position of a nanotube is centered on the optical axis of the microscope. This has been done for the three spots marked by the letters b, c and d in figure 5.2 a. The corresponding radiation patterns are displayed in (b-d), respectively. Each experimental pattern has been fitted with a simulated dipole pattern with the angle Φ describing the in-plane dipole orientation as the only fit parameter. As the nanotubes are lying flat on the surface, the angle Θ is assumed to be 90°. The fitted radiation patterns are shown in figure 5.2 e-f.

The theoretical dipole patterns reproduce the measured radiation patterns from the SWCNTs extremely well. Most intensity is detected in an outer ring at emission angles larger than the critical angle and is concentrated into two lobes on opposite sides of the pattern. The orientation of the nanotubes in figure 5.2 were estimated by the fitting procedure to be $\Phi = 142°$, 61° and 35° for the nanotubes b, c and d, respectively. The dipole transition is polarized along the nanotube axis and thus parallel to the sample surface.

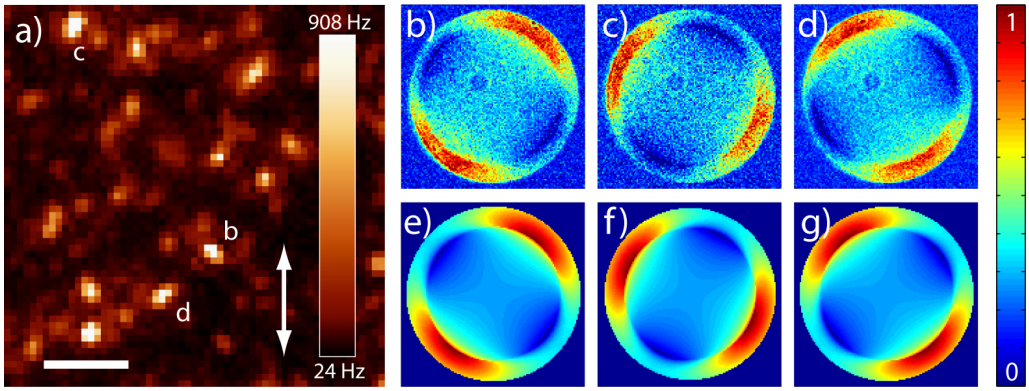

Figure 5.2: a) Confocal photoluminescence image of a sample of single SWCNTs. The scale bar is 2 µm. For the three bright SWCNTs marked b, c and d the observed emission patterns are shown in (b), (c) and (d). The corresponding simulated dipolar patterns are depicted in (e), (f) and (g), respectively. Only the angle Φ which describes the in-plane dipole orientation has been varied to reproduce the corresponding experimental patterns. Simulated and measured radiation pattern agree very well. Material: SC-wrapped CoMoCat nanotubes.

As a conclusion of the excellent agreement between experimentally observed and simulated patterns, the emission arising from exciton recombination in single SWCNTs is found to be dipolar. The mobility of excitons along the nanotube axis can be described by a center of mass motion. This leads to a random distribution of recombination sites within the focus that contribute to the measured radiation pattern. Further, coupling of the photoluminescence emission to spatially extended antenna modes of the nanotube can be excluded because it would result in narrower angular radiation pattern. Simulations using a chain of coherent dipoles indicate that the coherent length would need to exceed 150 nm to obtain a distinguishable radiation pattern.

The same experiment has also been done for another sample material, namely polymer-wrapped single carbon nanotubes. The radiation patterns observed from this material were found to be identical to those from carbon nanotubes wrapped with sodium cholate. The surfactant thus does not significantly alter the angular emission pattern.

To test whether the position of the nanotube with respect to the focal point influences the intensity distribution of the observed radiation pattern, a luminescent carbon nanotube was scanned through the focus and a pattern was recorded at several positions during the scan. Some patterns of the resulting series of patterns are depicted in figure 5.3. The distance between two neighbouring positions of radiation pattern acquisition has been 250 nm, the range covered by the patterns here is thus 1.00 x 0.75 µm. If the polarization of the emission is independent from that of the excitation light, which is longitudinal in the focus center and transversal in a ring around the center, no changes in the intensity distribution are expected. The strongest signal intensity should arise when the nanotube is centered in the focus, where the highest optical fields are located.

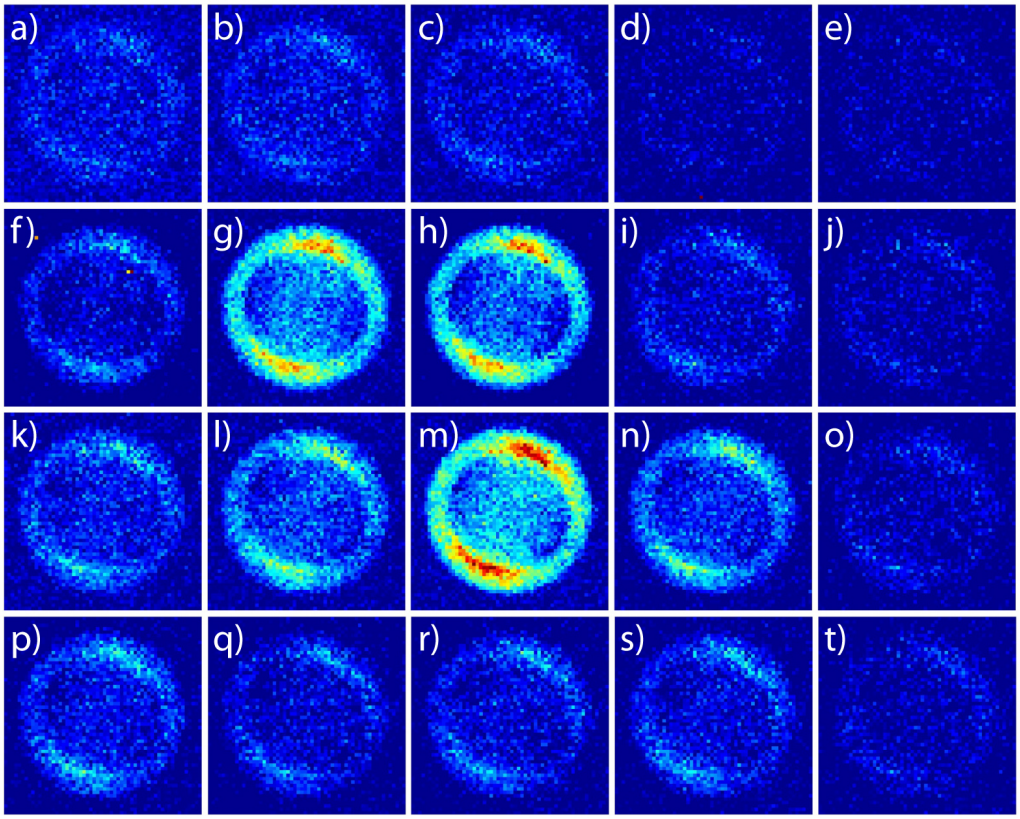

Figure 5.3: Series of radiation patterns from a SWCNT's photoluminescence that have been measured while scanning the nanotube through the laser focus. As expected, the intensity distribution in each pattern does not change when the nanotube is off the optical axis. The signal intensity and the signal-to-noise ratio is maximized when the nanotube is positioned accurately in the focus. Material: SDS-wrapped CoMoCat nanotubes.

It is found that the intensity distribution does not change when the nanotube is off the optical axis of the microscope. This means that the polarization of the emission is independent from that of the absorption. In addition, the imaging properties of the optical system show no observable dependence on the lateral position of the emitter with respect to the intensity distribution in the radiation pattern. Only the signal intensity and therefore the signal-to-noise ratio decreases with increasing offset and is best for an accurately centered nanotube position, where the highest excitation intensity is located. This is the case in figure 5.3 m in the presented example.

5.3 Influence of a near-field probe on the radiation pattern

In the following the influence of an optical antenna in form of a sharp gold tip as used in TENOM experiments will be analyzed. As sample material the polymer-wrapped nanotubes were used. The near-field setup was equipped with a red HeNe-laser with an output wavelength of 632.8 nm and an NA = 1.49 objective. The near-field interaction between

the gold antenna and the carbon nanotube is expected to result in significant changes of the angular emission characteristics. A representative set of experimental data is shown in figure 5.4.

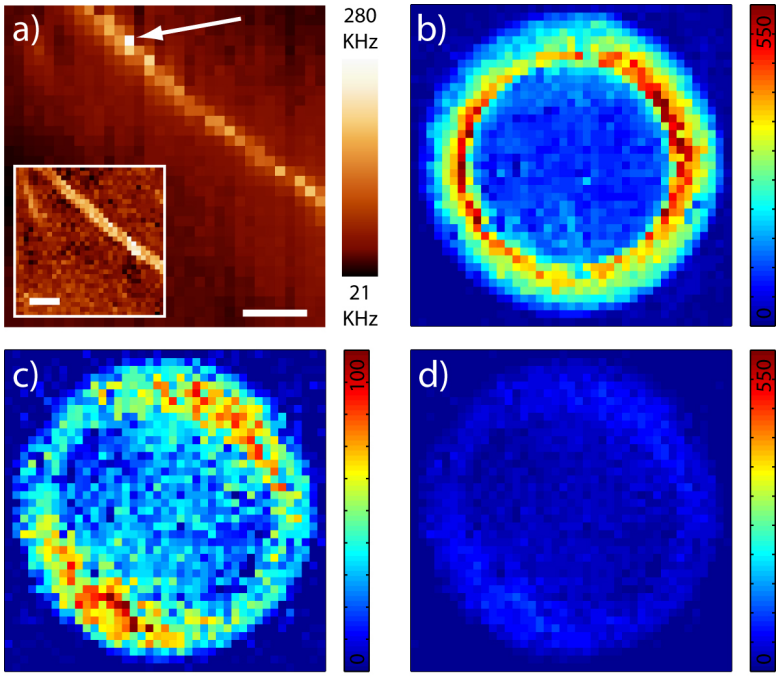

Figure 5.4: a) Near-field image of a luminescent SWCNT with the simultaneously measured topography (inset). The scale bar is 100 nm. The observed radiation patterns from this nanotube are shown in (b-d), where (b) is measured with the tip close to the nanotube (PL^{*}). c) and d) are acquired at the same position while the tip was retracted (PL^{0}_{SWCNT}). For better comparison the intensity-scale in (d) is identical to that in (b). Material: polymer-wrapped nanotubes.

The near-field photoluminescence image presented in figure 5.4 a shows that the gold tip is centered correctly in the objective focus. It exhibits high near-field enhancement resulting in a lateral optical resolution of about 20 nm. The nanotube shows bright PL with uniform intensity along the nanotube. It is oriented from top left to bottom right as can be seen in the PL image (figure 5.4 a) and the simultaneously obtained topographical data shown in the inset.

After optimization of the alignment to provide maximum enhancement by the antenna, the radiation patterns in its presence and absence were acquired for comparison and further data analysis. The radiation patterns are denoted as $\mathbf{PL}^{b}_{a}$, at which the lower index a denominates the emitting dipole (SWCNT or tip) and the upper index b indicates the absence (^{0}) or presence (*) of a near-field probe during the acquisition of a pattern. Note that $\mathbf{PL}^{b}_{a}$ describes the intensity as a function of the angles θ and φ (see figure 3.6).

The radiation pattern in the absence of the antenna, which is denoted as $\mathbf{PL}^{0}_{\mathrm{SWCNT}}$, was measured first, it is shown in figure 5.4 c. Fitting this pattern results in a nanotube orientation of $\Phi = 148°$ in agreement with the PL image and the topography. After approaching

the tip again, a second pattern in the presence of the tip was acquired, denoted as $\mathbf{PL}^*$ (figure 5.4 b). Here, the lower index a has been omitted, because both antenna and nanotube dipole contribute to this radiation pattern. Obviously, the radiation pattern has changed considerably compared to the pattern without antenna (figure 5.4 c). For a better comparison of the overall intensity, $\mathbf{PL}^0_{\mathrm{SWCNT}}$ is plotted again in (d) with the same intensity scaling as in (b). Two differences of $\mathbf{PL}^0_{\mathrm{SWCNT}}$ and $\mathbf{PL}^*$ are found that will be discussed in the following. The first observation is that the overall intensity is strongly increased. This results from the signal-enhancement due to the optical antenna. The second observation is related to the distribution of the intensity in the pattern. Clearly, the angular intensity distribution has changed significantly. The radiation pattern that formerly showed two opposite lobes of maximum intensity is now dominated by a sharp ring close to the critical angle.

The overall signal enhancement results from the interaction of the carbon nanotube with the enhanced electrical fields at the apex of the optical antenna. The presence of the antenna leads to increased excitation and emission rates. A spatial integration of the intensity in both patterns reveals a roughly five-fold number of photons detected in the presence of the gold tip. The near-field interaction also leads to the changes in the emission characteristics and thus to the altered intensity distribution of the observed radiation patterns. A pattern like the one in figure 5.4 b, dominated by a sharp ring is characteristic for a radiating dipole that is oriented vertically with respect to the optical axis. The simulated pattern of such a dipole was depicted earlier in figure 3.6 b. Approaching an optical antenna close to a dipole emitter leads to the creation of a new radiation channel through which energy is transferred from the emitter to the antenna by means of near-field interaction. The transferred energy is finally emitted by the antenna dipole. This antenna emission can be well described by an axially oriented point dipole despite the semi-infinite structure of the optical antenna. The resulting radiation pattern then consists of two coherent contributions, one from the nanotube dipole and a second one from the antenna dipole.

Regarding the transitions rates this means that the radiative rate $\mathrm{k}_{\mathrm{rad,SWCNT}}$ of the carbon nanotube, which is the number of photons emitted per second, is increased by adding a tip-induced radiative rate $\mathrm{k}^*_{\mathrm{rad,tip}}$ according to

$$\mathrm{k}^*_{\mathrm{rad}} = \mathrm{k}_{\mathrm{rad,SWCNT}} + \mathrm{k}^*_{\mathrm{rad,tip}}, \tag{5.1}$$

with the radiative rate in the absence of the tip $\mathrm{k}_{\mathrm{rad,SWCNT}}$ and the resulting radiative rate in the presence of the tip $\mathrm{k}^*_{\mathrm{rad}}$. Here, the fact that exciton decay in carbon nanotubes on flat substrates is dominated by non-radiative channels with $\mathrm{k}_{\mathrm{nr}} \gg \mathrm{k}_{\mathrm{rad,SWCNT}}$ is used. The radiative rate $\mathrm{k}_{\mathrm{rad,SWCNT}}$ of the nanotube dipole is assumed to remain constant in the presence of the tip and thus $\mathrm{k}^*_{\mathrm{rad,SWCNT}} \approx \mathrm{k}_{\mathrm{rad,SWCNT}}$, also moderate radiative rate enhancement factors $\mathrm{F}_{\mathrm{rad}}$ are expected and observed in the experiments.

The following section will show how the observations and findings presented so far can be used to separate excitation and radiative rate enhancements.

5.4 Quantification of excitation and radiation rate enhancement

In conventional TENOM measurements it is not possible to distinguish between radiative and emission rate enhancement since only the final overall signal is detected. In the following data analysis it will be shown that by analyzing the radiation pattern in the presence and absence of the tip, the rates can be separated and quantified independently. This is possible because the radiation patterns of a vertically and a horizontally oriented dipole differ substantially (see chapter 3). As has been shown above, the nanotube emission can be described by a horizontal dipole while emission radiated via the optical antenna can be described by a dipole oriented parallel to the tip axis. In the analysis, the nanotube and the tip emitter are treated independently which leads to a superposition of the radiated intensities. In principle interference of the radiated fields has to be considered since the emission via the antenna is driven by the nanotube's emission. However, the antenna and the nanotube dipole are perpendicular giving rise to orthogonal fields for most of the detected area in the back focal plane. Tip radiation leads to fields with a radial polarization in the detection plane while radiation from the horizontally nanotube dipole is linearly polarized. In the region with parallel polarization, which is in the direction of the nanotube dipole, the intensity of the latter is very weak. Therefore, interference can be neglected in the first approximation.

The total radiation pattern $\mathbf{PL}^*$ from a SWCNT in the vicinity of an optical antenna as detected by the CCD camera can be then divided into two contributions. One contribution is the energy radiated by the horizontal nanotube dipole ($\mathbf{PL}^*_{\mathrm{SWCNT}}$), and the second one that is radiated by the axial antenna dipole ($\mathbf{PL}^*_{\mathrm{tip}}$), according to

$$\mathbf{PL}^* = \mathbf{PL}^*_{\mathrm{SWCNT}} + \mathbf{PL}^*_{\mathrm{tip}}. \tag{5.2}$$

The intensity of the photoluminescence signal observed in the experiments depends on the excitation rate $\mathrm{k_{ex}}$, the quantum yield of the emitting nanotube Q and the detection efficiency η of the system. Further, the fraction γ of the total power radiated by a dipole into the angular detection range defined by the numerical aperture of the system depends on the orientation of the dipole as has been shown in chapter 3. The observed signal intensity is therefore given by the product

$$\mathrm{PL} = \eta \cdot \gamma \cdot \mathrm{Q} \cdot \mathrm{k_{ex}}. \tag{5.3}$$

For the NA = 1.49 objective used here $\gamma_\perp = 0.92$ for a dipole oriented vertically and $\gamma_\parallel = 0.73$ for a dipole oriented horizontally.

The photoluminescence signal intensity radiated by the tip dipole, which gives rise to $\mathbf{PL}^*_{\mathrm{tip}}$, is given by

$$\mathrm{PL}^*_{\mathrm{tip}} = \eta\gamma_\perp \mathrm{Q}^*_{\mathrm{tip}} \frac{\mathrm{k}^*_{\mathrm{ex}}}{V}. \tag{5.4}$$

Here, $\mathrm{k}^*_{\mathrm{ex}}$ is the excitation rate in the presence of the antenna limited to the near-field interaction range, and $\mathrm{Q}^*_{\mathrm{tip}}$ is the quantum yield for the tip channel available for excitons in this interaction range, given by

$$\mathrm{Q}^*_{\mathrm{tip}} = \frac{\mathrm{k}^*_{\mathrm{rad,tip}}}{\sum \mathrm{k}^*}.$$

$\sum \mathrm{k}^*$ is the sum of all decay rates given by $\sum \mathrm{k}^* = \mathrm{k}^*_{\mathrm{rad,SWCNT}} + \mathrm{k}^*_{\mathrm{rad,tip}} + \mathrm{k}^*_{\mathrm{nr}}$ including the non-radiative rate $\mathrm{k}^*_{\mathrm{nr}}$. The photoluminescence signal intensity radiated by the nanotube dipole, which gives rise to $\mathbf{PL}^*_{\mathrm{SWCNT}}$, is given by

$$\mathrm{PL}^*_{\mathrm{SWCNT}} = \eta\gamma_\parallel \mathrm{Q}^*_{\mathrm{SWCNT}} \frac{\mathrm{k}^*_{\mathrm{ex}}}{V} + \mathrm{PL}^0_{\mathrm{SWCNT}} \left(1 - \frac{1}{V}\right). \tag{5.5}$$

Here $\mathrm{Q}^*_{\mathrm{SWCNT}}$ is the quantum yield for the nanotube channel available for excitons in the near-field interaction range, given by

$$\mathrm{Q}^*_{\mathrm{SWCNT}} = \frac{\mathrm{k}^*_{\mathrm{rad,SWCNT}}}{\sum \mathrm{k}^*}.$$

The two parts on the right side of equation 5.5 account for signal contributions from the range of near-field interaction with the antenna and from the remaining far-field focus range, respectively. The constant factor V in the equations above accounts for the different sizes of the confocal focus and the much smaller spot underneath the tip apex in which the enhanced excitation and radiation takes place, as introduced in equation 3.8. In the example in figure 5.4, V is about $300\,\mathrm{nm}/20\,\mathrm{nm} = 15$ as determined from the width of the PL signals in the confocal and near-field optical images.

The enhancement factors for excitation and radiation are denoted $\mathrm{F_{ex}}$ and $\mathrm{F_{rad}}$, respectively. $\mathrm{F_{rad}}$ is given by

$$\mathrm{F_{rad}} = \frac{\mathrm{k}^*_{\mathrm{rad}}}{\mathrm{k_{rad,SWCNT}}} = \frac{\mathrm{k}^*_{\mathrm{rad,SWCNT}} + \mathrm{k}^*_{\mathrm{rad,tip}}}{\mathrm{k_{rad,SWCNT}}} \approx 1 + \frac{\mathrm{k}^*_{\mathrm{rad,tip}}}{\mathrm{k_{rad,SWCNT}}}, \tag{5.6}$$

following the same approximation as earlier in equation 5.1. The ratio of the quantum yields underneath the tip can then be written as

$$\frac{\mathrm{Q}^*_{\mathrm{tip}}}{\mathrm{Q}^*_{\mathrm{SWCNT}}} \approx \frac{\mathrm{k}^*_{\mathrm{rad,tip}}}{\mathrm{k_{rad,SWCNT}}}, \tag{5.7}$$

and equation 5.6 can be transformed to

$$\mathrm{F_{rad}} = \frac{\mathrm{Q}^*_{\mathrm{tip}}}{\mathrm{Q}^*_{\mathrm{SWCNT}}} + 1. \tag{5.8}$$

Finally, equations 5.4 and 5.5 are inserted after rearranging, which results in

$$\mathrm{F_{rad}} = \frac{\mathrm{PL}^*_{\mathrm{tip}}}{\mathrm{PL}^*_{\mathrm{SWCNT}} - \mathrm{PL}^0_{\mathrm{SWCNT}}(1 - 1/V)} \cdot \frac{\gamma_\parallel}{\gamma_\perp} + 1. \tag{5.9}$$

$\mathbf{PL}^0_{\mathrm{SWCNT}}$, which is the intensity distribution of the emission radiated by the SWCNT dipole in the absence of the tip, is already known from the experiment without tip. In the example in figure 5.4 it is identical to the pattern in (c). The spatial integration of $\mathbf{PL}^0_{\mathrm{SWCNT}}$ gives the intensity $\mathrm{PL}^0_{\mathrm{SWCNT}}$. To solve equation 5.9, the intensity contributions to $\mathbf{PL}^*_{\mathrm{tip}}$ and $\mathbf{PL}^*_{\mathrm{SWCNT}}$, that add up to the observed radiation pattern in the presence of the tip, $\mathbf{PL}^*$, have to be separated. For that purpose the differences of the radiation pattern from a vertical and a horizontal dipole are utilized, which are thus pictured again in figure 5.5.

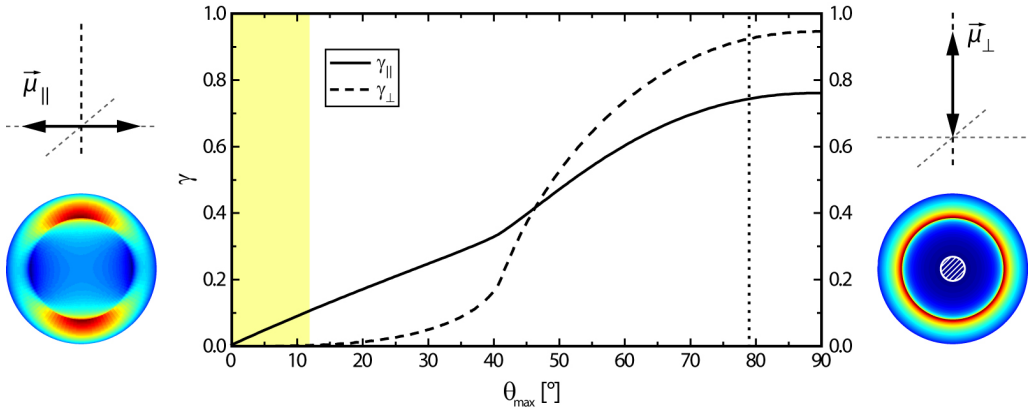

Figure 5.5: The graph shows $\gamma_\perp$ and $\gamma_\parallel$ plotted versus the maximum collection angle θ_{max} of the objective together with the calculated radiation pattern of a horizontal dipole on the left and a vertical dipole on the right. The pattern of a vertically oriented dipole shows no intensity in the center (shaded in white). The corresponding region in the graph is shaded yellow. The pattern of a horizontally oriented dipole does show intensity in this region.

The graph in the middle shows $\gamma_\perp$ and $\gamma_\parallel$ plotted versus the maximum collection angle θ_{max}. At the sides, the calculated radiation pattern of a horizontally oriented dipole (on the left) and of a vertically oriented dipole (on the right) are pictured. The radiation pattern of a vertical dipole shows hardly any intensity in the central region from $\theta = 0\text{-}12°$ (shaded in white in the pattern). Here, $\gamma_\perp$ is approximately zero (yellow shaded region in the graph). This applies to the axially antenna dipole pattern. The radiation pattern of a horizontal dipole on the other hand shows significant intensity in the central region. All intensity in $\mathbf{PL}^*$ that occurs in this central region is thus emitted via the horizontally oriented nanotube dipole resulting in $\mathbf{PL}^*_{\mathrm{SWCNT}}$. Compared to the pattern in the absence of the tip, it is enhanced because of excitation rate enhancement, since we assume that all additional emission caused by radiative rate enhancement is radiated via the tip dipole.

Below saturation, the excitation rate is proportional to the intensity of the optical fields I_E and thus proportional to the absolute square of the electrical field. The excitation rate enhancement factor $\mathrm{F_{ex}}$ is defined by the ratio of the excitation rates in the presence and the absence of the tip, hence

$$\mathrm{F_{ex}} = \frac{\mathrm{k^*_{ex}}}{\mathrm{k^0_{ex}}} = \frac{I^*_E}{I^0_E}. \tag{5.10}$$

In the absence of the tip, the measured signal is proportional to the field intensity and the size of excitation spot given by V_{ff},

$$\mathrm{PL}^{0}_{\mathrm{SWCNT}} \propto V_{ff} I^{0}_{E}.$$

In the presence of the tip, the measured signal is proportional of the sum of excitation in the near-field interaction range and far-field excitation in the remaining far-field focus according to

$$\mathrm{PL}^{*}_{\mathrm{SWCNT}} \propto V_{nf} I^{*}_{E} + (V_{ff} - V_{nf})\, I^{0}_{E}.$$

The ratio of both signals can be written as

$$\frac{\mathrm{PL}^{*}_{\mathrm{SWCNT}}}{\mathrm{PL}^{0}_{\mathrm{SWCNT}}} = \underbrace{\frac{V_{nf} I^{*}_{E}}{V_{ff} I^{0}_{E}}}_{=\frac{1}{V}\mathrm{F_{ex}}} + \frac{V_{ff} I^{0}_{E}}{V_{ff} I^{0}_{E}} - \frac{V_{nf} I^{0}_{E}}{V_{ff} I^{0}_{E}}, \tag{5.11}$$

and rearranged to

$$\mathrm{F_{ex}} = \left(\frac{\mathrm{PL}^{*}_{\mathrm{SWCNT}}}{\mathrm{PL}^{0}_{\mathrm{SWCNT}}} - 1 \right) V + 1. \tag{5.12}$$

If the enhancement of the excitation due to the tip is zero, the enhancement factor is unity and $\mathrm{PL}^{*}_{\mathrm{SWCNT}}$ is equal to $\mathrm{PL}^{0}_{\mathrm{SWCNT}}$.

The ratio $\mathrm{PL}^{*}_{\mathrm{SWCNT}}/\mathrm{PL}^{0}_{\mathrm{SWCNT}}$ can be determined by integrating the intensities in the central part of the measured radiation pattern as explained above (see figure 5.5). After inserting the resulting value into equation 5.12, the excitation rate enhancement factor $\mathrm{F_{ex}}$ can be estimated. For the example shown in figure 5.4, it was found to be $\mathrm{F_{ex}} = 32$. This means that 32 times more excitons have been created due to the presence of the optical antenna. After rearrangement of equation 5.12, $\mathrm{PL}^{*}_{\mathrm{SWCNT}}$ can now be estimated, and thus $\mathbf{PL}^{*}_{\mathrm{SWCNT}}$. Now, $\mathbf{PL}^{*}_{\mathrm{tip}}$ is given by the difference $\mathbf{PL}^{*} - \mathbf{PL}^{*}_{\mathrm{SWCNT}}$, and the spatial integration results in $\mathrm{PL}^{*}_{\mathrm{tip}}$, which finally is the last unknown to calculate $\mathrm{F_{rad}}$ according to equation 5.9. For the presented example $\mathrm{F_{rad}}$ was found to be $\mathrm{F_{rad}} = 1.9$, which means that the ratio of emitted PL photons is increased by additional 90 % because of the tip antenna.

In principle, the equations derived above only hold for systems with non-mobile excited states such as single fluorescent molecules or semiconductor nanocrystals. In such systems the position of the excited state is always in the range of the near-field interaction between emitter and antenna. Excitons in SWCNTs, however, are not localized but highly mobile along the nanotube axis. A diffusion range of about 100 nm has been reported in literature [44, 118, 134]. As a consequence a substantial fraction of excitons created by strongly tip-enhanced excitation can leave the local near-field interaction region. After escaping this narrow region they are no longer object to possible radiative rate enhancement but will all contribute to the $\mathbf{PL}^{*}_{\mathrm{SWCNT}}$ pattern in the case of radiative relaxation. Hence, a treatment derived for zero-dimensional structures underestimates the actual radiation enhancement factor $\mathrm{F_{rad}}$ in the case of higher-dimensional systems like carbon nanotubes. A

simulation of the competition between exciton diffusion and local radiative rate enhancement was performed by calculating the time-dependent spatial distribution of the exciton density after local antenna enhanced excitation using a 1D random-walk model [45]. The only input parameters are the near-field interaction range of 20 nm and the diffusion range of 100 nm. The result is a significantly increased radiative rate enhancement $k^*_{rad,tip}$ owing to the tip. The actual radiative rate enhancement factor F_{rad} in the example in figure 5.4 is then 7.8.

The used gold tips are electrochemically etched individually and hence have differing enhancement capabilities. The observed enhancement factors for different tips and also different nanotubes range from F_{ex} = 12-32 and F_{rad} = 6.1-13.6. The variation of enhancement factors is attributed to non-optimal positioning of the tip on top of the nanotube and minor differences in tip shapes leading to a variability of antenna efficiencies.

For all investigated SWCNTs and gold tips, excitation enhancement was substantially higher than radiation enhancement even after accounting for exciton mobility effects. Two reasons are responsible for this observation. First, there is a stronger field enhancement at the excitation wavelength compared to the emission wavelength. Photoluminescence spectra of metal nanostructures are known to reflect the wavelength dependence of the field enhancement which is dominated by plasmon resonances in the visible range [135]. Luminescence spectra of gold tips, resulting from interband transitions of d-band electrons into the conduction band and subsequent radiative recombination, show maximum intensity in the range of the excitation wavelength at 632.8 nm used in the TENOM experiments [136]. The intensity at the emission wavelength of carbon nanotubes (at around 950 nm) is at least 20 times smaller. One representative example spectrum of gold tip luminescence, measured after excitation at 473 nm, is shown in figure 5.6 (solid line) together with the PL spectrum of a (6,5) nanotube (dashed line). The tip PL spectrum has been corrected for the sensitivity of the CCD and the reflectivity of the grating, since both show significant variations in the broad spectral range of the tip PL.

The second reason for the higher excitation enhancement is based on the polarization of absorbing and emitting states. Emission at the exciton energy E_{11} is polarized in-plane as can be seen from the radiation patterns and the literature cited above. Treating the near-field interaction between tip and nanotube as dipole-dipole coupling only weak effects are expected due to the orthogonal orientation of the dipoles. In principal, radiative rate enhancement would be expected to occur twice along the nanotube at opposite sites displaced from the tip center, since the optical fields at the tip are polarized radially around the tip. On the other hand, excitation at 632.8 nm is within the range of the E_{12} transition of the investigated SWCNTs that is polarized perpendicular to the nanotube axis. For far-field excitation this absorption is screened efficiently by the nanotubes' polarizability. However, since strongest field enhancement is obtained for these perpendicular fields with very high field gradients, excitation at E_{12} may become allowed in the presence of the tip [32].

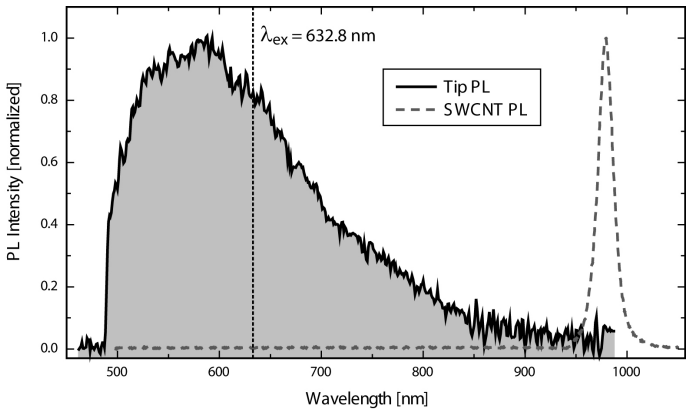

Figure 5.6: Photoluminescence spectra of a gold tip (solid line) and a single (6,5) carbon nanotube. The output wavelength of a red HeNe-laser at 632.8 nm is in the range of the tip luminescence. Photoluminescence signals of the gold tip and the nanotube, however, do not overlap.

A horizontally oriented dipole in the tip induced by the nanotube could also contribute to the radiation pattern detected as $\mathbf{PL}^{*}_{\mathrm{SWCNT}}$, even though the radiation would emanate from the tip. This would result in an underestimation of $\mathrm{F_{rad}}$ and an overestimation of $\mathrm{F_{ex}}$. However, its contribution will be small compared to that of the vertical tip dipole due to the small polarizability of the tip perpendicular to its axis. For a complete estimation of the respective contributions the one-dimensional structure of the nanotube needs to be considered. Since radiative rate enhancement is limited due to strong competition with exciton mobility as discussed before, the small contribution of the horizontal tip dipole can also be neglected compared to that of emission via the nanotube dipole. Therefore, the uncertainty introduced by neglecting the horizontal tip dipole is estimated to be smaller than 10 %.

Usually, the observed radiation patterns induced by the tip slightly deviate from a perfect radial symmetry as predicted by the simulation. This is attributed to non-ideal tip shapes of the electrochemically etched gold tips. It is noteworthy that the radial polarization of the tip emission implicates that the tip antenna is excited efficiently using a radially polarized doughnut mode. In general, the radiation pattern detected for a given antenna system will reflect the optimum excitation pattern at the detected frequency as a consequence of reciprocity. After detecting the radiation pattern of a given antenna, its coupling efficiency could be optimized by vector point spread function engineering.

Conclusion

In this chapter investigations of the enhancement mechanisms in tip-enhanced near-field optical microscopy on photoluminescent SWCNTs were presented. For that purpose the back focal plane of the microscope objective was imaged with a CCD camera. It was found that the photoluminescence emission of semiconducting single-walled carbon nanotubes

on a dielectric substrate can be modelled as emission from a single in-plane point dipole despite the one-dimensional structure of the nanotubes. The signal enhancement due to a sharp gold tip regarded as optical antenna in the close vicinity of a carbon nanotube originates from enhanced excitation and additional radiation via the tip dipole. The enhancement process was found to be connected to a spatial redirection of the emission, which in turn allows for some control of the emission. These results illustrate that optical antennas could be used to improve the performance of carbon nanotube based nanoscale NIR emitters and absorbers. Furthermore, the enhancement factors of excitation (F_{ex}) and radiation (F_{rad}) have been quantified independently by analyzing the radiation patterns. In the present system of nanotube and gold tip, enhancement of the excitation rate was found to dominate the overall enhancement.

6 TENOM on CdSe nanowires

The following chapter reports on the TENOM investigations of CdSe nanowires. It is based on the papers *"Optical Imaging of CdSe Nanowires with Nanoscale Resolution"* that has been published in *Angewandte Chemie International Edition* (volume **50**, page 11536 (2011)) and *"Tip-Enhanced Near-Field Optical Microscopy of Quasi-1D Nanostructures"* published in *ChemPhysChem* (volume **13**, page 927 (2012)).

Variations of the photoluminescence signal along single CdSe nanowires regarding intensity as well as energy are known from confocal measurements. Spatial averaging over a sample area of a diffraction limited focal spot size, however, hides variations that occur on a length scale below 200 nm, which could be important for the development of components for nanoscale devices. On the other hand, HRTEM measurements revealed changes in the crystal structure in the range of only few nanometers from which changes in the optical properties are expected [16]. Additional inhomogeneities of the nanowire diameter or in its surrounding should also result in variations of the optical properties on nanometer length scales.

In the following it will be shown that tip-enhanced near-field optical microscopy provides the required high detection sensitivity and spatial resolution to gain deeper insight into the optical properties of these structures on the nanoscale. Imaging with the detection of the integrated signal from the sample in a particular spectral window reveals nanoscale intensity variations along single CdSe nanowires. Two example measurements are presented in section 6.1.

A more sophisticated technique is hyperspectral imaging, where the complete spectral information is acquired at each pixel, providing the same high spatial resolution but much more spectral information. Here, subsequent data analysis reveals different PL energies emanating from different nanowires. It will be demonstrated that even bundled nanowires can be spatially resolved by their PL and Raman signals. Section 6.2.2 describes variations of the PL energy observed along single nanowires of constant diameter, a feature that is attributed to the polytypism of the crystal structure.

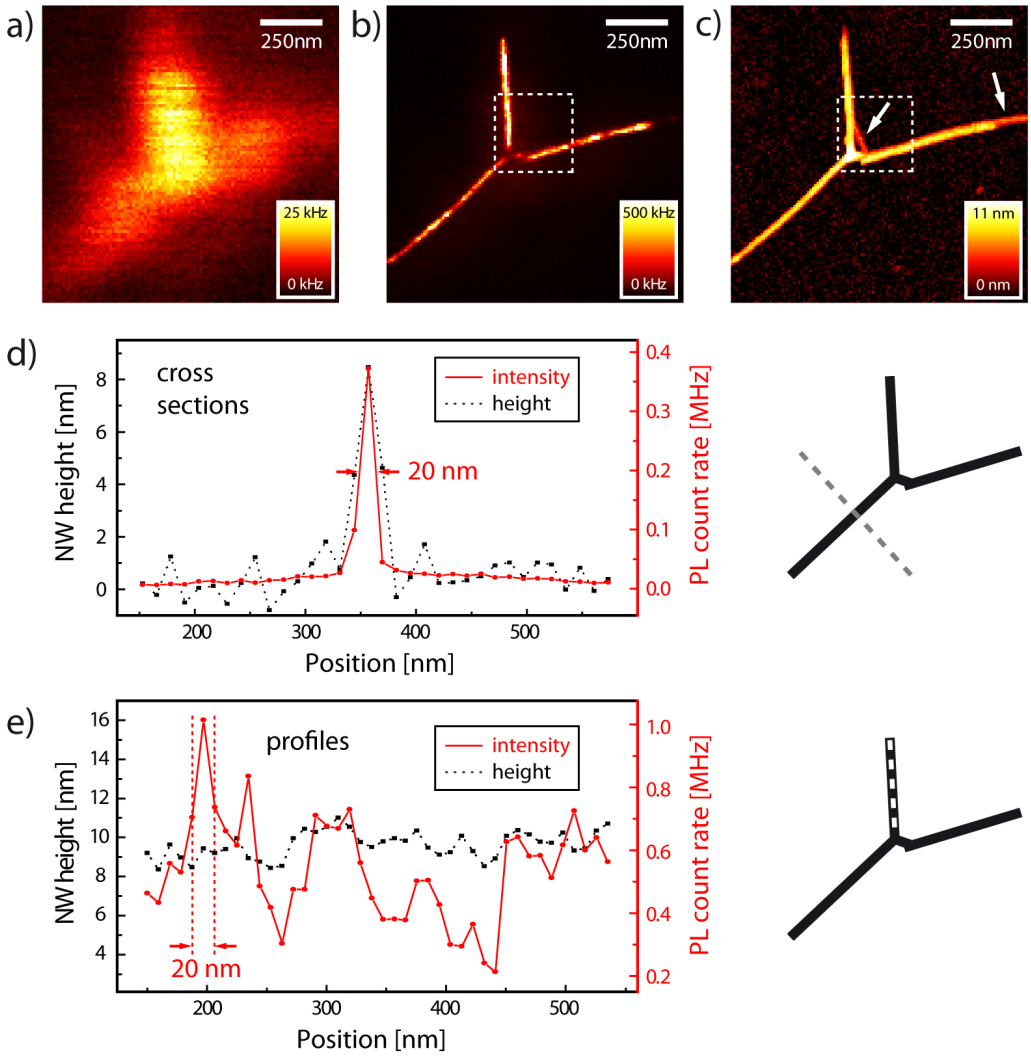

Figure 6.1: Confocal versus TENOM PL image of CdSe NWs on a glass substrate. a) Diffraction-limited confocal image. b) TENOM image of the same sample area as in (a). c) Simultaneously detected topographic image. Local signal enhancement in the vicinity of the gold tip results in substantially enhanced signal intensity leading to a substantially improved spatial resolution in the PL image. This is obvious in the images and additionally shown by a cross section across and a profile along a nanowire shown in (d) and (e), respectively (measured along dashed lines indicated in the insets).

6.1 Near-field imaging using an APD

Figure 6.1 a shows a conventional far-field photoluminescence image of CdSe nanowires. The PL has been detected by an APD after spectral filtering of the PL between 698 nm and 708 nm. Since the PL band of CdSe nanowires is usually rather broad, signals from thicker nanowires with a band gap close to the bulk value as well as slightly blue-shifted signals from thinner nanowires that are subject to quantum confinement effects will be detected in this spectral window. The structure of the nanowire appears to be y-shaped. Figure 6.1 b presents the tip-enhanced near-field PL image that has been measured in the

same area, and figure 6.1 c shows the simultaneously obtained topography. Excitation power and integration time were equal in both PL measurements. Tip-enhancement leads to a substantial increase of the PL intensity by a factor of 20 from about 25 kHz to 500 kHz. The spatial resolution in the PL images has improved drastically from 240 nm to 20 nm as determined from cross sections as well as profiles along a NW as shown in figure 6.1 d and e. The TENOM data reveal that the structure actually is a tripod shape where the right arm is broken close to the branching site. While the NWs are found to be luminescent for their complete length, the PL intensity is seen to vary strongly within few tens of nanometers without significant changes in NW height (figure 6.1 e). The thinner nanowires marked by white arrows in figure 6.1 c are not visible in the PL image since their emission wavelength is too much blue-shifted to pass the detection filter. This will be addressed in section 6.2.

Surprisingly, the PL intensity fades toward the central branching site; the junction core itself is completely dark in an area that is about 30 nm wide. The cores typically have pure ZB structure and could thus be expected to be luminescent. ZB-WZ interfaces, in contrast, result in type-II transitions with reduced oscillator strength because of the partial charge transfer [29]. Modified optical properties could in principle result from the particular dimensionality of the core that could lead to different quantum-confined electronic states or an increased density of defect-related quenching sites. In fact, all branched NWs that have been investigated in this work featured this dark junction sites. A second example is shown in figure 6.2.

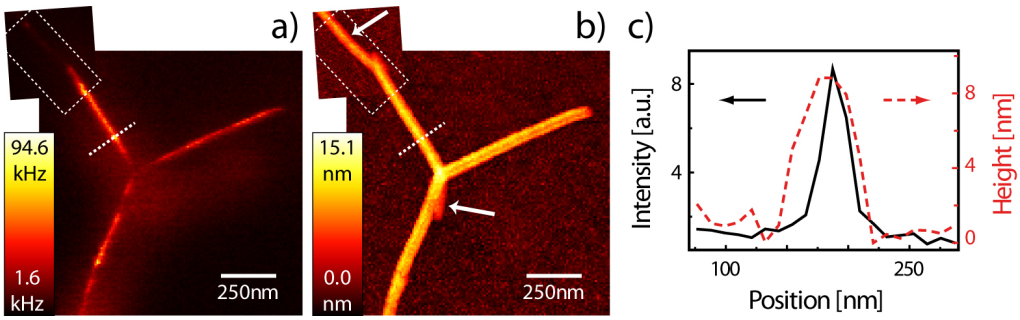

Figure 6.2: TENOM data of CdSe nanowires: Simultaneously measured photoluminescence map (a) and topographical image (b). Some parts of the structure marked with white arrows in the topography are not visible in the PL map because of the limited spectral detection window of the optical measurement. c) Cross-sections taken along the dotted lines reveal high lateral resolution. The spatial resolution of 23 nm obtained in the PL image is substantially higher than the topographical resolution of 53 nm. This is a consequence of the higher order field dependence of the optical signal that scales with the square of the electric field for both excitation and emission rates.

TENOM PL image and topography of a second branched CdSe nanostructure measured with another gold tip are depicted in figure 6.2 a and b. The near-field PL image reveals intensity variations in some regions, for example in the lower left arm in figure 6.2 a, whereas other sections show rather homogeneous PL. Cross-sections that have been taken along the dotted lines reveal a high lateral resolution. The spatial resolution (given by the

full width at half maximum) of 23 nm obtained in the PL image is substantially higher than the topographical resolution of 53 nm. This is a consequence of the higher order field dependence of the optical signal that scales with the square of the electric field for both excitation and emission rates. The lateral resolution in the topography is given by the gold tip which was slightly broadened in this case.

There are thinner NWs present in both measurements shown above that appear dark in the PL images. They are marked by the white arrows in the topographical images in figures 6.1 c and 6.2 b. These thinner nanowires do not show any emission in the spectral detection window defined by the bandpass filter in front of the photodiode. To obtain additional information on the PL bands of these nanowires, hyperspectral images in which complete spectra are recorded at each image pixel were acquired. They also contain details on the PL energies and the LO Raman band that has not been considered so far.

6.2 Hyperspectral imaging

Hyperspectral imaging (HI) achieved by recording complete emission spectra at each image pixel provides detailed information beyond a simple visualization by integrating the signal in a filtered spectral window. The obtained set of spectra allows not only to image with a single spectral window, but the distribution of any spectral property can be visualized. This includes imaging of the spectral position and lineshape of specific peaks in the spectra.

6.2.1 Nanowires of different diameter

From each of the CdSe nanostructures presented above a smaller area has been further investigated by hyperspectral imaging. The results are presented in figures 6.3 and 6.4.

Figure 6.3 shows hyperspectral imaging data measured in the area marked by the dashed box in figure 6.2. In the topographical image in figure 6.3 a two NWs appear, a thinner one in the upper part and a thicker one in the lower part of the image with diameters of (6.5±0.5) nm and (8.0±0.5) nm, respectively. Two example spectra taken from the hyperspectral data are depicted in figure 6.3 b. The respective PL bands have energies differing by 72 meV, while both have energies above the bulk value of CdSe of 1.74 eV. Figure 6.3 c displays a false coloured PL intensity map formed by integrating the intensities within the spectral windows marked in figure 6.3 b and showing the contributions of the two respective bands in blue and red. The integration windows are chosen in such a way that no contribution from the other band adds to the intensity. Apparently, the low energy band (red) originates from the thicker NW in the lower part of the image, whereas the thinner NW features blue-shifted PL (blue). The increase of the band gap with decreasing diameter, a result of quantum confinement, is clearly visible. The spectra in figure 6.3 b also exhibit a Raman peak at 209 cm^{-1} (1.934 eV) that results from the longitudinal optical

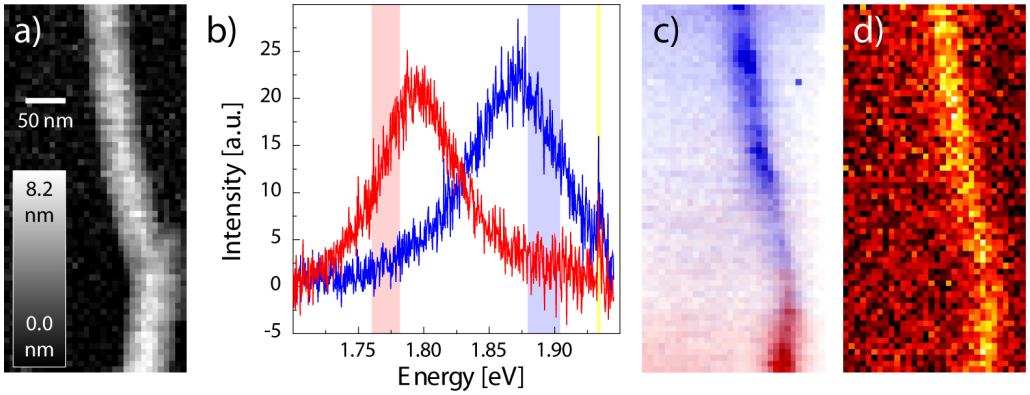

Figure 6.3: Hyperspectral image data of the area marked by the dashed box in figure 6.2. a) The sample topography reveals two NWs of different diameter. b) Two example spectra showing a Raman peak at 1.934 eV as well as PL bands at different energies (1.797 meV and 1.869 meV). c) Integration of the PL bands within the spectral windows in (b) results in the corresponding PL intensity maps coloured blue and red for the respective windows. d) Raman map obtained by integrating the area marked yellow in (b).

phonon mode (LO). Integration of the Raman signal leads to the Raman map depicted in figure 6.3 d, which does not show substantial intensity variations along the nanowire in contrast to the PL data. While the electronic energies vary strongly with the diameter due to quantum confinement, the phonon energies mainly reflect the crystal structure. However, the Raman signal in this example is very weak and variations might be hidden in the noise.

Figure 6.4 presents hyperspectral imaging data of the central region of the CdSe nanostructure which has been shown in figure 6.1. From the topographical data the diameters of the nanowires are determined to be (5.0±0.5) nm for the thin nanowire and (9.0±0.5) nm for the two thicker arms of the branched structure from which the right one is broken. Again two example spectra of this measurement are depicted in figure 6.4 b taken at positions I and II marked in the topographical image obtained simultaneously (figure 6.4 a). Spectrum I is dominated by a broad PL band at around 1.772 eV labelled (1), spectrum II features an additional PL band at around 1.880 eV labelled (2). In both spectra the LO Raman peak at 209 cm^{-1} (1.934 eV) is visible. The contributions of the two PL bands were determined by fitting each spectrum with two Gaussian line shape functions. The resulting amplitude images were normalized and plotted together in the intensity map depicted in figure 6.4 c. Clearly, the low energy PL band (1; red in figure 6.4 c) originates from the thicker three-armed CdSe nanostructure, whereas the thinner NWs show blue-shifted PL energy (PL band (2); blue). Again, the increase of the band gap with increasing quantum confinement is visible.

The optical TENOM data reveals that there are a thinner nanowire and a thicker one bundled together in the lower right part of the scanned area, that can hardly be distinguished

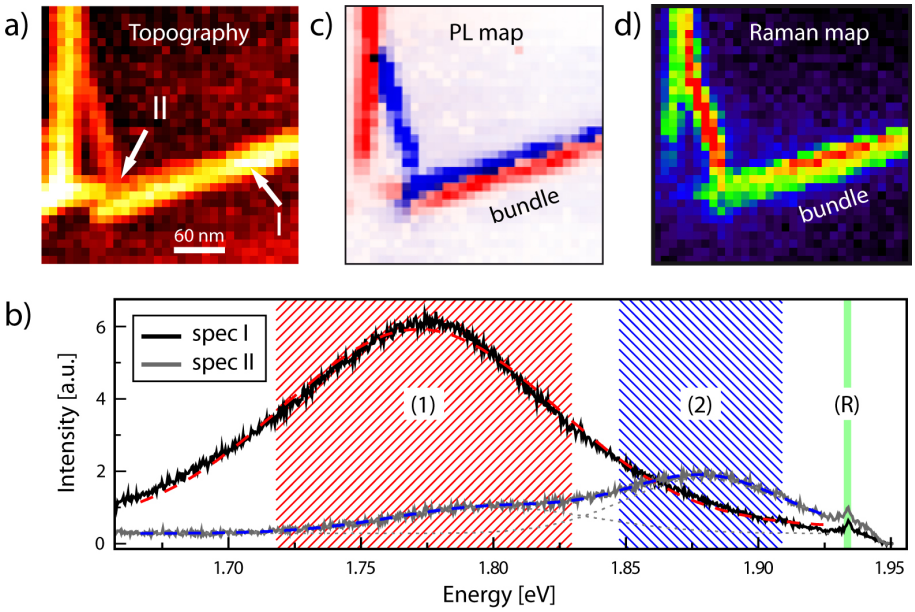

Figure 6.4: Hyperspectral imaging of the CdSe nanowires as marked in figure 6.1 c by the dashed boxes. a) Topographical image data. b) Spectra taken at the positions marked in (a) show PL bands at around 1.772 eV (1) and 1.880 eV (2) that can be described by Gaussian line shape functions. A Raman band (R) corresponding to the LO phonon is visible at 1.934 eV. c) Intensity maps of PL (1; red) and PL (2; blue) bands show higher PL energies for thinner NWs. d) The Raman map reveals stronger scattering for thinner NWs. In the hyperspectral image the two NWs forming the bundle are clearly resolved by the PL and the Raman signal.

in the topography. The diameter of the thicker nanowire is estimated to be (9.0±0.5) nm, for the thinner NW such an estimation is not possible since the nanowires are not resolved by the AFM probe. However, they are clearly resolved and localized with TENOM based on their optical characteristics. The PL intensities of the thinner nanowires are comparable and apparently independent of their distance from the thicker ones. This implies that there is no efficient energy transfer from the higher band gap nanowire to the one with a smaller band gap within the bundle since this would result in quenching of the photoluminescence from the nanowire with the larger band gap, i.e. the nanowire coloured in blue in the present example.

The Raman map depicted in figure 6.4 d results from integrating the intensity of the Raman signal. The chosen spectral window is indicated in green in figure 6.4 b. It can be seen that the nanowire bundle is also resolved spatially in the Raman map. The data reveals stronger Raman scattering from the thinner nanowires in comparison to the thicker ones despite their smaller material volume. This effect can be attributed to resonance Raman scattering, which leads to a stronger Raman scattering signal of thin nanowires with band gap energies closer to the energy of the scattered photon. For the thin nanowire in the other example (figure 6.3) with a diameter of (6.5±0.5) nm this resonance effect was not observable, although the difference of the PL energies is only about 10 meV, which is

small compared to the widths of the bands. However, the worse signal-to-noise ratio resulting from smaller tip-enhancement hinders a detailed interpretation in that case. As a consequence, significant Raman intensity enhancement due to resonance is observed only for diameters smaller than 6 nm and sufficient tip-enhancement.

6.2.2 Energy variations along single nanowires

Some CdSe nanowires were found to exhibit strong spatial variations of the PL energy with shifts of up to several tens of meV. In figure 6.5, the energy map along a 400 nm long NW segment is depicted. For this nanowire a constant height of (8.0±0.5) nm could be determined from the topographical data. In figure 6.5 b, two profiles through the energy map are shown. The solid line was taken on top of the nanowire where tip-sample interactions result in strong signal enhancement. The dashed profile stems from a parallel line where the nanowire was outside of the near-field interaction range of the tip, thus the profile reflects the confocal signal without influence of the tip. While the dashed profile shows a rather uniform increasing energy, the solid line reveals strong variations of the PL energy on length scales as small as the resolution given by the near-field probe, that is about 23 nm. The comparison shows that the tip-enhanced data provides information about variations on a length scale of about 20 nm which are invisible in conventionally measurements because of spatial averaging.

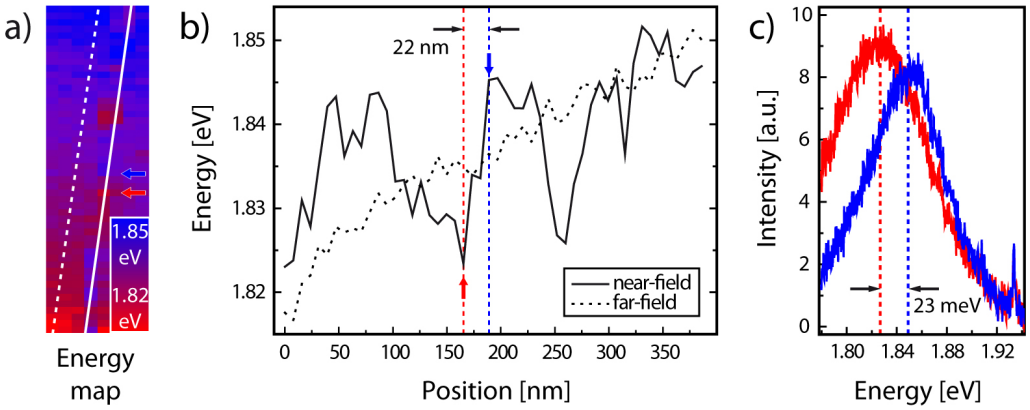

Figure 6.5: a) Energy map of a 400 nm long NW segment with a constant diameter of (8.0±0.5) nm revealing substantial energy shifts on nanometer length scales. b) PL energy profiles measured along the NW with and without the near-field contribution as marked in (a). c) Two spectra recorded at two positions separated by about 23 nm as marked by the red and blue arrows in (a) and (b) show PL bands with an energy difference of 22 meV.

The spectra shown in figure 6.5 c were measured at positions separated by only 23 nm (marked in figure 6.5 a and b by the red and blue arrows). The PL energy difference between these spectra is about 22 meV, revealing energy gradients of up to 1 meV nm^{-1}. Since there are no variations in the nanowire height, significant diameter-related band gap

variations can be excluded. Generally, other possible reasons for the energy variations are inhomogeneities in the surrounding of the nanowire and variations of the crystal structure. In the case presented here, no topographic irregularities were found in the substrate and the sample surface along this nanowire segment.

The used sample material typically shows short segments of alternating ZB and WZ phases revealed in HRTEM measurements (see figure 2.10). The shifts in the PL energy can be thus attributed to variations in the crystal phase with random fractions of zinc-blend and wurtzite structure. The increase of the PL energy from left to right in figure 6.5 b, observable in both profiles, indicates an increasing amount of WZ structure in the nanowires.

Conclusion

Tip-enhanced near-field optical microscopy proved to be extremely well suited for the investigation of the optical properties of inorganic nanowires with nanoscale resolution. Using TENOM, the first high-contrast images of semiconducting CdSe nanowires were obtained and presented in this work and, in addition, first hyperspectral images could be measured providing spectral informations with sub-diffraction spatial resolution.

The optical properties of CdSe nanowires were found to vary significantly on the nanoscale leading to strong spatial fluctuations in both photoluminescence intensities and energies. Energy gradients up to $1\,\mathrm{meV\,nm^{-1}}$ along the quasi 1D structures have been revealed. Simultaneous imaging of PL and Raman scattering by hyperspectral imaging allows for a comprehensive optical characterization of the nanowires. Bundles of nanowires with different diameters could be resolved spatially according to their photoluminescence and Raman scattering signals. As a consequence, a detailed optical characterization of these structures implicitly requires a spectrally resolving imaging technique with sub-diffraction spatial resolution, as provided by TENOM.

7 Near-field signal enhancement on CdSe NWs

In the preceding chapter, the successful application of TENOM for nanoscale imaging of the optical properties of CdSe nanowires has been presented. The following chapter refers to the mechanism of the underlying signal enhancement, it aims at a better understanding of the technique itself. For that purpose investigations of the signal dependency on the distance between a gold tip and a CdSe nanowire will be presented, and the influence of the metal tip on the emission spectrum and on the angular distribution of the photoluminescence signal will be addressed.

The first section 7.1 deals with the emission spectrum as a function of the distance between gold tip and CdSe nanowire. Therefore, approach curves for photoluminescence as well as Raman scattering signals have been acquired. Since the enhanced signal results from near-field interactions between the probe and the sample a very short ranged intensity increase is expected. The model from Cançado et al. regarding Raman scattering enhancement on quasi 1D semiconducting nanostructures will be applied to CdSe nanowires [93]. A question of particular importance regarding PL enhancement is whether the presence of the gold tip alters the spectral characteristics of the sample. It is found that in fact the presence of the gold tip in some cases results in spectral shifts and possible reasons are discussed.

The second and the third sections are focussed on the angular distribution of the photoluminescence emission. Section 7.2 reports on the angular emission characteristics of CdSe nanowires. A comparison of the observed radiation patterns with theoretical calculations shows that despite their quasi 1D structure the assumption of only a single radiating dipole is not sufficient to describe the angular distribution. In section 7.3, the influence of a gold tip on the radiation pattern is investigated, which is found to significantly alter the angular distribution. In the last section asymmetric intensity distributions which sometimes occur in the observed radiation patterns are addressed and possible reasons and consequences are discussed.

7.1 Influence of a NF probe on the emission spectrum

The dependence of the signal enhancement on the distance between tip and sample can be studied by measuring so called approach curves. For that purpose, the integrated signal intensity is recorded as a function of the tip-sample distance. The absolute distance could be measured by decreasing it to zero, where the tip would touch the sample surface. Since this would damage the tip apex, the measurement is usually stopped before this happens. The signal intensity is thus plotted against the tip position relative to the setpoint position, which corresponds to the tip-sample distance used in TENOM imaging. An approach curve for the PL of a single CdSe nanowire is shown in figure 7.1. The resulting data show a steep increase of the PL signal within only a few nanometers, which is specific for signal enhancement induced by short ranged near-field interaction with the gold tip.

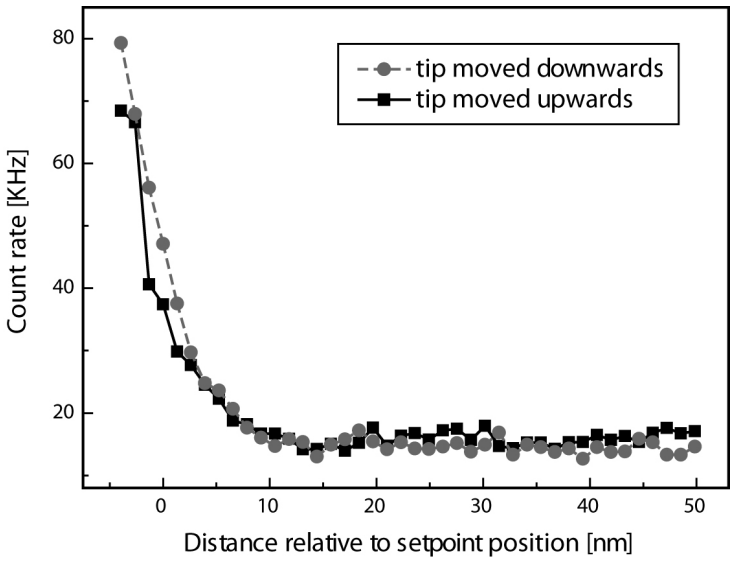

Figure 7.1: Approach curve for CdSe nanowire photoluminescence, showing the integrated signal intensity while a gold tip was approached (grey dashed line) and retracted again (black solid line). The short ranged steep increase of the PL signal is characteristic for near-field enhancement due to the tip.

Such a measurement, however, does not contain any spectrally resolved information. Therefore, series of spectra during approaching and retracting the gold tip to single CdSe nanowires have been measured to obtain the complete optical response as a function of the distance between sample and probe. In this way not only the intensity increase at small distances but also potential spectral shifts are observable and can be analyzed subsequently. An example of such a series of spectra is presented in figure 7.2 a.

The measurement was started while the gold tip was kept in close distance to the sample surface as defined by the setpoint of the shear-force feedback control (topmost spectrum in figure 7.2 a). This tip-sample distance is also used during TENOM image scans and is referred to as setpoint position. After a few spectra with the tip kept in this setpoint

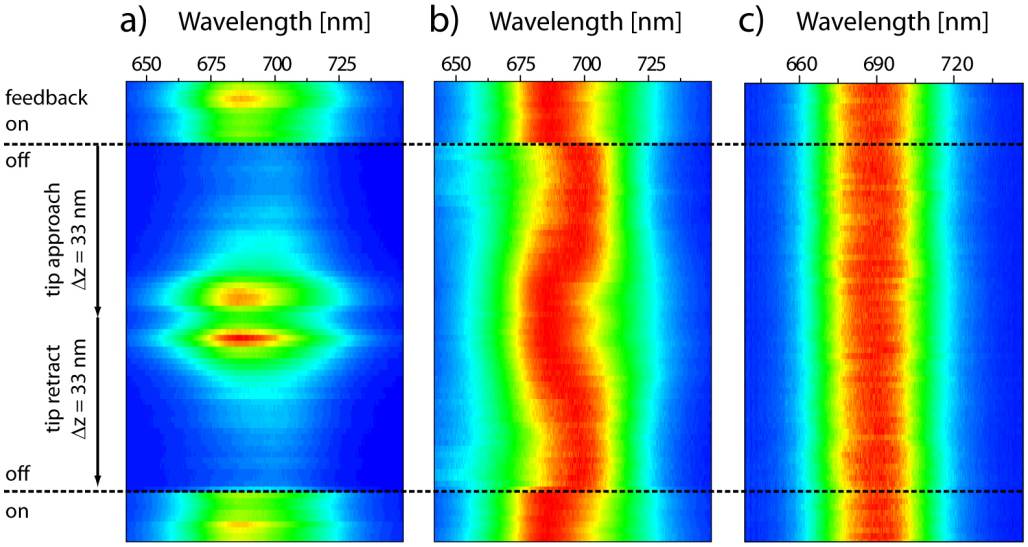

Figure 7.2: Series of spectra recorded for single CdSe nanowires during approaching and retracting a gold tip by about 33 nm. The acquisition time was 0.5 s per spectrum. a) The PL signal shows a short ranged increase due to the near-field enhancement provided by the tip. Competition of enhancement and quenching by the metal probe results in a decreasing intensity for very short distances. b) Same spectral series with each spectrum normalized for better comparison illustrates a blue-shift of the PL emission for small tip-sample distances. c) Normalized spectra series from another nanowire and tip showing no spectral shifts despite near-field enhancement.

position, it was instantly pulled back by about 27.5 nm, which resulted in a sudden decrease of the intensity. In the example this is indicated by the upper dotted line on the left side of the spectra. While the acquisition of spectra continued, the probe was then slowly approached to the sample surface, that means the distance was reduced constantly to a separation even closer than at the setpoint position. This region of the plot is indicated by the upper arrow. Here, the intensity increases rapidly within the last few nanometers confirming the near-field nature of the interaction. For the smallest distances, the PL intensity drops again because of quenching by the metal probe. The recording of the tip-sample distance dependence of the PL signal is repeated for the other direction as the tip is slowly retracted again reproducing the same results. Finally, the probe was returned to the setpoint position to complete the measurement.

In figure 7.2 b, the same spectral series is shown, this time the intensity of each spectrum has been normalized for better comparison. Apparently, the emission shifts to shorter wavelengths by about 8 nm for decreasing tip-sample distances and higher enhancement. While similar energy shifts have been observed for other CdSe nanowires and tips, also cases without any spectral variation occurred. Such an example without a spectral shift is shown in figure 7.2 c. In this case the spectrum did not change when the tip was approached and induced strong signal enhancement.

There are two possible reasons for this occasionally observed spectral shifts. First, the different size of the detected near-field and far-field areas may contain varying sample compositions. Irregularities regarding variations in the crystal structure, the diameter or changes in the surrounding of the nanowire could result in the observed differing emission energies, when averaging of the detected signal from far-field and near-field foci comprise different contributions. However, what kind of irregularities are involved in the particular case can not be deduced from the present measurements. Second, the signal enhancement due to the near-field probe is likely to dependent on the wavelength. It is strongest when the frequency of the photons matches the plasmon resonance, which in turn depends on the specific tip geometry. This would lead to spectrally altered emission depending on the optical properties of the respective gold tip, emphasizing spectral regions of strongest enhancement. Due to the complex nature of the investigated system these effects cannot be distinguish in the present case. Since varying energy shifts have been observed with the same tip at different sample positions the optical properties of the tip antenna can not be the only reason.

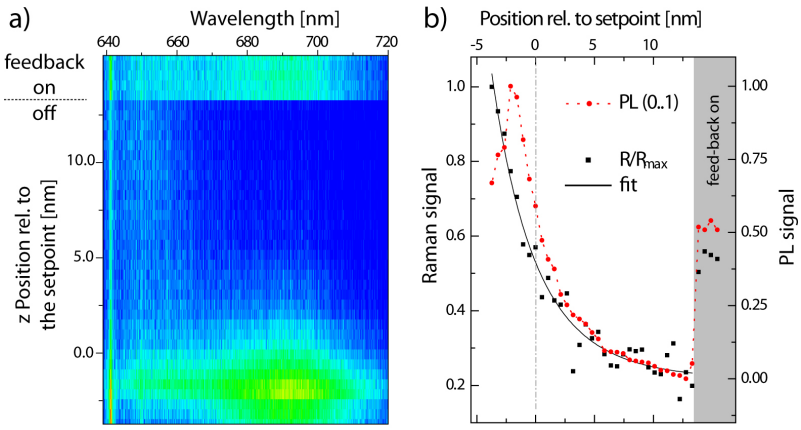

Figure 7.3: a) Series of spectra including Raman and PL signals recorded for a single CdSe NW during approaching a gold tip. b) Approach curves for the Raman signal (black squares) and PL signal (red circles) extracted from the spectra in (a). While the Raman signal increases continuously, the PL intensity decreases for very short distances due to metal-induced quenching. The Raman enhancement can be described by equation 3.24 (solid black line).

In figure 7.3 a, another example measurement obtained by the same approach procedure is depicted. For this CdSe nanowire, both Raman scattering and emission of photoluminescence were observed. Owing to the absence of any spectral shift, approach curves could be extracted by plotting the maximum intensity against the tip-sample distance. The resulting approach curves are depicted in figure 7.3 b. In the case of the Raman signal the intensity was normalized to the maximum Raman intensity, the model introduced by Cançado et al. can then be tested for CdSe nanowires [93]. In that model it is assumed that near-field and far-field contributions are always intermixed and that the relative intensity of the Raman signal is given by the sum of both, i.e. $R/R_{max} = (R_{ff} + R_{nf})/R_{max}$. The

model predicts that the signal enhancement due to the gold tip is inversely proportional to the 10th power of the tip-sample distance d according to

$$\frac{R(d)}{R_{max}} = \frac{1}{M} + \frac{C}{(d + r_{tip})^{10}}. \tag{7.1}$$

Here $R(d)/R_{max}$ denotes the distance dependence of the Raman signal normalized to its maximum, M is the maximum signal enhancement factor given by $\mathrm{R}_{max}/\mathrm{R}_{ff}$, C is a constant and r_{tip} the radius of the tip.

The experimental Raman data was fitted using equation 7.1, the resulting curve is plotted as solid black line in figure 7.3 b. The fitting parameters obtained were $M = 4.7$, $C = 3.9 \cdot 10^{15}\,\mathrm{nm}^{10}$ and $r_{tip} = 40\,\mathrm{nm}$, comparable to the values found for SWCNTs in the literature [93]. The distance dependence of the Raman signal (black squares) is found to be well described by the fitted curve. While the model was originally developed to describe coherent Raman scattering in SWCNTs, the good agreement between the experimental data and the fitted curve in figure 7.3 b suggests that it can also be applied to single CdSe nanowires. The radius of the tip r_{tip} obtained by the fit is larger than estimated from the resolution in near-field measurements ($r_{tip} = 25\,\mathrm{nm}$). This discrepancy is attributed to the point dipole model, i.e. the placement of a dipole at the center of a metal sphere of radius r_{tip}. A more accurate description of the tip fields requires a shift of the position of the dipole in direction of the tip axis [93]. It has to be mentioned that the Raman data in figure 7.3 b could also be modelled by the slightly steeper curve proportional to $(d + r_{tip})^{-11}$ which is expected for the case of incoherent scatterers. The small difference between the two dependencies cannot be distinguished in the present data.

Based on the force between tip and sample observed by the shear-force feedback control system, it was estimated that the tip would have touched the surface at position -5 nm in figure 7.3. Thus, quenching of photoluminescence dominates over enhancement only for very small tip-sample separations up to about 3 nm, corresponding to the peak PL intensity at position -2 nm in figure 7.3. This distance is somewhat shorter than the 5 nm reported for fluorescent dye molecules [97]. The enhancement efficiency for PL is expected to depend strongly on the intrinsic quantum yield of the emitter in the absence of the tip Q^0. For highly fluorescent dye molecules with Q^0 close to unity, the radiative rate enhancement provided by the tip would not be able to increase this value further, in contrast to low quantum yield emitters like the CdSe nanowires. TENOM is thus more efficient for low quantum yield emitters. At the same time, the distance at which the maximum enhancement is achieved is expected to shift to smaller values upon decreasing Q^0 [101]. In other words even smaller distances correlated with higher enhancement can be applied to low quantum yield emitters before quenching outweighs the signal enhancement.

In general, for 1D nanostructures like CdSe nanowires and also SWCNT, the mobility of the excited state needs to be considered as well. The exciton mobility has two significant effects. First, mobile states excited at the tip apex are able to leave the region of tip-enhanced fields escaping from enhanced decay rates. Second, excitons created besides the

tip apex (due to the diffraction limited excitation laser spot) can enter this interaction region. For low quantum yield systems a high exciton mobility leads to a reduced enhancement of the PL signal since the first effect dominates [39]. These findings complicate the quantitative description of the photoluminescence enhancement enormously [24].

The following section presents the investigations of the angular distribution of the PL emission and the influence of the near-field probe on the radiation pattern. For that purpose, the radiation pattern of photoluminescence from nanowires without the tip has been characterized first. In the second step, changes therein when approaching a near-field probe have been studied.

7.2 Angular emission of CdSe nanowires

The CdSe nanowires can be described as quasi 1D structures as long as their diameter is small enough, i.e. when it is smaller than twice the exciton Bohr radius. According to a classical treatment and using the dipole approximation, the radiation pattern is expected to resemble the pattern of a point dipole as shown in chapter 3.4. This dipole should be oriented along the nanowire axis ($\vec{\mu} \parallel c$) as expected from theory, because of the valence band crossing and dielectric mismatch effects (see chapter 2.2) [64,71]. Polarization dependent excitation and emission experiments support this idea [137,138]. On the other hand the finite size of the investigated CdSe nanowires with diameters in the range of about 4-24 nm and lengths of up to several microns suggests that the predictions of the angular emission by the single point dipole picture might be insufficient. Compared to the thin and hollow SWCNTs, where such a description was very accurate (see chapter 5), the CdSe nanowires might be less well described by the 1D picture. If this is the case, major deviations from the calculated pattern are expected and a more complex theoretical treatment will be necessary to model the angular emission.

Back focal plane imaging of the photoluminescence emission from CdSe nanowires was used to investigate the angular emission properties. A comparison of experimental and calculated dipole patterns reveals similarities and discrepancies between the physical system and the theoretical treatment. It will be shown that the description with a single point dipole is in fact insufficient, however, the addition of a second in-plane radiating dipole oriented orthogonally turns out to result in a good agreement of calculation and experiment. Therefore the dipole approximation within a classical treatment is still applicable to the physical system.

7.2.1 Experimental radiation patterns

To measure the radiation patterns of CdSe nanowires they were first localized via APD imaging. A selected nanowire was then positioned in the focus and the BFP imaged onto

a CCD chip by using a Bertrand lens. The experimental description can be found in chapter 4. For excitation the red HeNe laser was used with the output mode converted into a radial doughnut mode. A typical example of such a radiation pattern is shown in figure 7.4.

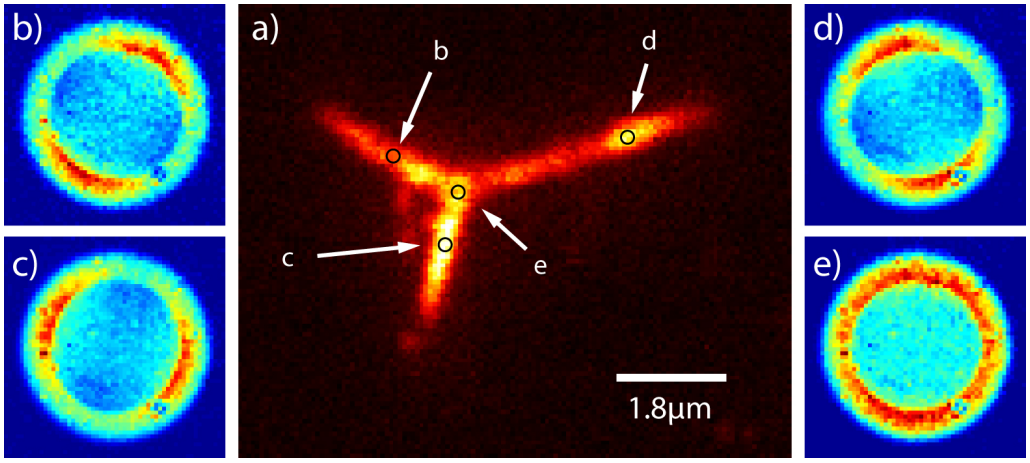

Figure 7.4: a) Confocal PL image of a CdSe nanostructure consisting of a tripod shaped nanowire with additional small nanowires bundled to the arms. b-d) Radiation patterns measured at the three arms of the nanostructure and in its central region as marked in (a). The intensity distributions in the patterns b-d show that the emission is similar to dipolar emission from which the orientation of the transition dipole can be determined to coincide with the nanowire axis. The three patterns overlap in the center of the structure resulting in the radially symmetric pattern shown in (e).

In this measurement a band pass filter with a center wavelength of 660 nm and a spectral width of 20 nm has been used to select emission from thin nanowires that show a blue shifted PL energy due to quantum confinement. The diameter of the observed nanowires is estimated to be about 5-10 nm. PL from thicker nanowires appears on the lower energy side of the spectral window and is thus not detected. A branched nanowire leads to the star like form that can be seen in the PL image in figure 7.4 a. The three arms of the structure consist of few thin nanowires bundled together as known from shear-force AFM measurements.

Radiation pattern from this nanostructure have been measured at four different positions as marked in figure 7.4 a. Three patterns were taken at the arms of the structure and the fourth one from its central region. The observed radiation patterns are shown in (b-e). The patterns measured at the arms feature two opposite lobes of maximum intensity in the outer region, beyond the critical angle. In the inner region there are two opposite minima. This intensity distribution reveals strong emission perpendicular to the nanowire axis, that is apparent in the APD image.

The radiation pattern acquired in the central region of the nanostructure, which is shown in figure 7.4 e, features a different intensity distribution that looks rather uniform in all directions. In the inner part of the pattern, for angles smaller than the critical angle, the

intensity is quite uniform. This radiation pattern results from an overlay of the other three patterns, from which the intensity adds up to a nearly radially symmetric distribution. In contrast to the emission from a vertical dipole (see figure 3.6 b) it exhibits some intensity even at very small angles, i.e. the center of the pattern.

7.2.2 Modelling the radiation pattern by two orthogonal point dipoles

To figure out whether the description of an emitting CdSe nanowire by a single point dipole results is adequate, theoretical and experimental data sets have been compared by fitting the experimental pattern with the respective theoretical distribution. In a first step the normalized pattern of a single dipole has been used to reproduce the measured data with the orientation angle Φ as the only fit parameter. Afterwards the amplitude was varied to match the originally measured radiation pattern. A representative set of data is shown in figure 7.5. The corresponding nanowire had a diameter of about 15 nm.

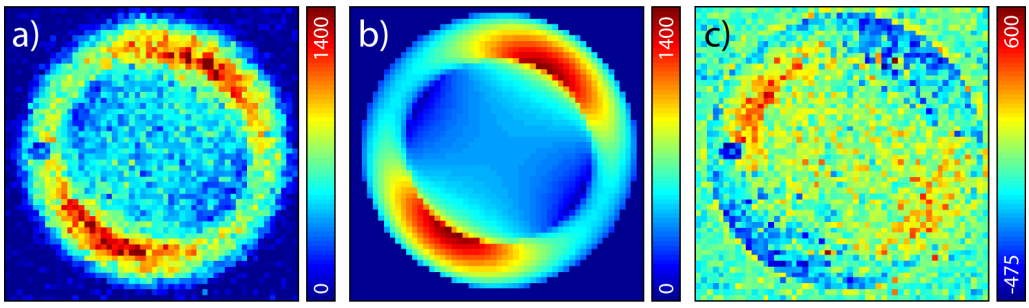

Figure 7.5: a) Experimental radiation pattern of a 15 nm thin CdSe nanowire. b) Theoretically calculated dipole pattern. The orientation and the amplitude have been fitted to match the experimental pattern in (a). The model is found to be sufficient for an estimation of the nanowire orientation. c) The difference of experimental and fitted pattern (residual), however, reveals that one dipole is not sufficient to reproduce the experimental data convincingly.

The measured pattern depicted in (a) was fitted by the calculated pattern shown in (b). The intensity distributions partially agree well, the two lobes with maximum intensity in the outer region and the two minima in the inner region coincide and allow for the estimation of the orientation of the transition dipole along the nanowire. The residual, which is depicted in figure 7.5 c, however, reveals also major systematic deviations between the two patterns. The most obvious deviations occur in the outer region, where the bright parts of the calculated pattern are too intense (blue in figure 7.5 c) and the weak parts are too dark (red in the residual). But also the inner region of the fitted pattern is considerably darker than that of the measured pattern (yellow in the residual). The dark blue spot on the left side of the measured pattern presumably results from some dirt on a spectral filter in the detection beam path.

These findings discussed so far clearly show that the description of the photoluminescence emission from CdSe nanowires with a single in-plane point dipole is insufficient. Therefore, the model has to be extended further in order to provide an accurate description of the angular emission. Owing to the quasi 1D nanowire structure many point dipoles along the nanowire might radiate coherently leading to a different radiation pattern. However, the resulting pattern would feature sharper maxima and minima and thus provide an even worse description of the experimental data [139]. Another consideration seems to be more likely, keeping in mind the rather large dimensions of the nanowires and taking into account possible consequences. Since the nanowires have a diameter in the range of or even larger than twice the exciton Bohr radius it appears to be acceptable to relax the restrictions that arise from a purely one dimensional treatment. Thus additional transition dipoles with orientations differing from the nanowire axis will also contribute to the radiation pattern.

In order to test this hypothesis the fit routine has been extended to consider two independent dipoles radiating incoherently in the next step. The main dipole was assumed to be oriented as estimated from the fit with only one radiating dipole, thus it is assumed to be in-plane and its orientation angle Φ_1 was kept constant. A second dipole perpendicular to the first dipole was then added. The orientation of this second dipole can be (i) in-plane or (ii) parallel to the optical axis of the microscope. In the first case Φ_2 would equal $\Phi_1 + 90°$, that means also the second dipole is oriented horizontally. In the second case the dipole would be oriented vertically with $\Theta = 0°$. For both cases (i) and (ii) the parameter that have been varied to fit the experimental data have been the amplitudes of the two calculated patterns. The fitting results for the experimental pattern from figure 7.5 a are presented in figure 7.6.

The upper row (a-c) shows the fitting results for the additional radiating dipole oriented vertically, the lower row (d-f) for a horizontally oriented one. The radiation pattern of the additional dipole is shown in the first column (a, d), they are consistent with the pattern shown in figure 3.6. The calculated patterns, resulting from fitting those double dipole patterns are presented in the middle column (b, e) and the differences of measured and fitted patterns are depicted in the right column (c, f). It can be seen that a fit using a single horizontally and one vertically oriented dipole (upper row) is not able to remove the deviations compared to the fit with only one dipole (figure 7.5 c), even though they are decreased. On the other hand, if the second dipole is also oriented horizontally but rotated by 90 ° (lower row), the resulting fit-pattern matches the experimental data quite well as can be seen from the now radially symmetric residual (figure 7.6 f). The amplitude of the second dipole is found to be a quarter of the amplitude of the first dipole. The main deviation visible in the residual now originates from the dark spot in the experimental data, which is due to the optical system. The differences at the outer rim of the patterns are presumably caused by a significant attenuation of the marginal rays, leading to a smaller effective numerical aperture of the objective. At very high angles, this would result in an

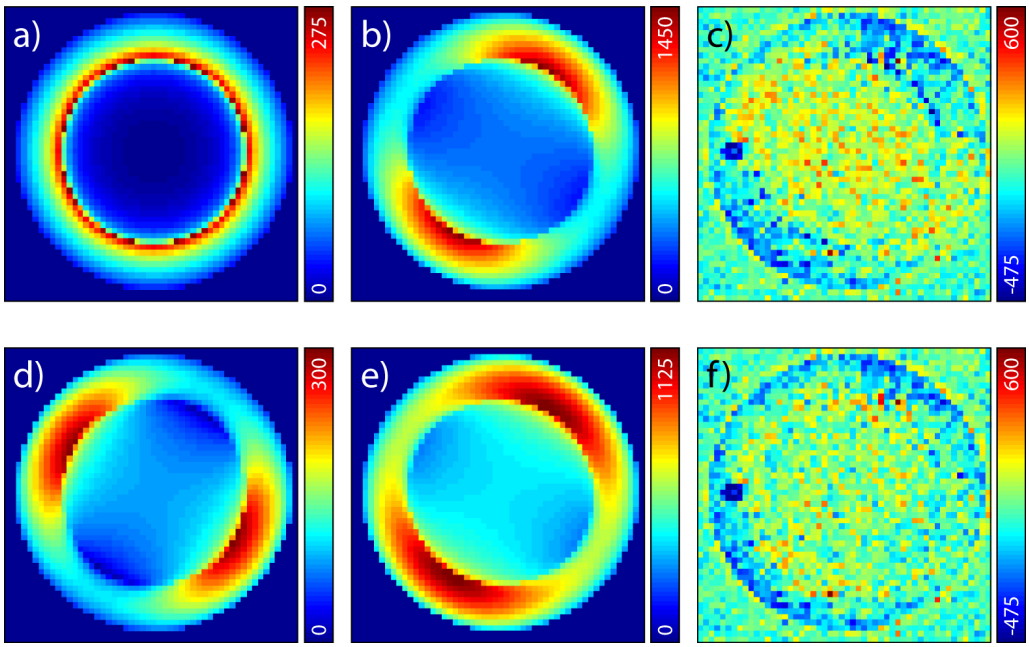

Figure 7.6: The experimental pattern from figure 7.5 fitted by two additive patterns with the corresponding dipoles oriented orthogonally to each other. a) Radiation pattern of a vertical dipole. b) Fitted pattern consisting of the horizontal and an additional vertical component, for each the amplitude has been varied to optimize the fit. c) The still low agreement of experimental and fitted pattern is revealed in the residual. d) Pattern of a second horizontal dipole (orthogonal to the first one). e) Fitted pattern consisting of two horizontal components, again the amplitude of both has been varied to optimize the fit. f) The remaining difference is spatially uniform revealing a much better agreement with the measured pattern depicted in figure 7.5 a. Deviations mainly originate from a discrepancy of the size of the measured and the fitted pattern.

overrated intensity in the calculated radiation pattern, leading to the negative contrast in the residual [140].

It is further found that adding a third radiating dipole to the fitting procedure with all dipoles oriented orthogonal to each other does not significantly improve the similarity of experimental and calculated pattern. The amplitude of such a third dipole pattern would be very small compared to those of the other dipoles and is therefore negligible.

The findings presented above lead to the conclusion that within the dipole approximation, the system is best described by two radiating in-plane dipoles that are oriented orthogonally with respect to each other. This is rather surprising since on the first sight both orientations perpendicular to the nanowire axis, whether horizontal or vertical, would be expected to emit photoluminescence equally. However, from literature it is known that the radiative rate of an emitter is decreased if it is placed at an interface, because the lifetime of the excited state is increased [141, 142]. The lifetime and the radiative rate were found to depend on the dipole orientation with respect to the interface, and the lifetime of a vertically oriented dipole to be about 2-3 times larger than that of a horizontally

oriented one. As a consequence the quantum yield of a horizontal dipole is expected to be significantly higher, because the quantum yield is proportional to the corresponding radiative rate. This effect explains the observations on the CdSe nanowires in which signal emitted from a vertical transition dipole can be neglected while it is important to take a second horizontally oriented dipole into account when fitting the intensity distribution of the radiation pattern.

7.2.3 Independence of the angular emission from the focus position

For the further investigations, it is highly important whether the intensity distribution depends on the position of the nanowire with respect to the focus or not. Assuming that the polarization of the emission is independent from the polarization of the excitation fields, the intensity distribution of the radiation pattern should always be the same, despite the different polarizations within the focus of a radially polarized doughnut mode. To address this question a single CdSe nanowire was scanned through the focus and the corresponding radiation patterns were measured at different positions. The photoluminescence image of a bright CdSe nanowire with a diameter of about 15 nm is shown in figure 7.7 a. The very bright signal in the bottom right area belongs to a bundle of several nanowires. The radiation pattern corresponding to the single NW, that was taken while the nanowire was centered correctly in the focus, is depicted in (b). It shows the typical dipolar intensity distribution. For both experiments a long pass filter with a cutoff wavelength of 700 nm has been used.

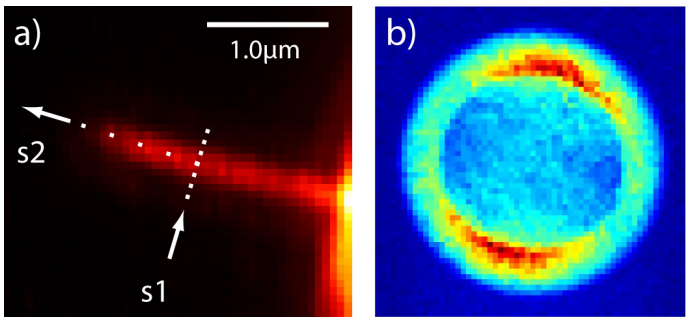

Figure 7.7: a) PL image of a single 15 nm thick CdSe nanowire. The corresponding radiation patterns detected while the NW was correctly centered in the focus is depicted in (b). Indicated in (a) are the positions along the paths s1 and s2, where radiation patterns have been acquired later on (see figures 7.8 and 7.9).

Two series of patterns were then acquired while the position of the nanowire relative to the focus was successively changed along the paths denoted s1 and s2 in figure 7.7 a: The first path runs across the NW axis, the second one along the nanowire and beyond it. The observed patterns are shown in the figures 7.8 and 7.9. For s1 and s2 the distance between two acquisition spots was 100 nm and 200 nm, respectively.

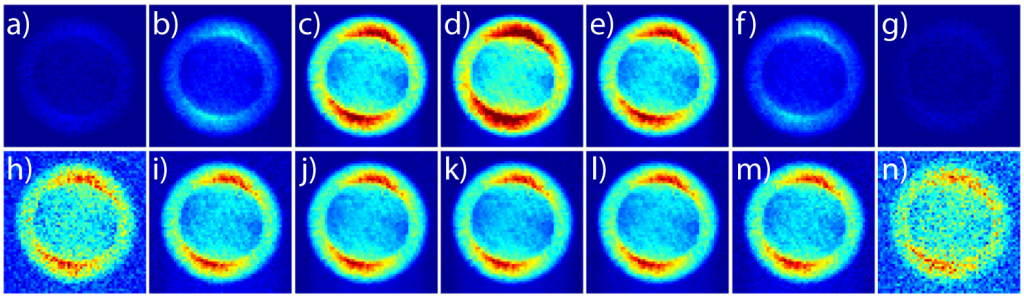

Figure 7.8: Radiation patterns taken along path s1 in figure 7.7 a across the nanowire. a-g) Patterns scaled to the maximum of the most intense pattern in (d). h-n) Same patterns as in the upper row but with normalized intensity. The intensity distribution does not show any changes, only the intensity varies and is highest when the nanowire is positioned in the center of the focus. The displacement between two positions of pattern acquisition is 100 nm.

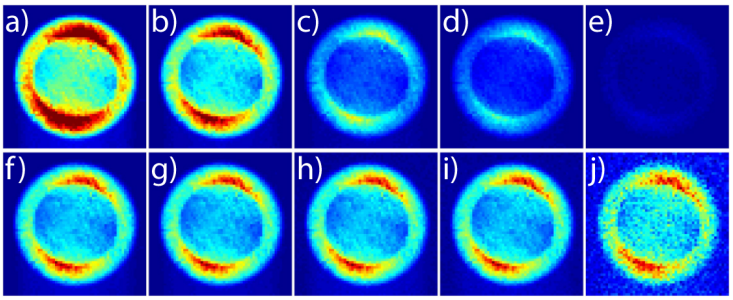

Figure 7.9: a) Radiation patterns taken along path s2 in figure 7.7 a along the nanowire. a-e) Patterns scaled to the maximum of the most intense pattern in (a). f-j) Same patterns as in the upper row but with normalized intensity. The intensity distribution does not show any changes, only the intensity varies and it becomes weaker as the nanowire leaves the focus. The displacement between two positions of pattern acquisition is 200 nm.

As expected the signal intensity in the radiation pattern strongly depends on the position of the nanowire with respect to the focus. The highest intensity and thus the best signal-to-noise ratio is observed when the nanowire is accurately positioned in the center of the focal spot, where the excitation intensity is highest. This is the case in figure 7.8 d and in figure 7.9 a. Already at a distance of 500 nm from the nanowire, the radiation pattern is no longer observable at these particular experimental conditions, reflecting the tight focusing achieved with a NA = 1.49 objective.

However, the radiation pattern does not show any variations in the intensity distribution, neither in figure 7.8 nor in figure 7.9. This can be clearly seen in the lower rows of the two figures were the normalized radiation patterns are depicted. Again only the signal-to-noise is clearly reduced as the nanowire leaves the focal spot. The pattern is always highly symmetric even if the position of the nanowire is slightly of the center of the focal spot. According to these findings the intensity distribution in the radiation pattern is stable for a nanowire positioned within the experimental position accuracy, because the

imaging properties of the optical system with respect to the intensity distribution in the radiation pattern show no observable dependence on the lateral position of the emitter. Also minor sample drifts will not change the intensity distribution, even though they may add to slight fluctuations of the intensity.

The laser mode which has been used to excite the nanowire results in areas of different polarizations of the optical fields in the focal spot. Since the intensity distribution of the radiation pattern does not change when scanning through the focus, the emission process is independent of the excitation polarization for PL emission from CdSe nanowires.

7.3 Influence of a NF probe on the angular emission

When the sharp gold tip used in TENOM experiments is brought into close proximity of the CdSe nanowire, the integrated PL intensity will increase because of enhanced excitation and radiative rates. In addition, the radiation pattern is expected to change its intensity distribution since radiative rate enhancement is connected to a spatial redistribution of the emitted signal [143]. A result from the previous section was that emission from CdSe nanowires cannot be described by only one emitting dipole, as it was the case for SWCNTs. It rather turned out that a second in-plane dipole has to be taken into account, while the vertical component can be neglected. However, this vertical dipole matches the orientation of the tip dipole, thus it is expected to gain importance when interaction with the tip takes place. Therefore a strong ring shaped component in the radiation pattern corresponding to a vertical dipole is expected.

Figure 7.10 shows a series of radiation patterns that has been acquired during the approach of a near-field probe. In contrast to earlier presented distance-dependent measurements, the feedback loop was not switched of here, because the acquisition time per pattern is much higher than per spectrum. During the long measurement in the case of pattern acquisition, small vertical drifts of the sample and the tip would surely damage the tip. Therefore, a series of radiation pattern was measured while the tip was approach under control of the feedback loop. The CdSe nanowire is the same as in figures 7.7, 7.8 and 7.9. Its diameter was about 15 nm which is larger than twice the Bohr radius of an exciton in CdSe, thus no significant blue shift due to quantum confinement is observed. For the measurement, a 700 nm long pass filter was used. Acquisition of series of radiation patterns was possible since the bright nanowire allows for short acquisition times of 1 s per radiation pattern. The time that is needed for the acquisition of one pattern is nevertheless still long compared to the approach speed of the tip, which is roughly 300 nm/s. The feedback loop decreases the approach speed only within the last few nanometers when the tip reacts to the shear forces between tip and sample. Each pattern thus represents an average over a rather large tip-sample-distance range. Since the near-field enhancement occurs within only the last few nanometers the changes in the radiation patterns are expected

to occur within the acquisition of only one pattern. The first patterns before will not be influenced by the tip, while the last patterns are measured with the tip held constantly in its final feedback position. Preliminarily to the pattern measurements the signal enhancing character of the tip was confirmed by acquiring a conventional TENOM PL image. The signal enhancement was found to be moderate.

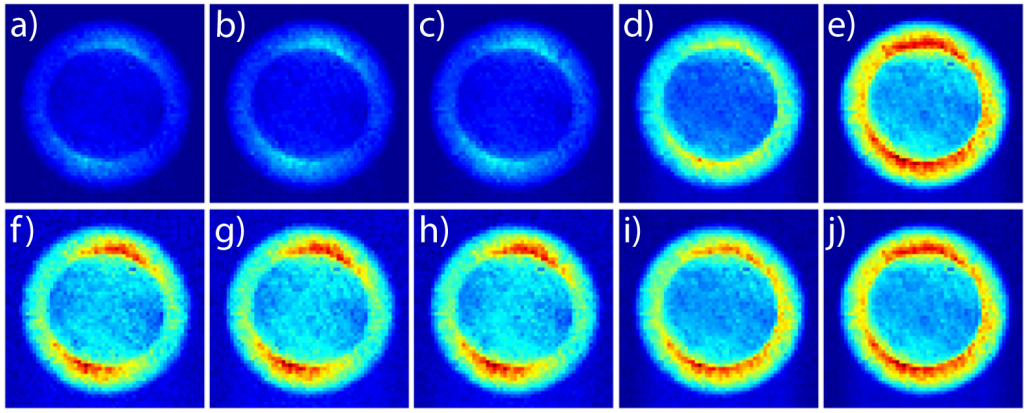

Figure 7.10: a) Series of radiation patterns measured during the approach of a gold tip. a-e) Patterns scaled to the maximum of the brightest one. Strong signal enhancement induced by the approached tip can be seen. f-j) In the normalized radiation patterns the redistribution of the intensity is revealed which leads to a more ring like pattern in (j) (tip in close vicinity) as compared to the radiation pattern in (f) (tip far away).

Both rows of figure 7.10 show the same series of radiation patterns that have been acquired during the approach of the near-field probe. The patterns in the upper row are scaled according to maximum and minimum intensity of the brightest pattern, which is the one shown in (e). In the lower row all patterns are normalized for a better comparison of their intensity distributions. The images shown in (a) and (f) represent the radiation patterns in the absence of the near-field probe and are consequently equal to the one shown in figure 7.7 b. The pattern in (j) on the other hand is measured while the tip was at its smallest distance to the nanowire. The pattern depicted in (g) represents an time average over radiation without and with near-field interaction while the tip reached the interaction range.

The first observation is that the overall intensity increases significantly when the tip is approached. The integrated intensity of the pattern in (e) is about 4 times higher than that in (a), which is consistent with the observed moderate enhancement in preliminarily TENOM measurements. In the series shown here one intermediate radiation pattern has been observed which is shown in (d). During the acquisition of this pattern the tip reached its final position with constant distance to the nanowire, the pattern thus shows an average of the pattern in the absence of the tip and the pattern in the presence of the tip as well as possibly occurring intermediate patterns.

The second observation refers to the intensity distribution of the radiation patterns which can be easily compared within the lower row of figure 7.10. The radiation pattern in (f) shows the typical nanowire pattern with two lobes of maximum intensity at higher emission angles. In contrast to this, the pattern influenced by near-field interaction between nanowire and tip (figure 7.10 e and j) reveals a strong ring shaped component in addition to the two lobe pattern. The inner region of the pattern also changed towards relatively lower intensity in the central region. That means that in fact the spatial emission has been altered due to the presence of the near-field probe.

The findings presented above are explained as follows. Regarding the excitation process, the enhanced electrical fields at the tip apex lead to a higher excitation rate k_{ex}. Since the emission process is independent from the excitation, as shown earlier by the far-field experiments in section 7.2.3, this does not alter the intensity distribution of the radiation pattern, but it will contribute to the overall signal enhancement. The presence of the gold tip adds a new emission channel in which energy is transferred to the tip before it is emitted by the antenna dipole, whereby also the radiative rate k_{rad} is enhanced. The vertical dipole in the nanowire, that has been neglected before, now becomes important. Since it is oriented parallel to the tip dipole, interaction of these two is highly efficient. This enables the tip to extract energy from the nanowire, which is then radiated by the tip dipole, giving rise to the ring-shaped component in the radiation pattern in figure 7.10 e.

It has to be mentioned that the photoluminescence from the gold tip itself also falls into the spectral detection window as can be seen in the spectrum of a typical gold tip in figure 5.6. A radiation pattern with the tip approached to the plain substrate surface was thus acquired without any nanowire. Under the same experimental conditions no tip signal was observable. A 30-fold increase of the integration time up to 30 s resulted in a very weak and noisy signal. Only a 10 times higher laser excitation power resulted in a measurable radiation pattern. Thus any contribution through photoluminescence of the tip to the nanowire PL radiation pattern can be neglected at the experimental conditions applied during the investigations on CdSe nanowires presented above.

Asymmetry in the radiation pattern induced by the gold tip

Radiation patterns of nanowire PL measured in the presence of a gold tip often show strong asymmetries in their intensity distribution. This asymmetries are never observed in the absence of the tip, which can be seen for example in the confocal investigations shown earlier (figures 7.4 7.8 and 7.9). The observed asymmetries further vary from tip to tip, some result in rather symmetric patterns while others lead to a significant amount of asymmetry in the patterns. They must thus be related to the individual tip characteristics and its influence on the angular emission of the CdSe nanowires. Furthermore, the intensity distribution becomes asymmetric when the tip is moved in the sample plane, even if the pattern from a coupled tip-nanowire pair is symmetric in the case of accurate alignment.

Owing to the fact that photoluminescence from nanowires can be emitted via dipoles of different orientations despite its quasi 1D structure, a non-ideal alignment between tip and nanowire might result in asymmetric angular emission. From literature it is known that emitters of all orientations can be coupled to a metal nanoantenna [110] and that the emission of a single molecule is redirected towards this metal object [109, 114]. The angular emission is thus expected to depend strongly on the relative positions of the tip with respect to the nanowire and consequently also asymmetric radiation patterns should occur.

In figure 7.11 this dependence on the relative position of the tip is shown for a coupled tip-nanowire system. As the tip is displaced slightly from the optical axis by a vertical movement, the radiation pattern gets strongly asymmetric even though the signal intensity is still comparable. Since horizontal as well as vertical dipoles feature highly symmetric radiation patterns, this indicates the presence of a radiating dipole with $0 < \Theta < 90°$.

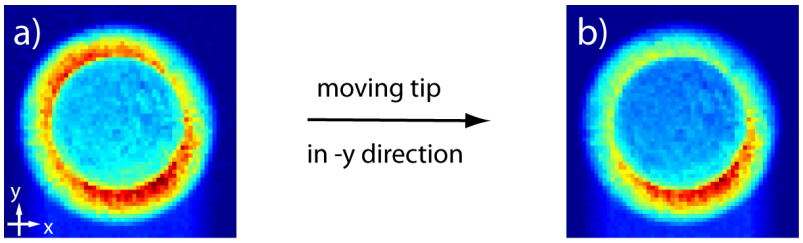

Figure 7.11: a) Moving the tip with respect to the nanowire position (and thus to the optical axis of the microscope) alters the radiation pattern, which becomes highly asymmetric.

Besides a misalignment of the coupled tip-sample system, the tip itself might be the reason for asymmetric radiation patterns if it features a non ideal tip shape. In addition, a dependence of the emission pattern of the tip on the lateral position (with respect to the optical axis) needs to be checked. To address this issues, the radiation pattern of a gold tip's photoluminescence has been measured at different positions in and around the focus. A representative set of data is shown in figure 7.12.

The radiation pattern in figure 7.12 c has been measured as the tip was centered accurately in the focus. It already shows an asymmetric intensity distribution with a non uniform ring at higher emission angles. At very small angles, where no intensity would be expected for a fully axially oriented dipole, at least some intensity is observed. Both findings results from a non-ideal geometry of the tip which leads to off-axially oriented dipole components despite the strong longitudinal polarization of the excitation field in the middle of the focus of the radial doughnut mode.

Figure 7.12 a-e shows a series of patterns of tip PL at five different positions along the x-direction. Starting from the middle pattern the tip was moved into the -x (+x) direction, the corresponding patterns are shown on the left (right) side in (b) and (a) (in (d) and (e)). For the other patterns in (f-i), the tip was moved along the y-axis. Obviously, the

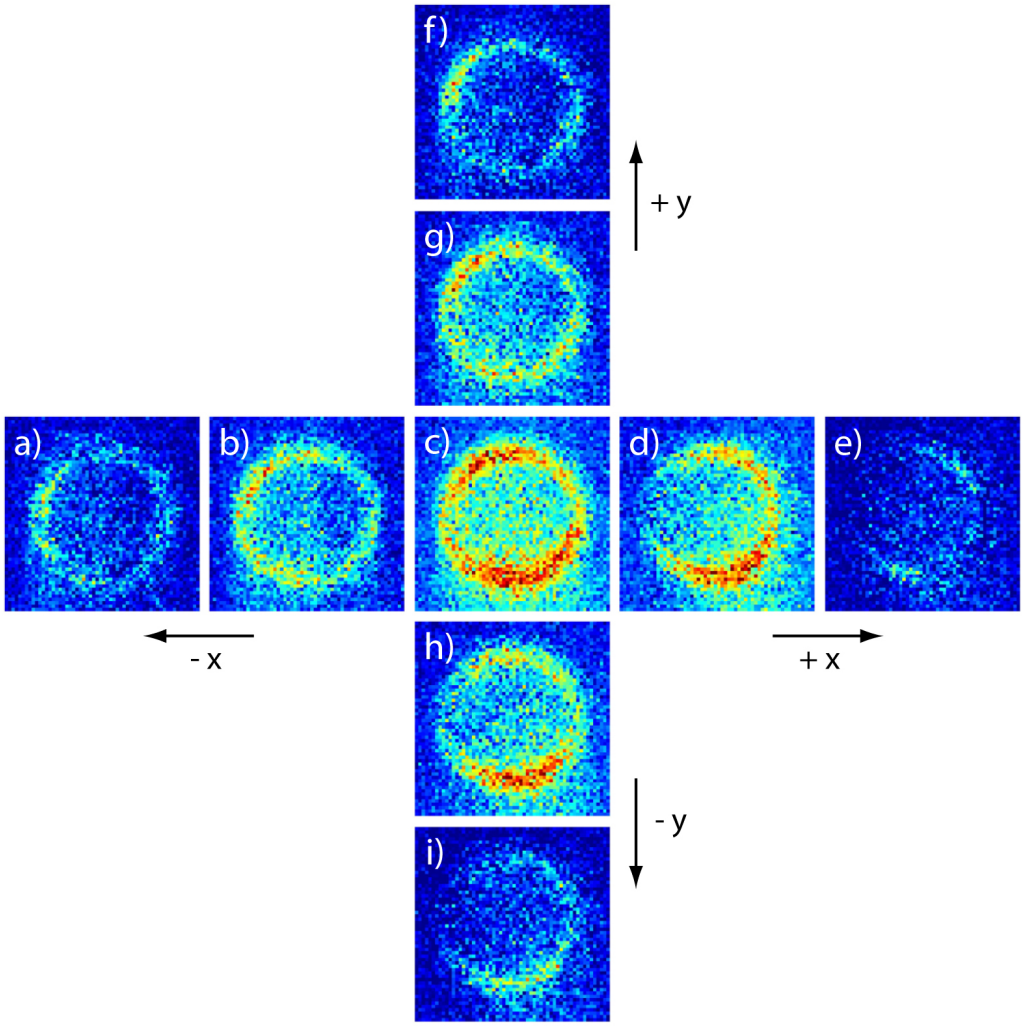

Figure 7.12: Series of radiation patterns of the PL from a gold tip that was positioned at different distances from the focus in x and y direction (in-plane movement). The patterns reveal asymmetries of the intensity distribution that depend on the position of the tip with respect to the focus. c and h) Even though the tip has been centered in the focus there is some asymmetry in the patterns.

radiation pattern of the tip emission changes with its position relative to the focus. When the tip is moved towards one direction also the intensity in the pattern concentrates on that pattern side. The exact intensity distribution also depends on the asymmetry of the tip, which visible in the accurately centered position (patterns c). When the tip leaves the focal spot the PL signal fades away resulting in the lower overall intensity of the pattern that were taken farthest away from the center.

The origin of the asymmetric radiation patterns from gold tip photoluminescence, even if it is positioned accurately, has been identified as follows. Every tip has its individual geometry that may result in a non-perfectly ring shaped pattern. As a consequence the approximation that the perpendicular component of the polarizability can be neglected with respect to the parallel component does not hold unrestrictedly for the used gold

tips. That means that $\alpha_{\parallel} \gg \alpha_{\perp}$ cannot be assumed generally for all tips. It has to be considered, that in the TENOM experiments on CdSe nanowires the pretty soft gold tips were scanned over features of up to for example 60 nm in the case of small bundles. While scanning over such relatively thick features the tip shape might change and usually looses it original geometry. This was especially found to be the case when the tip was moved manually while positioning it on a nanowire for the acquisition of radiation patterns. The tip PL pattern in figure 7.12, for example, were taken after experiments on nanowires which is likely be the reason for its non perfect radial symmetry.

The presented observations further show that the intensity distribution depends on the position of the tip with respect to the optical axis, i.e. its lateral position. Since this effect was not observed for SWCNTs nor CdSe nanowires, it is not induced by an aberration of the optical system. The dependence of the radiation pattern from the lateral position must thus be related to the excitation process within the focus, where the polarization is longitudinal in the center and lateral in a ring around the central region [144]. Consequently, the emission of luminescence depends on the polarization of the excitation fields in the case of such a gold tip.

Therefore, the accurate positioning of the tip and the investigated nanowire is highly important to prevent asymmetries in the intensity distribution induced by off axis alignment of the coupled system in TENOM experiments. On the other hand, the tip in its function of an optical antenna can be regarded as a tool to control and direct the spatial distribution of the emission. Well designed metal tips could be used to drastically increase the directivity of the radiated emission towards the detector, as has already been shown for single molecules coupled to optical antennas [107, 109]. As a consequence the detection sensitivity of the system would significantly increase.

Conclusion

In this chapter, the influence of a gold tip on the spectral and angular emission characteristics of CdSe nanowires has been investigated. Near-field enhancement of the signal within only few nanometers is in some cases connected to spectral shifts of the PL signal. Different reasons could be identified including irregularities in and outside the nanowire and a spectrally dependent signal enhancement by the tip, but they cannot be distinguished here. Consequently, high-resolution TENOM imaging requires a careful data analysis and interpretation, in particular regarding energy variations of the observed signal. The equation derived for the tip-sample distance dependence of Raman scattering from SWCNTs was found to describe the experimental findings on CdSe nanowires quite well, which shows that the model can be also applied to inorganic semiconducting quasi 1D nanostructures.

The radiation pattern of CdSe photoluminescence appears to be similar to the radiation pattern of a single point dipole, and the estimation of the nanowire orientation exploiting

this description provides good results. However, to reproduce the intensity distribution of the pattern quantitatively, a second dipole was found to be necessary for a satisfying agreement between measurement and calculation. Signal enhancement due to the presence of the gold tip was found to be always accompanied by a spatial redistribution of the emission. The theoretical description, however, is more complex than in the case of SWCNTs, because several radiating dipole orientations in the nanowire have to be taken into account that can interact with the tip. Nevertheless, the present results show that the metal tip can be utilized as a tool to control the angular emission and to increase the directivity of the signal besides its signal enhancing capability. This might be helpful for the improvement of the performance of nanoscale light emitting elements or future optoelectronic devices based on electroluminescence.

8 Summary and outlook

In this work, tip-enhanced near-field optical microscopy (TENOM) has been applied to quasi one-dimensional semiconducting materials, namely single-walled carbon nanotubes and CdSe nanowires. TENOM exploits the highly confined and strongly enhanced optical fields in the vicinity of a laser illuminated sharp metallic tip which acts as an optical antenna. These fields locally increase the spectroscopic response from the sample by enhancing the excitation and radiation rate, which results in a substantially higher sensitivity of this method and an outstanding spatial resolution beyond the diffraction limit.

The potential of TENOM has already been demonstrated for a variety of sample materials including single molecules, nanocrystals, RNA strands, carbon nanotubes, cellular membranes, polymer blends and graphene [12, 33, 93, 97, 106, 133, 145–148]. The underlying mechanisms however are not yet fully understood, e.g. the contributions of excitation and radiative rate enhancement are usually unknown, because the integrated optical response from the sample is detected without distinguishing them. One of the aims of this work was to develop a procedure that allows to separate and quantify the respective rate enhancement factors. Since TENOM is a well established tool for the investigation of the optical properties of single-walled carbon nanotubes (SWCNTs), this material was chosen for the investigation of the enhancement processes.

To study the enhancement mechanisms in TENOM on photoluminescent SWCNTs, the angular emission in the back focal plane of the microscope objective was imaged, and the resulting radiation patterns were compared with theoretical patterns. An important first result is that the photoluminescence emission of SWCNTs on a dielectric substrate without the influence of an optical antenna can be modelled as emission from a single in-plane point dipole despite the quasi 1D structure of the nanotubes. The next result is that the signal enhancement in the close vicinity of an optical antenna in form of a sharp gold tip is connected to a spatial redirection of the PL emission from the carbon nanotube. This redirection process could be attributed to the enhancement of the radiative rate, which is based on a transfer of energy from the nanotube to the antenna via near-field interactions. This energy is then radiated by the antenna dipole adopting the emission characteristics of the antenna itself. A control of the emission characteristics by an optical antenna, e.g. by adopting the antenna's directivity, as illustrated here, could be used to improve the performance of carbon nanotube based nanoscale NIR emitters and absorbers. Further, the enhancement factors of excitation (F_{ex}) and radiation (F_{rad}) have been quantified independently for the first time by analyzing the experimental radiation patterns. It was

found that in the present system of carbon nanotube and gold tip, the enhancement of the excitation rate dominates the overall enhancement. The observed enhancement factors for different tips and different nanotubes ranged from F_{ex} = 12-32 and F_{rad} = 6.1-13.6.

Besides gaining a deeper understanding of the enhancement mechanisms, this work aimed at the establishment of TENOM on other quasi one-dimensional materials than carbon nanotubes. This was accomplished using thin CdSe nanowires with diameters of about twice the exciton Bohr radius or smaller. Up to now, only first steps in this direction are known despite the high potential of TENOM to visualize the optical properties of such materials with its outstanding sensitivity and a resolution on the length scales interesting for potential nanoapplications [31, 33].

Using TENOM, the first high-contrast images of semiconducting CdSe nanowires were obtained and presented in this work. Also first hyperspectral images were measured, providing spectral informations with sub-diffraction spatial resolution. As a result, tip-enhanced near-field optical microscopy proved to be extremely well suited for the investigation of the optical properties of inorganic nanowires. The optical properties of CdSe nanowires were found to vary significantly on the nanoscale, leading to strong spatial fluctuations in both photoluminescence intensities and energies. Energy gradients up to 1 meV nm^{-1} along the quasi 1D structures have been revealed. A comprehensive optical characterization of the nanowires was possible by simultaneous detection of PL and Raman scattering by means of hyperspectral imaging. TENOM proved to be able to spatially resolve bundles of nanowires with different diameters according to their photoluminescence and Raman scattering signals. For these bundles, no indication of energy transfer to the smaller band gap component was found. These results show that a detailed optical characterization of these structures implicitly requires a spectrally resolving imaging technique with sub-diffraction spatial resolution, and that TENOM is highly qualified for this purpose.

An accurate interpretation of the obtained TENOM images requires the understanding of the influence of the gold tip on the spectral and angular emission characteristics of CdSe nanowires, which was addressed in the last part of this work. Near-field enhancement of the signal was found to be connected to spectral shifts of the PL signal in some cases. Different reasons are possible, including irregularities in and outside the nanowire and spectrally dependent signal enhancement by the tip. However, they could not be distinguished in the presented experiments due to the complexity of the investigated nanowires, exhibiting alternating crystal phases and potential diameter variations. A consequential result is that high-resolution TENOM imaging requires a careful data analysis and interpretation, in particular regarding energy variations of the observed PL signal. Another result of the TENOM investigation was that the model from [93] derived for Raman scattering from SWCNTs describes the experimental findings on CdSe nanowires quite well. This shows that the model can be also applied to inorganic semiconducting quasi 1D nanostructures.

The influence of the optical antenna was further investigated with respect to the angular PL emission from CdSe nanowires. A first result is that the radiation pattern of CdSe nanowires on a dielectric substrate appear to be similar to the radiation pattern of a single point dipole. The estimation of the nanowire orientation exploiting this description provides good results. But upon close inspection of the data, it was found that a second dipole is necessary for a satisfying agreement between measurement and calculation. This was attributed to the finite size of the nanowires perpendicular to their long axis which also allows for other dipole orientations and reveals the limitations of the one-dimensional treatment of the nanowires with quasi-zero diameters. Signal enhancement due to the presence of the gold tip was found to be always accompanied by a spatial redistribution of the emission. The theoretical description, however, is more complex than in the case of SWCNTs, because several radiating dipole orientations in the nanowire have to be taken into account that can interact with the tip. Nevertheless, the presented results show that optical antennas can be utilized as a tool to control the angular emission and to increase the directivity of the signal besides its signal enhancing capability. These findings will possibly help to improve the performance of optoelectronic devices, for example based on electroluminescence.

A high quality nanowire material with a homogeneous crystal phase and a constant diameter would be very helpful for future experiments following the present investigations. By studying nanowires with a homogeneous structure, tip-induced changes in the spectral emission characteristics of the nanowires could be attributed to the optical antenna only, since variations due to spatial averaging of different sample volumes could be excluded. It would be also interesting to study the angular emission and tip induced changes therein for nanowires of different diameters. For very thin nanowires with far smaller diameters, a one-dimensional description is expected to be sufficient to reproduce the observed angular radiation patterns. This is expected to result in the emission characteristics of a single in-plane point dipole, as it is the case for SWCNTs. A separation and quantification of the enhancement factors would then be possible. The sample material qualified for these experiments, however, is not yet available.

A combination of TENOM measurements and atomic-resolution structural data obtained by high-resolution transmission electron microscopy (HRTEM) from the same nanowire could be combined with theoretical calculations to predict the electronic energy landscape along single nanowires. The combination of TENOM and TEM could be also used for SWCNTs to correlate structural defects with Raman scattering informations.

A further goal is to combine TENOM with electrical transport measurements on single contacted 1D nanowires and -tubes. Tip-enhanced photocurrent and electroluminescence experiments would provide unprecedented insight into the properties of optoelectronic and photovoltaic devices on the nanoscale.

Appendix A: Light confinement by structured metal tips

This chapter is based on the paper *"Light confinement by structured metal tips for antenna-based scanning near-field optical microscopy"* published in *Proc. SPIE* (8105G, 2011), that resulted from a collaboration with Joachim Jambreck from the group of A. Bauer (Fraunhofer Institute for Integrated Systems and Devices (IISB), Erlangen, Germany).

TENOM utilizes the strong local electromagnetic fields near a laser illuminated sharp metal tip to probe the near-field response of the sample. To achieve a clear image contrast this near-field signal needs to exceed the background contribution resulting from simultaneous far-field excitation and far-field detection. For the resolution of TENOM the exact localization of the light emission plays a major role.

In this chapter, a way for improving the near-field-to-far-field-ratio, and the confinement of surface plasmon polaritons is presented for electrochemically etched conical gold tips. For that purpose, they have been structured using multiple three-dimensional nanopatterning with a focused ion beam (FIB). For the first time, surface plasmon Bragg reflectors were fabricated all around the tip in a well-defined distance to the tip apex to mimic finite length antenna structures, for which more efficient light confinement is expected. The design of the structures, the fabrication strategy, and the characterization of the resulting tips by scanning electron and optical microscopy is discussed. Photoluminescence spectra recorded before and after FIB modification of the tips indicate an increase of the light confinement of 60 %.

For antenna-based near-field optical microscopy, the far-field illumination and detection of the tip-sample region leads to two signal contributions. The first results from short ranged near-field interactions between probe and sample and contains high spatial information. The second is the background contribution that would also be detected in the absence of the tip. In the following, the two contributions are denoted near-field (NF) signal and far-field (FF) background. To achieve a clear image contrast, the NF signal needs to exceed the background. The emission from a relatively small region where the NF signal is originated has to compete against the emission from a far larger sample region which causes the FF background contribution. Different strategies have been developed to improve the image contrast by reducing the FF contribution. One option is to modulate the tip-sample distance while recording the optical response, associating small and large distances with

the NF and the FF signals, respectively [149]. Another option is to fabricate a combined probe, were the optical antenna is fixed at the apex of an aperture probe [109]. In this case the optical antenna is excited by the aperture probe. A third option is to reduce the FF contribution by the remote excitation of surface plasmons on the tip shaft propagating along the surface towards the tip apex. The momentum mismatch between photons and plasmons is compensated by fabricating grating structures into the surface of the tip using FIB milling [150–152].

Since elongated finite-sized metal particles and resonant antennas achieve higher field enhancements compared to semi-infinite metal tips, a grating structure acting as a Bragg reflector was introduced into the tip here to mimic a finite-sized structure [101]. A Bragg reflector for surface plasmon polaritons (SPPs) is a periodic stacking of regions with alternating refractive indices. It reflects a SPP travelling in the direction of the reflector due to interference effects [153]. For the accurate choice of the distance between apex and Bragg reflector, which is the length of the resulting antenna, the reduction of the vacuum wavelength λ_0 in small metal structures has to be taken into account. For rod-shaped nano-antennas, a scaling relation between λ_0 and the resulting effective wavelength λ_{eff} is reported in literature showing a strong dependence of the scaling factor on the rod diameter [105]. In general, the scaling factor will crucially depend on the shape of the considered structure and, therefore, only rough predictions are possible for the individually etched gold tips.

As starting probe material conventionally etched gold tips were used. A FEI Helios 600 dual beam system consisting of a focused ion beam and a scanning electron microscope was used for the fabrication and inspection of the tips. A FIB was used because the special geometry of the tips with a grating structured almost perpendicular to the tip surface requires a tool capable of three dimensional nano-structuring. It also offers the flexibility of fast adaption of parameters during the development process.

A target wavelength λ_0 of 660 nm was chosen, giving an effective wavelength of around $\lambda_{eff} = 500\,\text{nm}$ in the gold tip. The period p of the grating is chosen to equal one half wavelength in the respective media air and gold. The detailed structure of the periods is selected such that the gold parts (gold layers) have a width c of 125 nm and the grooves (air layers) have a width b of 165 nm, yielding $p = 290\,\text{nm}$ as the sum of b and c. The distance l of the first groove of the grating from the tip apex, which defines the length of the antenna, is chosen to 500 nm, corresponding to one effective wavelength. A cross section of the tip design is depicted in figure A.1 a.

In the used dual beam system the ion column is installed at an angle of 52° relative to the electron column. The sample holder can be rotated up to 360° and tilted up to 52°. For FIB processing, the tips were mounted on the holder with the apex oriented directly towards the electron column. In this case, the angle between the ion column and the symmetry axis of the tip is 52° and, therefore, the angle between the surface of the tip

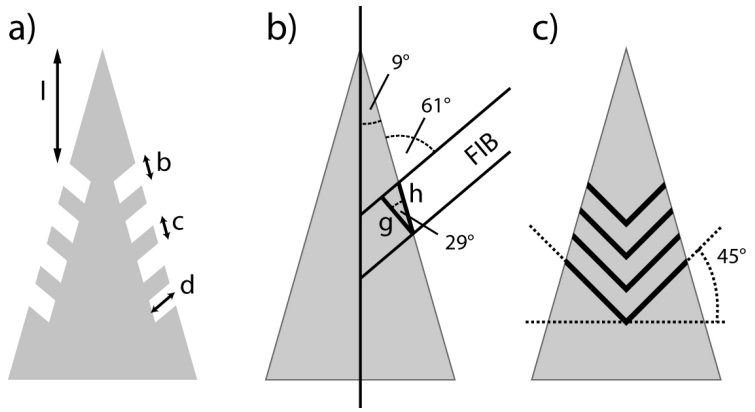

Figure A.1: a) Schematic of the tip design with the distance l of the first groove from the tip apex and the grating parameters b, c and d resulting in an appropriate Bragg reflector. b) Schematic of the geometry for milling in the dual beam system. Both schemes are cross sections containing the tip axis. c) Schematic of the FIB pattern on the tip seen by the ion gun.

and the ion column is 61° for the average opening angle of the tips of 18°. This has to be taken into account for the design of the milling patterns for the FIB processing. It means, for example, to structure a period p of 290 nm, the period in the FIB-pattern gp has to be adjusted to a value of 254 nm, according to

$$gp = p \cdot \cos 29^\circ = 290\,\text{nm} \cdot \cos 29^\circ = 254\,\text{nm}.$$

The distance gl of the first groove from the apex in the FIB-pattern is chosen to be 432 nm, because

$$gl = l \cdot \cos 9^\circ \cdot \cos 29^\circ = 500\,\text{nm} \cdot \cos 9^\circ \cdot \cos 29^\circ = 432\,\text{nm}.$$

The distance gl is the projection of the length l on the tip surface seen by the ion gun. A scheme of the tip including all relevant angles is depicted in figure A.1 b.

A schematic of the FIB-pattern on the tip is shown in figure A.1 c as seen from the direction of the ion beam. The thick black lines are the FIB-pattern i.e., the areas where the ion beam is scanned during FIB-milling. This pattern was milled from one side of the tip, then the tip was rotated about 180° around the tip axis, the pattern was aligned to the structures and milled from the second side. This yields a structure enclosing the tip shaft completely. A linear approximation in the patterns is chosen to compensate for the curved surface of the tip as well as for the angle between the tip axis and the ion beam. For that purpose, multiple V-shaped patterns were created, aligned to the tip so that the symmetry axis of the V-shape was congruent with the symmetry axis of the image of the tip, seen from the view of the ion gun.

In TENOM, the probes are scanned in close distance over the sample surface, which requires good mechanical stability of the tips. Therefore, the depth of the grooves is chosen deep enough to generate the required effect but maintaining mechanical stability.

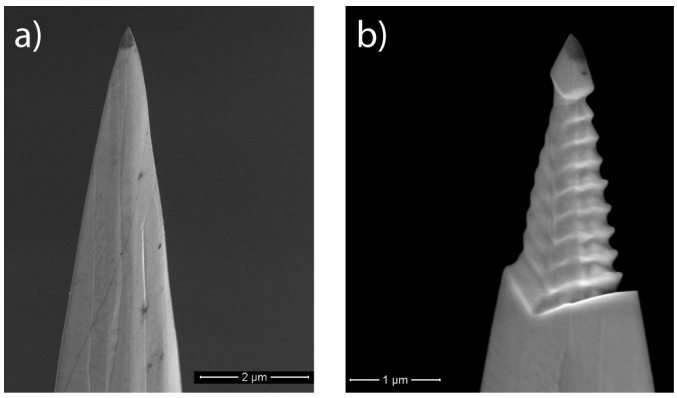

Figure A.2: Scanning electron microscopy images of a gold tip before (a) and after (b) FIB milling. The tip was structured from two opposite sides using optimized FIB patterns.

A depth d of 80 nm showed the best results. SEM images of the tips before and after FIB processing were recorded. Figure A.2 shows a typical tip before and after FIB milling. The SEM images are captured under an angle of 52° measured from the main axis of the tip.

The structures were fabricated using an ion beam with an acceleration voltage of 30 kV and the lowest ion currents possible by the ion gun (1.5 pA and 9.7 pA). This enables structuring fine details with a small beam diameter and thus minimizing damage due to ion beam broadening and beam tails in the regions not intended to be sputtered [154]. The low beam current also minimizes heating effects which may become critical for the small volume of material at the apex of the high aspect ratio tips. The apex becomes even more thermally isolated after the initial structures are milled, as heat conduction occurs through thinner remaining material. Starting milling from the tip and then moving step by step in direction of the shaft would not be an option due to redeposition issues. Therefore, the structures were milled in parallel mode, which means that the pattern was scanned completely and then re-scanned using multiple beam passes.

To characterize the optical properties of the tips and the effect of the grating structures, photoluminescence images and spectra before and after FIB structuring were recorded, since metal nanostructures are known to exhibit photoluminescence emission that reflects the spectral and spatial characteristics of their plasmonic response [135]. The tips were mounted onto a piezo-electric stage and excited by a Gaussian laser beam ($\lambda_{ex} = 473$ nm) oriented perpendicular to their symmetry axis. The laser beam was polarized along the tip apex and focused by an air objective (NA = 0.95). The light emitted from the tip was collected by the same objective and directed to an avalanche photodiode (APD) after spectral filtering of the optical response between 650 - 670 nm or into a spectrometer equipped with a charge-coupled device (CCD) camera.

In the PL images of the unmodified tip, presented in figure A.3 a, its contour is clearly visible with rather uniform PL intensities. The PL image after FIB structuring is shown

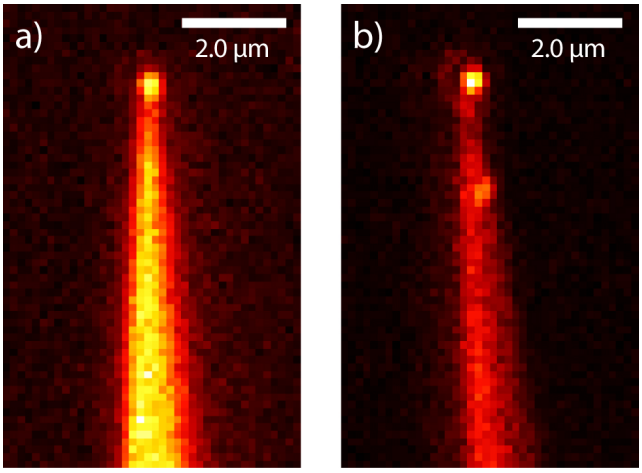

Figure A.3: Confocal luminescence scan images of a sharp gold tip before (a) and after (b) FIB milling. The polarization of the excitation light ($\lambda_{ex} = 473\,\text{nm}$) was parallel to the tip axis. The light emission from the apex of the tip clearly increased because of the modification. The intensity is normalized in both images.

in figure A.3 b. The tip now features a bright and localized PL emission at the tip apex exceeding the signal from the tip shaft, despite the small gold volume at the tip apex compared to the shaft. This indicates increased local field enhancement at the apex and more efficient coupling of these fields to propagating waves which can finally be detected.

To quantify the changes in the optical properties obtained after introducing the grating structures, the ratio between the PL signal at the tip apex and the shaft was estimated. The position on the shaft measurement was located on the tip axis in a distance of about 1 µm from the apex in the PL raster image. In this case both positions are still in the focal plane of the objective, while the tip volume at a position further away from the apex would reach beyond the focal expansion along optical axis. For a series of 6 tips fabricated with similar design parameters, an average increase of the contrast by a factor of about 1.6 was determined. In the case of tip presented above, even a factor of 3.3 was observed. The field enhancing capabilities of etched gold tips varies considerably from tip to tip, which explains the spread of the PL contrast in the experiments.

To explore the origin of the bright photoluminescence at the tip apex, spectra at different positions along the tip were acquired. Figure A.4 shows PL spectra of the tip from the shaft (circles) and from the apex before (rectangles) and the apex after FIB structuring (triangles). The spectrum at the shaft was acquired at a position located centrally on the tip in a distance of 5 µm form the apex. This position is not in the same focal plane of the objective as the apex, but it is chosen to minimize the influence of the apex in the collected spectrum. A clear broad enhancement around a wavelength of 650 nm can be observed at the tip apex after structuring. This broad peak is related to the plasmon resonance enhanced by the Bragg reflector. The spectrum along the shaft does not change due to the tip modification.

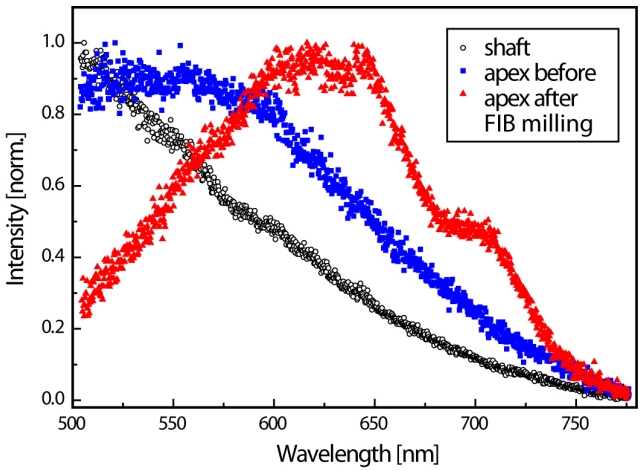

Figure A.4: PL spectra from the apex of a gold tip before (squares) and after (rectangles) FIB modification. Also shown is the optical response from the tip shaft (open circles). The spectrum after FIB milling shows a clear broad resonance at around 650 nm.

Another effect may play a role for the confinement of the emission as the Bragg reflectors could not only act on plasmons, but also on photons. Therefore, photons propagating approximately perpendicular to the grooves and in the direction from the apex to the shaft may be reflected by the FIB-generated structure which now acts as a one-dimensional photonic crystal [155]. The manufactured structure matches the conditions for the reflection of photons if they propagate approximately perpendicular to the grooves in the direction from the apex to the shaft, depending on their wavelength in detail. This condition is usually not fulfilled in the experiment since the focal fields comprises mostly evanescent fields decaying rapidly in z-direction. The probability of photons being reflected and coupled to the tip is thus relatively low. For this reason, the dominant effects should be the ed finite length antennas resulting in the Bragg reflection of the plasmons.

Conclusion

In this chapter, the optimization of conventional etched gold tips for optical imaging with sub-diffraction resolution down to the nanoscale was investigated. For the stronger enhancement of the near-field signal and the confinement of the light at the tip apex, special tips were designed and fabricated which allow a control of the electromagnetic fields. Gratings were structured from all sides to the tip in a defined distance to the apex of the tips to mimic finite length antennas. They result in Bragg reflectors yielding an increased field enhancement at the tip apex. It has been demonstrated that optimized FIB structuring can lead to significantly increased optical fields up to 330% in the best case. First TENOM experiments on carbon nanotubes including photoluminescence and Raman scattering indicate a high potential of the structured tips for near-field imaging. However, the FIB procedure is ambitious and time-consuming because of the required small structures, which hinders it from being easily applicable.

Appendix B: TENOM on substrates other than glass

In some cases, a combination of TENOM with complementary techniques is desirable for a better understanding of the sample's optical properties, e.g. with high-resolution transmission electron microscopy (HRTEM) in the case of CdSe nanowires on purpose of developing a model to predict the optical properties with nanoscale precision according to the TEM data or vice versa. The combination of TENOM and TEM could be also used for SWCNTs to correlate the knowledge of structural defects with Raman scattering information. A completely different idea is to combine SERS and TERS to obtain a burst of the signal enhancement. What both ideas have in common, is that these experiments are not possible with conventionally glass cover slips as substrates. Therefore TENOM measurements on other substrates would be highly desired, pushing forward the boarders of tip-enhanced near-field optical microscopy.

Here, the experimental tests with carbon nanotubes on a TEM grid and on a rough gold film are presented. It will be shown that TENOM is also possible under this unconventional conditions. However, this requires a high quality of the tips, the samples and the substrates since is it highly susceptible.

B.1 TENOM on a TEM grid

A schematic of the TENOM configuration for measurements on a conventional TEM grid is depicted in figure B.5 a. The sample was prepared by adding a drop of dispersed SWCNTs on a thin carbon film which is attached to a copper grid. Since the carbon film must lie flat on a glass cover slide for TENOM experiments, the nanotubes are added on the back side, where the film is attached to the Cu grid. The TEM grid is then gently mounted up-side-down onto the glass slide, so that the gold tip can be approached between the Cu bars from above. To avoid damaging of the carbon film, no mechanical forces must be applied to the TEM grid.

The resulting TENOM data are shown in figure B.5 b and c. The topography in (b) shows the nanotube but also other bumps that probably result from remaining surfactant, since the sample was not rinsed to avoid damaging of the carbon film. In the tip-enhanced Raman map, measured by integrating the optical response at 698 - 708 nm to image the G

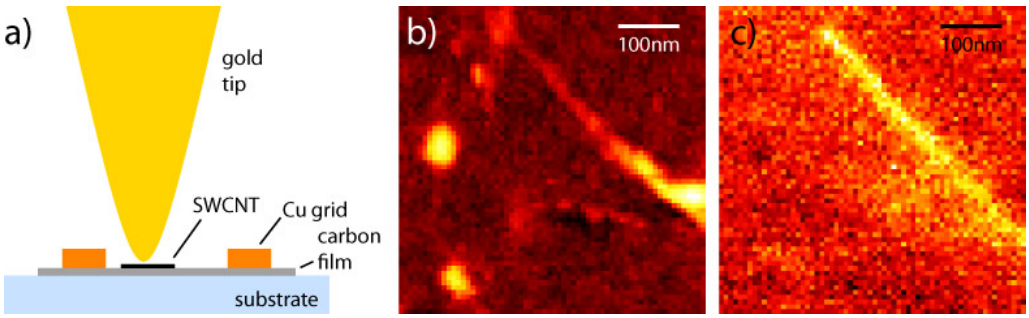

Figure B.5: a) Schematic of the TENOM configuration with a TEM grid as supporting material. The TEM sample is made of a copper grid carrying a thin carbon film on which the SWCNTs are placed. This sample is mounted on a conventional glass slide for optical investigations. The gold tip is approach from above and scanned inside the windows of the Cu grid. b) Topography showing a nanotube and additional surface contaminations. c) TENOM Raman image of the nanotube's G mode.

mode, the nanotube is clearly visible. The enhancement due to the gold tip is moderate, but still a spatial resolution of about 25 nm is found. The carbon film itself adds to the background, since as a carbonaceous material, it shows a Raman scattering signal. This problem could be avoided by measuring the photoluminescence signal of the nanotubes. In the presented example, the nanotube was metallic thus showing no PL signal at all.

B.2 TENOM on a rough gold film

Another substrate that has been tested is a glass cover slide covered with a thin rough gold film with a nominal thickness of 7.5 nm. The SWCNTs were spin coated on this substrate. For a smooth gold film non-radiative losses in the metal should result in a completely quenched photoluminescence. The rough gold film, on the other hand, might provide so called hot spots where the nanotubes could be freely suspended and will show enhanced PL because of surface enhancement. A representative confocal PL image is shown in figure B.6 a.

The presence of the expected hot spots gives rise to strong photoluminescence signals at several positions within the scanned area. Interestingly, the PL features are ring shaped pattern in the majority of the cases. This indicates transitions polarized perpendicular to the optical axis, since the strong longitudinal component in the center of the excitation focus is not imaged in contrast to the transversal components around the center.

The TENOM data measured at such a hot spot is shown in figure B.6 b and c. The topographical image in (b) reveals the typical structure of the rough gold film. The carbon nanotube, however, is not visible. In the simultaneously obtained TENOM PL image shown in (c), the enhanced optical response on top of the confocal background clearly indicates the exact position of the nanotube. The small offset between near-field

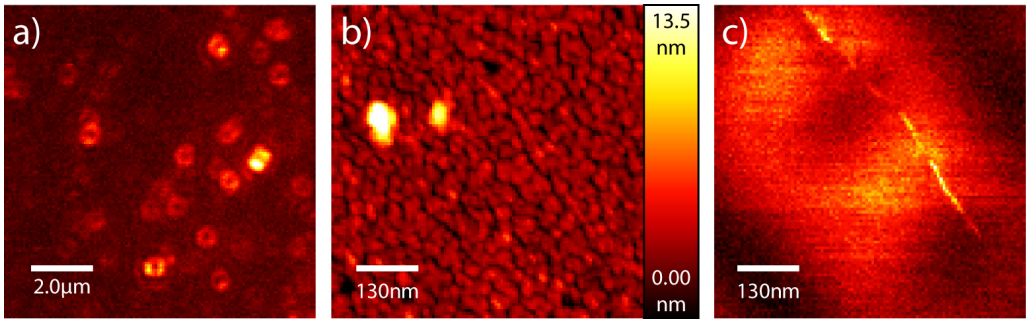

Figure B.6: a) Confocal PL image showing hot spots with bright PL signals that image the radially polarized excitation focus. b) The topography reveals the typical structure of the rough gold film. The carbon nanotube is not visible. c) The simultaneously measured TENOM PL image shows near-field enhanced PL signal above the confocal background, the spatial resolution is about 10 nm.

and confocal signal originates from a slightly misalignment of the gold tip. The spatial resolution of the near-field signal is about 10 nm.

Conclusion

For the first time it could be shown that TENOM is possible on TEM grids as well as rough gold films. This is the first step towards the combination of TENOM with other techniques as for example TEM. In the next step higher signal enhancements must be achieved resulting in a better image contrast. An improvement of the usually exploited etched tips would be thus desirable, also better sample preparation leading to a reduction of the background signal would increase the performance of such measurements. Detection of PL on gold films could exploit the additional signal enhancement provided by these structures.

Bibliography

[1] D. Appell. Nanotechnology: Wired for success. *Nature*, 419(6907):553–555, 2002. doi:10.1038/419553a.

[2] Z. L. Wang. New developments in transmission electron microscopy for nanotechnology. *Adv. Mater.*, 15(18):1497–1514, 2003. doi:10.1002/adma.200300384.

[3] M. Tortonese, R. C. Barrett, and C. F. Quate. Atomic resolution with an atomic force microscope using piezoresistive detection. *Appl. Phys. Lett.*, 62(8):834–836, 1993. doi:10.1063/1.108593.

[4] F. J. Giessibl. Advances in atomic force microscopy. *Rev. Mod. Phys.*, 75(3):949–983, 2003. doi:10.1103/RevModPhys.75.949.

[5] C. J. Chen. Origin of atomic resolution on metal surfaces in scanning tunneling microscopy. *Phys. Rev. Lett.*, 65(4):448–451, 1990. doi:10.1103/PhysRevLett.65.448.

[6] S. W. Hell and J. Wichmann. Breaking the diffraction resolution limit by stimulated emission: stimulated-emission-depletion fluorescence microscopy. *Opt. Lett.*, 19(11):780–782, 1994. doi:10.1364/OL.19.000780.

[7] E. Betzig, G. H. Patterson, R. Sougrat, O. W. Lindwasser, S. Olenych, J. S. Bonifacino, M. W. Davidson, J. Lippincott-Schwartz, and H. F. Hess. Imaging intracellular fluorescent proteins at nanometer resolution. *Science*, 313(5793):1642–1645, 2006. doi:10.1126/science.1127344.

[8] S. T. Hess, Th. P. K. Girirajan, and M. D. Mason. Ultra-high resolution imaging by fluorescence photoactivation localization microscopy. *Biophys J*, 91(11):4258–4272, 2006. doi:10.1529/biophysj.106.091116.

[9] M. J. Rust, M. Bates, and X. Zhuang. Sub-diffraction-limit imaging by stochastic optical reconstruction microscopy (storm). *Nat Methods*, 3(10):793–796, 2006. doi:10.1038/nmeth929.

[10] D. Liu, A. L. Pan, G. Z. Xu, Y. Q. Bai, X. Zhu, and B. S. Zou. Self-absorption effect in the spatial resolved spectra of CdS nano-ribbon optical waveguide observed by near-field spectroscopy. *Optical Review*, 13(4):235–238, 2006. doi:10.1007/s10043-006-0235-y.

[11] F. Keilmann and R. Hillenbrand. Near-field microscopy by elastic light scattering from a tip. *Philosophical Transactions of the Royal Society of London*, 362(1817):787–805, 2004. doi:10.1098/rsta.2003.1347.

[12] A. Hartschuh. Tip-enhanced near-field optical microscopy. *Angewandte Chemie International Edition*, 47(43):8178–8191, 2008. doi:10.1002/anie.200801605.

[13] L. Novotny and B. Hecht, editors. *Principles of Nano-Optics*. Cambirdge University Press, 2008.

[14] A. Jorio, G Dresselhaus, and M. S. Dresselhaus, editors. *Carbon Nanotubes*, volume 111 of *Topics in Applied Physics*. Springer-Verlag Berlin Heidelberg, 2008. doi:10.1071/978-3-540-72865-8.

[15] Y. Xia, P. Yang, Y. Sun, Y. Wu, B. Mayers, B. Gates, Y. Yin, F. Kim, and H. Yan. One-dimensional nanostructures: Synthesis, characterization, and applications. *Adv. Mater.*, 15(5):353–389, 2003. doi:10.1002/adma.200390087.

[16] M. Kuno. An overview of solution-based semiconductor nanowires: synthesis and optical studies. *Phys. Chem. Chem. Phys.*, 10(5):620–639, 2008. doi:10.1039/b708296g.

[17] R. H. Baughman, A. A. Zakhidov, and W. A. de Heer. Carbon nanotubes - the route toward applications. *Science*, 297(5582):787–792, 2002. doi:10.1126/science.1060928.

[18] T. Hertel. Carbon nanotubes: A brighter future. *Nat Photon*, 4(2):77–78, 2010. doi:10.1038/nphoton.2009.278.

[19] A. Hartschuh, E. J. Sánchez, X. S Xie, and L Novotny. High-resolution near-field raman microscopy of single-walled carbon nanotubes. *Phys. Rev. Lett.*, 90(9):095503–4, 2003. doi:10.1103/PhysRevLett.90.095503.

[20] H. Qian, P. T. Araujo, C. Georgi, T. Gokus, N. Hartmann, A. A. Green, A. Jorio, M. C. Hersam, L. Novotny, and A. Hartschuh. Visualizing the local optical response of semiconducting carbon nanotubes to DNA-wrapping. *Nano Lett.*, 8(9):2706–2711, 2008. doi:10.1021/nl801038t.

[21] H. Qian, C. Georgi, N. Anderson, A. A. Green, M. C. Hersam, L. Novotny, and A. Hartschuh. Exciton transfer and propagation in carbon nanotubes studied by near-field optical microscopy. *phys. stat. sol. (b)*, 245(10):2243–2246, 2008. doi:10.1002/pssb.200879598.

[22] L. G. Cançado, A. Hartschuh, and L. Novotny. Tip-enhanced raman spectroscopy of carbon nanotubes. *J. Raman Spec.*, 40(10):1420–1426, 2009. doi:10.1002/jrs.2448.

[23] C. Georgi and A. Hartschuh. Tip-enhanced raman spectroscopic imaging of localized defects in carbon nanotubes. *Appl. Phys. Lett.*, 97(14):143117–3, 2010. doi:10.1063/1.3499752.

[24] C. Georgi, A. A. Green, M. C. Hersam, and A. Hartschuh. Probing exciton localization in single-walled carbon nanotubes using high-resolution near-field microscopy. *ACS Nano*, 4(10):5914–5920, 2010. doi:10.1021/nn101443d.

[25] A. J. Baca, J.-H. Ahn, Y. Sun, M. A. Meitl, E. Menard, H.-S. Kim, W. M. Choi, D.-H. Kim, Y. Huang, and J. A. Rogers. Semiconductor wires and ribbons for high-performance flexible electronics. *Angew. Chem. Int. Ed.*, 47(30):5524–5542, 2008. doi:10.1002/anie.200703238.

[26] Y. Li, F. Qian, J. Xiang, and Ch. M. Lieber. Nanowire electronic and optoelectronic devices. *Mater. Today*, 9(10):18–27, 2006. doi:10.1016/S1369-7021(06)71650-9.

[27] H. Yu, J. Li, R. A. Loomis, P. C. Gibbons, L.-W. Wang, and W. E. Buhro. Cadmium selenide quantum wires and the transition from 3D to 2D confinement. *J. Am. Chem. Soc.*, 125(52):16168–16169, 2003. doi:10.1021/ja037971+.

[28] J. Li and L.-W. Wang. Shape effects on electronic states of nanocrystals. *Nano Lett.*, 3(10):1357–1363, 2003. doi:10.1021/nl034488o.

[29] V. V. Protasenko, K. L. Hull, and M. Kuno. Disorder-induced optical heterogeneity in single CdSe nanowires. *Adv. Mater.*, 17(24):2942–2949, 2005. doi:10.1002/adma.200501660.

[30] A. M. Mintairov, J. Herzog, M. Kuno, and J. L. Merz. Near-field scanning optical microscopy of colloidal CdSe nanowires. *phys. stat. sol. (b)*, 247(6):1416–1419, 2010. doi:10.1002/pssb.200983201.

[31] E. Yoskovitz, G. Menagen, A. Sitt, E. Lachman, and U. Banin. Nanoscale near-field imaging of excitons in single heterostructured nanorods. *Nano Lett.*, 10(8):3068–3072, 2010. doi:10.1021/nl101614s.

[32] L. F. Zagonel, S. Mazzucco, M. Tencé, K. March, R. Bernard, B. Laslier, G. Jacopin, M. Tchernycheva, L. Rigutti, F. H. Julien, R. Songmuang, and M. Kociak. Nanometer scale spectral imaging of quantum emitters in nanowires and its correlation to their atomically resolved structure. *Nano Lett.*, 11(2):568–573, 2011. doi:10.1021/nl103549t.

[33] S. Berweger, C. C. Neacsu, Y. Mao, H. Zhou, S. S. Wong, and M. B. Raschke. Optical nanocrystallography with tip-enhanced phonon raman spectroscopy. *Nat Nano*, 4(8):496–499, 2009. doi:10.1038/nnano.2009.190.

[34] S. Berweger and M. Raschke. Signal limitations in tip-enhanced raman scattering: the challenge to become a routine analytical technique. *Analytical and Bioanalytical Chemistry*, 396(1):115–123, 2010. doi:10.1007/s00216-009-3085-1.

[35] H. Dai. Carbon nanotubes: Synthesis, integration, and properties. *Acc. Chem. Res.*, 35(12):1035–1044, 2002. doi:10.1021/ar0101640.

[36] C. M. Lieber and Z. L. Wang. Functional nanowires. *MRS Bull.*, 32:99–108, 2007. doi:10.1557/mrs2007.41.

[37] Rodrigo B. Capaz, Catalin D. Spataru, Sohrab Ismail-Beigi, and Steven G. Louie. Diameter and chirality dependence of exciton properties in carbon nanotubes. *Phys. Rev. B*, 74(12):121401–4, 2006. doi:10.1103/PhysRevB.74.121401.

[38] J. G. Vilhena, S. Botti, and M. A. L. Marques. Excitonic effects in the optical properties of CdSe nanowires. *Appl. Phys. Lett.*, 96(12):123106–3, 2010. doi:10.1063/1.3368126.

[39] C. Georgi. *Exciton Mobility and Localized Defects in Single Carbon Nanotubes Studied with Tip-Enhanced Near-Field Optical Microscopy.* PhD thesis, Ludwig-Maximilians-Universität München, 2011.

[40] H. Qian. *Tip-enhanced Near-Field Optical Spectroscopy on Single-Walled Carbon Nanotubes.* PhD thesis, Ludwig-Maximilians-Universität, 2008.

[41] R. Saito, G. Dresselhaus, and M. S. Dresselhaus. *Physical Properties of Carbon Nanotubes.* Imperial College Press, London, 1998.

[42] S. Reich, C. Thomsen, and J. Maultzsch. *Carbon Nanotubes: Basic Concepts and Physical Properties.* Wiley-VCH, Berlin, 2004.

[43] J. Maultzsch, R. Pomraenke, S. Reich, E. Chang, D. Prezzi, A. Ruini, E. Molinari, M. S. Strano, C. Thomsen, and C. Lienau. Exciton binding energies in carbon nanotubes from two-photon photoluminescence. *Phys. Rev. B*, 72(24):241402–, 2005. doi:10.1103/PhysRevB.72.241402.

[44] A. J. Siitonen, D. A. Tsyboulski, S.i M. Bachilo, and R. B. Weisman. Surfactant-dependent exciton mobility in single-walled carbon nanotubes studied by single-molecule reactions. *Nano Lett.*, 10:1595–1599, 2010. doi:10.1021/nl9039845.

[45] C. Georgi, M. Böhmler, H. Qian, L. Novotny, and A. Hartschuh. Probing exciton propagation and quenching in carbon nanotubes with near-field optical microscopy. *phys. stat. sol. (b)*, 246(11-12):2683–2688, 2009. doi:10.1002/pssb.200982306.

[46] Y. Miyauchi, H. Hirori, K. Matsuda, and Y. Kanemitsu. Radiative lifetimes and coherence lengths of one-dimensional excitons in single-walled carbon nanotubes. *Phys. Rev. B*, 80(8):081410–4, 2009. doi:10.1103/PhysRevB.80.081410.

[47] C. Manzoni, A. Gambetta, E. Menna, M. Meneghetti, G. Lanzani, and G. Cerullo. Intersubband exciton relaxation dynamics in single-walled carbon nanotubes. *Phys. Rev. Lett.*, 94(20):207401–4, 2005. doi:10.1103/PhysRevLett.94.207401.

[48] T. Hertel, V. Perebeinos, J. Crochet, K. Arnold, M. Kappes, and Ph. Avouris. Intersubband decay of 1D exciton resonances in carbon nanotubes. *Nano Lett.*, 8(1):87–91, 2008. doi:10.1021/nl0720915.

[49] Y.-Z. Ma, M. W. Graham, G. R. Fleming, A. A. Green, and M. C. Hersam. Ultrafast exciton dephasing in semiconducting single-walled carbon nanotubes. *Phys. Rev. Lett.*, 101(21):217402–4, 2008. doi:10.1103/PhysRevLett.101.217402.

[50] H. Qian, C. Georgi, N. Anderson, A. A. Green, M. C. Hersam, L. Novotny, and A. Hartschuh. Exciton energy transfer in pairs of single-walled carbon nanotubes. *Nano Lett.*, 8(5):1363–1367, 2008. doi:10.1021/nl080048r.

[51] F. Tuinstra and J. L. Koenig. Raman spectrum of graphite. *J. Chem. Phys.*, 53(3):1126–1130, 1970. doi:10.1063/1.1674108.

[52] M. M. Lucchese, F. Stavale, E. H. Martins Ferreira, C. Vilani, M. V. O. Moutinho, Rodrigo B. Capaz, C. A. Achete, and A. Jorio. Quantifying ion-induced defects and raman relaxation length in graphene. *Carbon*, 48(5):1592–1597, 2010. doi:10.1016/j.carbon.2009.12.057.

[53] N. Anderson, A. Bouhelier, and L. Novotny. Near-field photonics: tip-enhanced microscopy and spectroscopy on the nanoscale. *J. Opt. A-Pure Appl. Op.*, 8(4):227–233, 2006. doi:10.1088/1464-4258/8/4/S24.

[54] Z. Fan, J. C. Ho, Z. A. Jacobson, H. Razavi, and A. Javey. Large-scale, heterogeneous integration of nanowire arrays for image sensor circuitry. *P. Natl. Aca. Sci.*, 105(32):11066–11070, 2008. doi:10.1073/pnas.0801994105.

[55] A. Singh, X. Li, V. Protasenko, G. Galantai, M. Kuno, H. (G.) Xing, and D. Jena. Polarization-sensitive nanowire photodetectors based on solution-synthesized CdSe quantum-wire solids. *Nano Lett.*, 7(10):2999–3006, 2007. doi:10.1021/nl0713023.

[56] P. Yang, R. Yan, and M. Fardy. Semiconductor nanowire: What's next? *Nano Lett.*, 10(5):1529–1536, 2010. doi:10.1021/nl100665r.

[57] Y. Yu, P. V. Kamat, and M. Kuno. A cdse nanowire/quantum dot hybrid architecture for improving solar cell performance. *Adv. Funct. Mater.*, 20(9):1464–1472, 2010. doi:10.1002/adfm.200902372.

[58] S. J. Rosenthal, J. McBride, S. J. Pennycook, and L. C. Feldman. Synthesis, surface studies, composition and structural characterization of CdSe, core/shell and biologically active nanocrystals. *Surf. Sci. Rep.*, 62(4):111–157, 2007. doi:10.1016/j.surfrep.2007.02.001.

[59] W. Lu and Ch. M Lieber. Semiconductor nanowires. *Journal of Physics D: Applied Physics*, 39(21):387–406, 2006. doi:10.1088/0022-3727/39/21/R01.

[60] C. Kittel. *Introduction to Solid States Physics*. John Wiley & Sons, Inc., 7th ed. edition, 1996.

[61] A. Kobayashi, O. F. Sankey, S. M. Volz, and J. D. Dow. Semiempirical tight-binding band structures of wurtzite semiconductors: AlN, CdS, CdSe, ZnS, and ZnO. *Phys. Rev. B*, 28(2):935–945, 1983. doi:10.1103/PhysRevB.28.935.

[62] A. L. Efros, M. Rosen, M. Kuno, M. Nirmal, D. J. Norris, and M. Bawendi. Band-edge exciton in quantum dots of semiconductors with a degenerate valence band: Dark and bright exciton states. *Phys. Rev. B*, 54(7):4843–4856, 1996. doi:10.1103/PhysRevB.54.4843.

[63] T. Kippeny, L. A. Swafford, and S. J. Rosenthal. Semiconductor nanocrystals: A powerful visual aid for introducing the particle in a box. *J. Chem. Educ.*, 79(9):1094–1100, 2002. doi:10.1021/ed079p1094.

[64] Q. Zhao, P. A. Graf, W. B. Jones, A. Franceschetti, J. Li, L.-W. Wang, and K. Kim. Shape dependence of band-edge exciton fine structure in CdSe nanocrystals. *Nano Lett.*, 7(11):3274–3280, 2007. doi:10.1021/nl0713070.

[65] U. E. H. Laheld and G. T. Einevoll. Excitons in CdSe quantum dots. *Phys. Rev. B*, 55(8):5184–5204, 1997. doi:10.1103/PhysRevB.55.5184.

[66] D. J. Norris and M. G. Bawendi. Measurement and assignment of the size-dependent optical spectrum in CdSe quantum dots. *Phys. Rev. B*, 53(24):16338–16346, 1996. doi:10.1103/PhysRevB.53.16338.

[67] X. Chen, A. Nazzal, D. Goorskey, M. Xiao, Z. A. Peng, and X. Peng. Polarization spectroscopy of single CdSe quantum rods. *Phys. Rev. B*, 64(24):245304–4, 2001. doi:10.1103/PhysRevB.64.245304.

[68] M. Nirmal, B. O. Dabbousi, M. G. Bawendi, J. J. Macklin, J. K. Trautman, T. D. Harris, and L. E. Brus. Fluorescence intermittency in single cadmium selenide nanocrystals. *Nature*, 383:802–804, 1996. doi:10.1038/383802a0.

[69] D. V. Talapin, A. L. Rogach, A. Kornowski, M. Haase, and H. Weller. Highly luminescent monodisperse CdSe and CdSe/ZnS nanocrystals synthesized in a hexadecylamine - trioctylphosphine oxide - trioctylphospine mixture. *Nano Lett.*, 1(4):207–211, 2001. doi:10.1021/nl0155126.

[70] J. McBride, J. Treadway, L. C. Feldman, S. J. Pennycook, and S. J. Rosenthal. Structural basis for near unity quantum yield core/shell nanostructures. *Nano Lett.*, 6(7):1496–1501, 2006. doi:10.1021/nl060993k.

[71] J. Hu, L. Wang, L. Li, W. Yang, and A. P. Alivisatos. Semiempirical pseudopotential calculation of electronic states of cdse quantum rods. *J. Phys. Chem. B*, 106(10):2447–2452, 2002. doi:10.1021/jp013204q.

[72] E. A. Muljarov, E. A. Zhukov, V. S. Dneprovskii, and Y. Masumoto. Dielectrically enhanced excitons in semiconductor-insulator quantum wires: Theory and experiment. *Phys. Rev. B*, 62(11):7420–7432, 2000. doi:10.1103/PhysRevB.62.7420.

[73] A. Shabaev and A. L. Efros. 1D exciton spectroscopy of semiconductor nanorods. *Nano Lett.*, 4(10):1821–1825, 2004. doi:10.1021/nl049216f.

[74] J. J. Glennon, R. Tang, W. E. Buhro, R. A. Loomis, D. A. Bussian, H. Htoon, and V. I. Klimov. Exciton localization and migration in individual CdSe quantum wires at low temperatures. *Phys. Rev. B*, 80(8):081303–4, 2009. doi:10.1103/PhysRevB.80.081303.

[75] I. Robel, B. A. Bunker, P. V. Kamat, and M. Kuno. Exciton recombination dynamics in CdSe nanowires: Bimolecular to three-carrier auger kinetics. *Nano Lett.*, 6(7):1344–1349, 2006. doi:10.1021/nl060199z.

[76] A. Myalitsin, Ch. Strelow, Z. Wang, Z. Li, T. Kipp, and A. Mews. Diameter scaling of the optical band gap in individual CdSe nanowires. *ACS Nano*, 5(10):7920–7927, 2011. doi:10.1021/nn202199f.

[77] J. J. Glennon, W. E. Buhro, and R. A. Loomis. Simple surface-trap-filling model for photoluminescence blinking spanning entire CdSe quantum wires. *J. Phys. Chem. C*, 112(13):4813–4817, 2008. doi:10.1021/jp710067b.

[78] L. Manna, E. C. Scher, and A. P. Alivisatos. Synthesis of soluble and processable rod-, arrow-, teardrop-, and tetrapod-shaped CdSe nanocrystals. *J. Am. Chem. Soc.*, 122(51):12700–12706, 2000. doi:10.1021/ja003055+.

[79] P. D. Cozzoli, T. Pellegrino, and L. Manna. Synthesis, properties and perspectives of hybrid nanocrystal structures. *Chem. Soc. Rev.*, 35(11):1195–1208, 2006. doi:10.1039/B517790C.

[80] L. J. Lauhon, M. S. Gudiksen, and Ch. M. Lieber. Semiconductor nanowire heterostructures. *Philosophical Transactions of the Royal Society of London*, 362(1819):1247–1260, 2004. doi:10.1098/rsta.2004.1377.

[81] L. Manna, D. J. Milliron, A. Meisel, E. C. Scher, and A. P. Alivisatos. Controlled growth of tetrapod-branched inorganic nanocrystals. *Nat Mater*, 2(6):382–385, 2003. doi:10.1038/nmat902.

[82] D. V. Talapin, J. H. Nelson, E. V. Shevchenko, S. Aloni, B. Sadtler, and A. P. Alivisatos. Seeded growth of highly luminescent CdSe/CdS nanoheterostructures

with rod and tetrapod morphologies. *Nano Lett.*, 7(10):2951–2959, 2007. doi:10.1021/nl072003g.

[83] J. W. Grebinski, K. L. Hull, J. Zhang, Th. H. Kosel, and M. Kuno. Solution-based straight and branched CdSe nanowires. *Chemistry of Materials*, 16(25):5260–5272, 2004. doi:10.1021/cm048498h.

[84] F. Wang, A. Dong, J. Sun, R. Tang, H. Yu, and W. E. Buhro. Solution-liquid-solid growth of semiconductor nanowires. *Inorganic Chemistry*, 45(19):7511–7521, 2006. doi:10.1021/ic060498r.

[85] Z. Li, Ö. Kurtulus, N. Fu, Z. Wang, A. Kornowski, U. Pietsch, and A. Mews. Controlled synthesis of CdSe nanowires by solution-liquid-solid method. *Adv. Funct. Mater.*, 19(22):3650–3661, 2009. doi:10.1002/adfm.200900569.

[86] R. H Webb. Confocal optical microscopy. *Rep. Prog. Phys.*, 59(3):427–471, 1996. doi:10.1088/0034-4885/59/3/003.

[87] J. B. Pawley, editor. *Handbook of Biological Confocal Microscopy*. Springer Berlin, 3rd edition, 2006.

[88] E. H. Synge. A suggested model for extending microscopic resolution into the unltramicroscopic region. *Phil. Mag.*, 6:356–362, 1928.

[89] D. W. Pohl, W. Denk, and M. Lanz. Optical stethoscopy: Image recording with resolution $\lambda/20$. *Appl. Phys. Lett.*, 44(7):651–653, 1984. doi:10.1063/1.94865.

[90] B. Knoll and F. Keilmann. Enhanced dielectric contrast in scattering-type scanning near-field optical microscopy. *Optics Communications*, 182(4-6):321–328, 2000. doi:10.1016/S0030-4018(00)00826-9.

[91] T. Ichimura, S. Fujii, T. Verma, P.and Yano, Y. Inouye, and S. Kawata. Subnanometric near-field raman investigation in the vicinity of a metallic nanostructure. *Phys. Rev. Lett.*, 102(18):186101–4, 2009. doi:10.1103/PhysRevLett.102.186101.

[92] S. Kawata, Y. Inouye, and P. Verma. Plasmonics for near-field nano-imaging and superlensing. *Nat Photon*, 3(7):388–394, 2009. doi:10.1038/nphoton.2009.111.

[93] L. G. Cançado, A. Jorio, A. Ismach, E. Joselevich, A. Hartschuh, and L. Novotny. Mechanism of near-field raman enhancement in one-dimensional systems. *Phys. Rev. Lett.*, 103(18):186101–4, 2009. doi:10.1103/PhysRevLett.103.186101.

[94] L. Novotny, E. J. Sánchez, and X. S. Xie. Near-field optical imaging using metal tips illuminated by higher-order hermite-gaussian beams. *Ultramicroscopy*, 71(1-4):21–29, 1998. doi:10.1016/S0304-3991(97)00077-6.

[95] A. Hartschuh. Tip-enhanced optical spectroscopy. *Philosophical Transactions of the Royal Society of London. Series A:Mathematical, Physical and Engineering Sciences*, 362(1817):807–819, 2004. doi:10.1098/rsta.2003.1348.

[96] P. G. Etchegoin and E. C. Le Ru. A perspective on single molecule sers: current status and future challenges. *Phys. Chem. Chem. Phys.*, 10(40):6079–6089, 2008. doi:10.1039/b809196j.

[97] P. Anger, P. Bharadwaj, and L. Novotny. Enhancement and quenching of single-molecule fluorescence. *Phys. Rev. Lett.*, 96(11):113002–4, 2006. doi:10.1103/PhysRevLett.96.113002.

[98] S. Kühn, U. Hakanson, L. Rogobete, and V. Sandoghdar. Enhancement of single-molecule fluorescence using a gold nanoparticle as an optical nanoantenna. *Phys. Rev. Lett.*, 97(1):017402–4, 2006. doi:10.1103/PhysRevLett.97.017402.

[99] Y. Ebenstein, E. Yoskovitz, R. Costi, A. Aharoni, and U. Banin. Interaction of scanning probes with semiconductor nanocrystals; physical mechanism and basis for near-field optical imaging. *J. Phys. Chem. A*, 110(27):8297–8303, 2006. doi:10.1021/jp056229o.

[100] F. M. Huang and D. Richards. Fluorescence enhancement and energy transfer in apertureless scanning near-field optical microscopy. *J. Opt. A-Pure Appl. Op.*, 8(4):234–238, 2006. doi:10.1088/1464-4258/8/4/S25.

[101] P. Bharadwaj, B. Deutsch, and L. Novotny. Optical antennas. *Advances in Optics and Photonics*, 1:438–483, 2009. doi:10.1364/AOP.1.000438.

[102] J. Wessel. Surface-enhanced optical microscopy. *J. Opt. Soc. Am. B*, 2(9):1538–1541, 1985. doi:10.1364/JOSAB.2.001538.

[103] U. Ch. Fischer and D. W. Pohl. Observation of single-particle plasmons by near-field optical microscopy. *Phys. Rev. Lett.*, 62(4):458–461, 1989. doi:10.1103/PhysRevLett.62.458.

[104] P. Drude. Zur Elektronentheorie der Metalle. *Ann. Phys.*, 306(3):566–613, 1900. doi:10.1002/andp.19003060312.

[105] L. Novotny. Effective wavelength scaling for optical antennas. *Phys. Rev. Lett.*, 98(26):266802, 2007. doi:10.1103/PhysRevLett.98.266802.

[106] P. Bharadwaj, P. Anger, and L. Novotny. Nanoplasmonic enhancement of single-molecule fluorescence. *Nanotechnology*, 18(4):044017–5, 2007. doi:10.1088/0957-4484/18/4/044017.

[107] A. G. Curto, G. Volpe, T. H. Taminiau, M. P. Kreuzer, R. Quidant, and N. F. van Hulst. Unidirectional emission of a quantum dot coupled to a nanoantenna. *Science*, 329(5994):930–933, 2010. doi:10.1126/science.1191922.

[108] S. Kühn, G. Mori, M. Agio, and V. Sandoghdar. Modification of single molecule fluorescence close to a nanostructure: radiation pattern, spontaneous emission and quenching. *Mol. Phys.*, 106(7):893–908, 2008. doi:10.1080/00268970802002510.

[109] T. H. Taminiau, D. F. Stefani, B. F. Segerink, and N. F. van Hulst. Optical antennas direct single-molecule emission. *Nat Photon*, 2(4):234–237, 2008. doi:10.1038/nphoton.2008.32.

[110] T. H Taminiau, D. F. Stefani, and N. F. van Hulst. Single emitters coupled to plasmonic nano-antennas: angular emission and collection efficiency. *New Journal of Physics*, 10(10):105005–16, 2008. doi:10.1088/1367-2630/10/10/105005.

[111] E. C. Le Ru, P. G. Etchegoin, J. Grand, N. Félidj, J. Aubard, and G. Lévi. Mechanisms of spectral profile modification in surface-enhanced fluorescence. *J. Phys. Chem. C*, 111(44):16076–16079, 2007. doi:10.1021/jp076003g.

[112] M. A. Lieb, J. M. Zavislan, and L. Novotny. Single-molecule orientations determined by direct emission pattern imaging. *J. Opt. Soc. Am. B*, 21(6):1210–1215, 2004. doi:10.1364/JOSAB.21.001210.

[113] R. Ruppin. Decay of an excited molecule near a small metal sphere. *J. Chem. Phys.*, 76(4):1681–1684, 1982. doi:10.1063/1.443196.

[114] H. Gersen, M. F. García-Parajó, L. Novotny, J. A. Veerman, L. Kuipers, and N. F. van Hulst. Influencing the angular emission of a single molecule. *Phys. Rev. Lett.*, 85(25):5312–4, 2000. doi:10.1103/PhysRevLett.85.5312.

[115] N. Hayazawa, T. Yano, H. Watanabe, Y. Inouye, and S. Kawata. Detection of an individual single-wall carbon nanotube by tip-enhanced near-field raman spectroscopy. *Chem. Phys. Lett.*, 376(1-2):174–180, 2003. doi:10.1016/S0009-2614(03)00883-2.

[116] T. Yano, P. Verma, S. Kawata, and Y. Inouye. Diameter-selective near-field raman analysis and imaging of isolated carbon nanotube bundles. *Appl. Phys. Lett.*, 88(9):093125–3, 2006. doi:10.1063/1.2178490.

[117] D. Roy, J. Wang, and M. E. Welland. Nanoscale imaging of carbon nanotubes using tip enhanced raman spectroscopy in reflection mode. *Faraday Discuss.*, 132:215–247, 2006. doi:10.1039/B506365E.

[118] L. Cognet, D. A. Tsyboulski, J.-D. R. Rocha, C. D. Doyle, J. M. Tour, and R. B. Weisman. Stepwise quenching of exciton fluorescence in carbon nanotubes by single-molecule reactions. *Science*, 316(5830):1465–1468, 2007. doi:10.1126/science.1141316.

[119] N. Anderson, A. Hartschuh, and L. Novotny. Chirality changes in carbon nanotubes studied with near-field raman spectroscopy. *Nano Lett.*, 7(3):577–582, 2007. doi:10.1021/nl0622496.

[120] J. Prasek, J. Drbohlavova, J. Chomoucka, J. Hubalek, O. Jasek, V. Adam, and R. Kizek. Methods for carbon nanotubes synthesis. *J. Mater. Chem.*, 21(40):15872–15884, 2011. doi:10.1039/C1JM12254A.

[121] J. H. Hafner, M. J. Bronikowski, B. R. Azamian, P. Nikolaev, A. G. Rinzler, D. T. Colbert, K. A. Smith, and R. E. Smalley. Catalytic growth of single-wall carbon nanotubes from metal particles. *Chem. Phys. Lett.*, 296(1-2):195–202, 1998. doi:10.1016/S0009-2614(98)01024-0.

[122] A. M. Cassell, J. A. Raymakers, J. Kong, and H. Dai. Large scale CVD synthesis of single-walled carbon nanotubes. *J. Phys. Chem. B*, 103(31):6484–6492, 1999. doi:10.1021/jp990957s.

[123] M. S. Arnold, S. I. Stupp, and M. C. Hersam. Enrichment of single-walled carbon nanotubes by diameter in density gradients. *Nano Lett.*, 5(4):713–718, 2005. doi:10.1021/nl050133o.

[124] M. S. Arnold, A. A. Green, J. F. Hulvat, S. I. Stupp, and M. C. Hersam. Sorting carbon nanotubes by electronic structure using density differentiation. *Nat Nano*, 1(1):60–65, 2006. doi:10.1038/nnano.2006.52.

[125] A. A. Green and M. C. Hersam. Ultracentrifugation of single-walled nanotubes. *Mater. Today*, 10(12):59–60, 2007. doi:10.1016/S1369-7021(07)70309-7.

[126] S. Iijima and T. Ichihashi. Single-shell carbon nanotubes of 1 nm diameter. *Nature*, 363(6430):603–605, 1993. doi:10.1038/363603a0.

[127] D. S. Bethune, C. H. Klang, M. S. de Vries, G. Gorman, R. Savoy, J. Vazquez, and R. Beyers. Cobalt-catalysed growth of carbon nanotubes with single-atomic-layer walls. *Nature*, 363(6430):605–607, 1993. doi:10.1038/363605a0.

[128] N. Stürzl, F. Hennrich, S. Lebedkin, and M. M. Kappes. Near monochiral single-walled carbon nanotube dispersions in organic solvents. *J. Phys. Chem. C*, 113(33):14628–14632, 2009. doi:10.1021/jp902788y.

[129] R. Dorn, S. Quabis, and G. Leuchs. Sharper focus for a radially polarized light beam. *Phys. Rev. Lett.*, 91(23):233901–4, 2003. doi:10.1103/PhysRevLett.91.233901.

[130] B. Ren, G. Picardi, and B. Pettinger. Preparation of gold tips suitable for tip-enhanced raman spectroscopy and light emission by electrochemical etching. *Rev. Sci. Instrum.*, 75(4):837–841, 2004. doi:10.1063/1.1688442.

[131] C. Williams and D. Roy. Fabrication of gold tips suitable for tip-enhanced raman spectroscopy. *J. Vac. Sci. Technol. B*, 26(5):1761–1764, 2008. doi:10.1116/1.2981078.

[132] L. Eligal, F. Culfaz, V. McCaughan, N. I. Cade, and D. Richards. Etching gold tips suitable for tip-enhanced near-field optical microscopy. *Rev. Sci. Instrum.*, 80(3):033701–3, 2009. doi:10.1063/1.3090174.

[133] D. Zhang, U. Heinemeyer, C. Stanciu, M. Sackrow, K. Braun, L. E. Hennemann, X. Wang, R. Scholz, F. Schreiber, and A. J. Meixner. Nanoscale spectroscopic imaging of organic semiconductor films by plasmon-polariton coupling. *Phys. Rev. Lett.*, 104(5):056601–4, 2010. doi:10.1103/PhysRevLett.104.056601.

[134] C. Georgi, N. Hartmann, T. Gokus, A. A. Green, M. C. Hersam, and A. Hartschuh. Photoinduced luminescence blinking and bleaching in individual single-walled carbon nanotubes. *Chem. Phys. Chem*, 9(10):1460–1464, 2008. doi:10.1002/cphc.200800179.

[135] A. Bouhelier, R. Bachelot, G. Lerondel, S. Kostcheev, P. Royer, and G. P. Wiederrecht. Surface plasmon characteristics of tunable photoluminescence in single gold nanorods. *Phys. Rev. Lett.*, 95(26):267405–4, 2005. doi:10.1103/PhysRevLett.95.267405.

[136] M. R. Beversluis, A. Bouhelier, and L. Novotny. Continuum generation from single gold nanostructures through near-field mediated intraband transitions. *Phys. Rev. B*, 68(11):115433–10, 2003. doi:10.1103/PhysRevB.68.115433.

[137] A. Lan, J. Giblin, V. Protasenko, and M. Kuno. Excitation and photoluminescence polarization anisotropy of single CdSe nanowires. *Appl. Phys. Lett.*, 92(18):183110–3, 2008. doi:10.1063/1.2924767.

[138] C. X. Shan, Z. Liu, and S. K. Hark. Photoluminescence polarization in individual CdSe nanowires. *Phys. Rev. B*, 74(15):153402–4, 2006. doi:10.1103/PhysRevB.74.153402.

[139] G. Y. Slepyan, M. V. Shuba, S. A. Maksimenko, and A. Lakhtakia. Theory of optical scattering by achiral carbon nanotubes and their potential as optical nanoantennas. *Phys. Rev. B*, 73(19):195416–11, 2006. doi:10.1103/PhysRevB.73.195416.

[140] W. T. Tang, E. Chung, Y.-H. Kim, P. T. C. So, and C. J. R. Sheppard. Investigation of the point spread function of surface plasmon-coupled emission microscopy. *Opt. Express*, 15(8):4634–4646, 2007.

[141] K. H. Drexhage. Influence of a dielectric interface on fluorescence decay time. *J. Lumin.*, 1,2:693–701, 1970. doi:10.1016/0022-2313(70)90082-7.

[142] M. Kreiter, M. Prummer, B. Hecht, and U. P. Wild. Orientation dependence of fluorescence lifetimes near an interface. *J. Chem. Phys.*, 117(20):9430–9433, 2002. doi:10.1063/1.1515732.

[143] M. Böhmler, N. Hartmann, C. Georgi, F. Hennrich, A. A. Green, M. C. Hersam, and A. Hartschuh. Enhancing and redirecting carbon nanotube photoluminescence by an optical antenna. *Opt. Express*, 18(16):16443–16451, 2010. doi:10.1364/OE.18.016443.

[144] T. Züchner, A. Virgilio Failla, and A. J. Meixner. Light microscopy with doughnut modes: A concept to detect, characterize, and manipulate individual nanoobjects. *Angew. Chem. Int. Ed.*, 50(23):5274–5293, 2011. doi:10.1002/anie.201005845.

[145] J. Steidtner and B. Pettinger. Tip-enhanced raman spectroscopy and microscopy on single dye molecules with 15 nm resolution. *Phys. Rev. Lett.*, 100(23):236101–4, 2008. doi:10.1103/PhysRevLett.100.236101.

[146] E. Bailo and V. Deckert. Tip-enhanced raman spectroscopy of single RNA strands: Towards a novel direct-sequencing method. *Angew. Chem. Int. Ed.*, 47(9):1658–1661, 2008. doi:10.1002/anie.200704054.

[147] Ch. Höppener and L. Novotny. Antenna-based optical imaging of single Ca2+ transmembrane proteins in liquids. *Nano Lett.*, 8(2):642–646, 2008. doi:10.1021/nl073057t.

[148] J. Stadler, T. Schmid, and R. Zenobi. Nanoscale chemical imaging of single-layer graphene. *ACS Nano*, 5(10):8442–8448, 2011. doi:10.1021/nn2035523.

[149] Ch. Höppener, R. Beams, and L. Novotny. Background suppression in near-field optical imaging. *Nano Lett.*, 9(2):903–908, 2009. doi:10.1021/nl803903f.

[150] C. C. Neacsu, S. Berweger, R. L. Olmon, L. V. Saraf, C. Ropers, and M.. B. Raschke. Near-field localization in plasmonic superfocusing: A nanoemitter on a tip. *Nano Lett.*, 10:592–596, 2010. doi:10.1021/nl903574a.

[151] C. Ropers, C. C. Neacsu, T. Elsaesser, M. Albrecht, M. B. Raschke, and C. Lienau. Grating-coupling of surface plasmons onto metallic tips: A nanoconfined light source. *Nano Lett.*, 7(9):2784–2788, 2007. doi:10.1021/nl071340m.

[152] F. Baida and A. Belkhir. Superfocusing and light confinement by surface plasmon excitation through radially polarized beam. *Plasmonics*, 4(1):51–59, 2009.

[153] J.-C. Weeber, A. Bouhelier, G. Colas des Francs, L. Markey, and A. Dereux. Submicrometer in-plane integrated surface plasmon cavities. *Nano Lett.*, 7(5):1352–1359, 2007. doi:10.1021/nl070403y.

[154] M. Rommel, J. D. Jambreck, C. Ebm, E. Platzgummer, A.J. Bauer, and L. Frey. Influence of FIB patterning strategies on the shape of 3D structures: Comparison of experiments with simulations. *Microelectron. Eng.*, 87(5-8):1566–1568, 2010.

[155] J. D. Joannopoulos, S. G. Johnson, Winn. J. N., and J. N. Meade. *Photon crystals: molding the flow of light*. Princeton University Press, 2008.

Abbreviations

1D	...	one-dimensional
2D	...	two-dimensional
3D	...	three-dimensional
AlN	...	aluminium nitride
AFM	...	atomic force microscopy
APD	...	avalanche photo diode
BFP	...	back focal plane
BL	...	Bertrand lens
CB	...	conduction band
CCD	...	charge coupled device
CdO	...	cadmium oxide
CdSe	...	cadmium selenide
CoMoCat	...	cobalt-molybdenum catalyst
CVD	...	chemical vapor deposition
DOS	...	density of states
FF	...	far-field
FIB	...	focused ion beam
FPALM	...	photoactivated localization microscopy
FWHM	...	full-width-at-half-maximum
HeNe	...	helium neon
HI	...	hyperspectral imaging
HiPCO	...	high pressure carbon monoxide
HRTEM	...	high-resolution transmission electron microscopy
LO	...	longitudinal optical
MBE	...	molecular beam epitaxy
NA	...	numerical aperture
NC	...	nanocrystal
NF	...	near-field

NW	...	nanowire
PALM	...	photo-activated localization microscopy
PL	...	photoluminescence
PSF	...	point-spread-function
QD	...	quantum dot
QY	...	quantum yield
RBM	...	radial breathing mode
SC	...	sodium cholate
SDS	...	sodium dodecyl sulfate
SEM	...	scanning electron microscopy
SERS	...	surface-enhanced Raman spectroscopy
SFLS	...	supercritical fluid liquid solid
SLS	...	solution liquid solid
SNOM	...	scanning near-field optical microscopy
a-SNOM	...	aperture-less SNOM
s-SNOM	...	scattering type SNOM
STED	...	stimulated emission depletion
STM	...	scanning tunnelling microscopy
STORM	...	stochastic optical reconstruction microscopy
SWCNT	...	single-walled carbon nanotube
TEM	...	transmission electron microscopy
TENOM	...	tip-enhanced near-field optical microscopy
TERS	...	tip-enhanced Raman spectroscopy
TOP	...	tri-*n*-octylphosphine
TOPO	...	tri-*n*-octylphosphine oxide
VB	...	valence band
VLS	...	vapor liquid solid
WZ	...	wurtzite
ZB	...	zinc-blende

List of Figures

List of Publications

During the course of my PhD research, the following peer-reviewed papers have been published:

A. Hartschuh, H. Qian, C. Georgi, M. Böhmler, L. Novotny, "Tip-enhanced near-field optical microscopy of carbon nanotubes", *Analytical and Bioanalytical Chemistry* **394**, 1787–1795 (2009).

C. Georgi, M. Böhmler, H. Qian, L. Novotny, A. Hartschuh, "Probing exciton propagation and quenching in carbon nanotubes with near-field optical microscopy", *physica status solidi (b)* **246**, 2683–2688 (2009).

T. Gokus, R. R. Nair, A. Bonetti, M. Böhmler, A. Lombardo, K. S. Novoselov, A. K. Geim, A. C. Ferrari, A. Hartschuh, "Making Graphene Luminescent by Oxygen Plasma Treatment", *ACS Nano* **3**, 3963–3968 (2009).

M. Böhmler, N. Hartmann, C. Georgi, F. Hennrich, M. C. Hersam, A. Hartschuh, "Enhancing and Redirecting Carbon Nanotube Photoluminescence by an Optical Antenna", *Optics Express* **18**, 16443–16451 (2010).

J. D. Jambreck, M. Böhmler, M. Rommel, A. Hartschuh, A. J. Bauer, L. Frey, "Light confinement by structured metal tips for antenna-based scanning near-field optical microscopy", *Proc. SPIE* **8105**, 81050G–9 (2011).

M. Böhmler, A. Myalitsin, Z. Wang, A. Mews, A. Hartschuh, "Optical imaging of CdSe nanowires with high optical resolution", *Angewandte Chemie International Edition* **50**, 11536–11538 (2011).

M. Böhmler, A. Hartschuh, "Tip-Enhanced Near-Field Optical Microscopy of Quasi-1D Nanostructures", *Chem Phys Chem*, **13**, 927–929 (2012).

List of Conferences

DPG Frühjahrstagung 2009, Dresden (Germany), 22.03. - 27.03.2009
Poster: Tip-Enhanced Optical Microscopy of Single-Walled Carbon Nanotubes

Workshop: "Carbon Nanotube Optics", Kleinwalsertal (Austria), 17.07. - 19.07.2010
Poster: Tip-Enhanced Near-Field Optical Microscopy of Carbon Nanotubes and Nanowires

Workshop: "Frontiers in Nanoscale Spectroscopy and Tomography",
Inlet (USA), 24.09. - 26.09.2009
Oral presentation: Tip-enhanced Optical Microscopy on Carbon Nanotubes and GaAs Nanowires

DPG Frühjahrstagung 2010, Regensburg (Germany), 21.03. - 26.03.2010
Oral presentation: Quantifying Excitation and Radiation Rate Enhancement Provided by Near-field Optical Antennas

EMRS 2010 Spring Meeting, Strasbourg (France), 07.06. - 11.06.2010
Poster: Tip-enhanced near-field optical microscopy on semiconductor nanowires

CeNS Workhop: Nanosciences: Merging Disciplines, San Servolo (Italy), 20.09. - 24.09.2010
Poster: TENOM - Optical Investigations with Enhanced Detection Sensitivity and Nanoscale Resolution

3rd German-Japanese Seminar on Nanophotonics, Ilmenau (Germany), 27.09. - 29.09.2010
Poster: TENOM - Optical Investigations of 1D nanostructures

DPG Frühjahrstagung 2011, Dresden (Germany), 13.03. - 18.03.2011
Oral presentation: Nanoscale Optical Imaging of Semiconductor Nanowires

NIM/CeNS Winter School, St. Christoph (Austria), 27.03 - 02.04.2011
Poster: Nanoscale Optical Imaging of Semiconductor Nanowires

TERS II, London (England), 05.07. - 06.07.2011
Poster: Nanoscale Optical Imaging of CdSe Nanowires

Workshop on Nano Carbon Optics, Herrsching (Germany), 06.10. - 09.10.2011
Poster: Nanoscale Optical Imaging of CdSe Nanowires

Danke

Als erstes möchte ich mich bei meinem Doktorvater Prof. A. Hartschuh bedanken, der mir die Möglichkeit gab diese Dissertation in seinem Arbeitskreis in München zu erarbeiten. Ich danke ihm für die wissenschaftliche Anleitung, die ständige Diskussionsbereitschaft und die Hilfestellungen bei allen Problemen. Ganz besonders bedanke ich mich für die Unterstützung und die Hilfe, die ich in persönlich schweren Zeiten erhalten habe.

Ich danke auch meinem Zweitgutachter Prof. A. Mews aus Hamburg für die gute Zusammenarbeit an den Cadmiumselenid Nanodrähten, für die Bereitstellung des Probenmaterials und für die Begutachtung meiner Dissertation.

Als nächstes möchte ich mich bei allen aktuellen und ehemaligen Mitgliedern des AK Hartschuh bedanken, bei Nicolai, Giovanni, Matthias, Nina, Harald, Julia, Sabrina, Dawid, Tobia, Richard, Tobias, Huihong, Hayk, Paulo, Alxandre und Carsten, für die gegenseitige Unterstützung, die tolle Zusammenarbeit und die freundschaftliche Atmosphäre in der Arbeitsgruppe. Danke auch an all die anderen Institutsmitglieder, die mir bei verschiedensten Fragen und Aufgaben geholfen haben.

Bei den Hamburgern Anton und Zhe bedanke ich mich für die tolle Unterstützung mit CdSe Nanodrähten und die hilfreichen Diskussionen.

Allen Freunden danke ich für viele tolle Momente, die mein Leben in dieser Zeit bereichert haben. Danke für gemeinsames Lachen und Weinen. Ein spezieller Dank geht an Matthias, durch den ich eine ganz besondere Erfahrung machen durfte: die Dust-and-Diesel Rallye nach Afrika, ein Highlight, das ich nie vergessen werde.

Meiner Familie danke ich für die Unterstützung und den besonderen Zusammenhalt, der mir sehr viel bedeutet, und der in der Zeit während meiner Doktorarbeit besonders wichtig für mich war.

Zuletzt möchte ich mich bei Carsten für die große Hilfe in allen wissenschaftlichen Belangen bedanken. Vor allem aber danke ich Dir so sehr für alles andere.